

UNIVERSITÀ DEGLI STUDI DI NAPOLI “FEDERICO II”



Scuola Politecnica e delle Scienze di Base
Department of Industrial Engineering – Aerospace Division
Doctoral Programme in Industrial Engineering
XXXI Cycle

Aeroelastic stability assessment of a CS-25 category aircraft
equipped with multi-modal wing morphing devices

Supervisors

Prof. Eng. Francesco Marulo
Prof. Eng. Leonardo Lecce
Prof. Eng. Rosario Pecora
Prof. Eng. Francesco Amoroso

PhD Candidate

Maria Chiara Noviello

Co-supervisors

PhD Antonio Concilio
PhD Ignazio Dimino

Dediche

A mio marito Domenico e alla mia preziosa famiglia, per essere la certezza più forte ed incrollabile che possa esistere. Nulla di tutto questo sarebbe stato possibile senza la vostra costante presenza, dolce rifugio per me.

Alle mie speciali Amisisters, perché la distanza “spaziale” non ci ha mai impedito di essere quotidianamente vicine. Grazie per i nostri “Ci amo”, per le parole di conforto e di confronto e per i “A domani, bimbe”, come promessa che ci saremo sempre l’una per l’altra. This is the Amisisters’ power!

Agli amici preziosi e ai miei parenti. Vi voglio bene!

Acknowledgments

First and foremost, I would like to thank the PhD School of the University of Naples “Federico II” for giving me the opportunity to work on this interesting research.

I wish to express my gratitude to *Professor Leonardo Lecce* for being an example of “war machine” to follow.

Many thanks to my *Professor Rosario Pecora* for passing on strong passion and enthusiasm for work to his students and... enthusiasm is contagious! I am extremely grateful for the technical assistance, patient supervision and excellent guidance provided throughout my PhD.

I wish to thank my *Professor Francesco Amoroso* for being by my side during these years. Constructive criticism during the discussion sections brought me to grow and mature. Besides, I am very grateful for the empathy, humility and listening, rare gifts.

...This is why they are “Two Number One Professors”!

...And, last but not least, I want to thank the Italian Aerospace Research Center for giving me this opportunity of professional growth, and for contributing to the stimulating and exciting atmosphere in which I was able to conclude my studies. I had the privilege of receiving authoritative scientific opinions of *PhD Antonio Concilio* and to work under the invaluable supervision of *PhD Ignazio Dimino*, whose teachings were fundamental to reach this goal.

Abstract

Morphing wing structures have the greatest ambition to dramatically improve aircraft aerodynamic performance (less fuel consumption) and reduce aerodynamic noise. Several studies in the literature have shown their potential for increased aerodynamic efficiency across nearly all flight conditions, enhanced aircraft maneuverability and control effectiveness, decreased takeoff/landing length, reduced airframe noise, etc. However, despite a long heritage of research, morphing wing technology has yet to be approved by the European Aviation Safety Authority (EASA) for use in commercial aviation. Models and approaches capable to predict the aeroelastic impact of a morphing wing still need to be matured to safely alter design and operation of future generations of aircraft. Additionally, a number of practical challenges remain to be addressed in the suitable materials, systems reliability, safety and maintenance.

Due to the reduced stiffness, increased mass and increased Degree Of Freedom (DOF) with respect to conventional wings, these mechanical systems can cause significant reduction of aircraft flutter margins. This aspect requires dedicated aeroelastic assessments since the early stages of the design process of such an innovative wing. Flutter boundaries predictions need sensitivity analyses to evaluate bending/torsional stiffness and inertial distribution variability ranges of the aircraft wing equipped with the morphing wing devices. In such a way, aeroelastic assessments become fundamental to drive a balance between weight and stiffness of the investigated adaptive systems. Furthermore, in pseudo rigid-body mechanisms-based morphing structures, the inner kinematics is so important that its faults may compromise the general aircraft-level functions. Similarly to the demonstration means of safety compliance, commonly applied to aircraft control surfaces, the novel functions resulting from the integration of adaptive devices into flying aircraft thus impose a detailed examination of the associated risks.

In the framework of Clean Sky 2 Airgreen 2 project, the author provides advanced aeroelastic assessments of two adaptive devices enabling the camber morphing of winglets and flaps, conceived for regional aircraft integration (EASA CS-25 category). Segmented ribs architectures ensure the transition from the baseline (or un-morphed) shape to the morphed ones, driven by embedded electromechanical actuators. Some of the advantages resulting from the combination of the two aforementioned morphing systems are wing load control, lift-over-drag ratio increase and root bending moment alleviation.

The aircraft aeroelastic model was generated by means of the proprietary code SANDY 3.0 (see APPENDIX A – General Description of the Sandy code). Then, the same code was adopted to solve the aeroelastic stability equations through theoretical modes association in frequency domain. To carry out multi-parametric flutter analyses (P-K continuation method), the actuation lines stiffness and winglet/flap tabs inertial parameters were considered in combination each other. Nominal operative conditions as well as systems malfunctioning or failures were examined as analyses cases of the investigated morphing devices, together with actuators free-play conditions. Proper design solutions were suggested to guarantee flutter clearance in accordance with aircraft stability robustness with respect to morphing systems integration, evaluated through a combination of “worst cases” simulating the mutual interaction among the adaptive systems.

The safety-driven design of the morphing wing devices required also a thorough examination of the potential hazards resulting from operational faults involving either the actuation chain, such as jamming, or the external interfaces, such as loss of power supplies and control lanes, and both. The main goal was to verify whether the morphing flap and winglet systems could comply with the standard civil flight safety regulations and airworthiness requirements (EASA CS25). More in detail, a comprehensive study of systems functions was firstly qualitatively performed at both subsystem and aircraft levels to identify potential design faults, maintenance and crew faults, as well as external environment risks. The severity of the hazard effects was thus determined and then ranked in specific classes, indicative of the maximum tolerable probability of occurrence for a specific event, resulting in safety design objectives. Fault trees were finally produced to assess the compliance of the system architectures to the quantitative safety requirements resulting from the FHAs.

Index

1	Introduction	15
1.1	General	15
1.2	Motivation of work.....	18
1.3	Objectives.....	20
1.4	Organization of the thesis.....	21
1.5	Author’s published works	22
2	State of the art on morphing structures.....	25
2.1	Adaptive wings.....	25
2.2	Clean Sky 2 Airgreen 2 Project.....	29
2.3	Overview on AG2 morphing devices.....	30
3	Morphing wing devices	33
3.1	Morphing flap.....	33
3.1.1	Scope and reference geometries.....	33
3.1.2	Aerodynamics and Benefits	34
3.1.3	Morphing flap architecture	36
3.2	Morphing winglet.....	40
3.2.1	Scope and reference geometries.....	40
3.2.2	Aerodynamics and Benefits	41
3.2.3	Morphing winglet architecture.....	42
4	Aeroelasticity	45
4.1	Introduction	45
4.1.1	Structural Model	45
4.1.2	Inertial Model.....	46
4.1.3	Aerodynamic Model	46
4.2	Aeroelastic stability equations	46
4.2.1	Generalized Aerodynamic Forces.....	46
4.2.2	Impedance matrix.....	48
4.3	Classification of the methods for flutter evaluation	50
4.3.1	K methods	51

4.3.2	PK methods	54
4.4	Aerodynamic forces approximation	58
4.4.1	P method	59
4.5	Harmonic Balance Method.....	61
5	Aeroelasticity of morphing devices	65
5.1	Dynamic Model.....	65
5.1.1	Structural Model	65
5.1.2	Inertial Model.....	73
5.2	Aerodynamic and Interpolation Model	74
5.3	Flutter Analyses.....	75
5.3.1	Trade-off flutter analysis on flap tabs	76
5.3.2	Trade-off flutter analysis on winglet tabs combined with flap tabs 86	
5.3.3	Free-Play Analyses Results, Harmonic Balance Method	103
6	Morphing Wing – Safety and Reliability issues	106
6.1	Introduction	106
6.2	Safety Analysis: general approach	107
6.2.1	Functional Hazard Assessment - FHA.....	111
6.2.2	System Safety Assessment—Fault Tree Analysis	113
6.2.3	Active Versus Hidden Failures	114
6.2.4	On safety factor.....	115
6.3	Morphing devices: Aircraft level functions	115
6.4	Morphing flap.....	117
6.5	Morphing winglet.....	122
6.6	Integrated Safety Analyses	128
7	Conclusions and Future Works.....	136
	APPENDIX A – General Description of the Sandy code.....	138
	APPENDIX B - CS 23.629 Flutter	140
	References.....	146

Nomenclature

<i>1D</i>	Mono-Dimensional
<i>2D</i>	Bi-Dimensional
<i>2MMF</i>	Bi-Modal Morphing Flap
<i>3D</i>	Three-Dimensional
<i>3MMF</i>	Three-Modal Morphing Flap
<i>A/C</i>	Aircraft
<i>AIC</i>	Aerodynamic Influence Coefficients
<i>b</i>	Span Length
<i>B_i</i>	i-th Block Of The Rib
<i>C_L</i>	Lift Coefficient
<i>C_{L_MAX}</i>	Maximum Lift Coefficient
<i>C_P</i>	Pressure Coefficient
<i>C_r</i>	Root Chord Length
<i>C_t</i>	Tip Chord Length
<i>D</i>	Drag
<i>DLM</i>	Doublet Lattice Method
<i>DMIG</i>	Direct Matrix Input At Grids
<i>DOF</i>	Degree Of Freedom
<i>EA</i>	Normal Force Stiffness
<i>ECU</i>	Electronic Control Unit
<i>EI_{min(max)}</i>	Minimum (Maximum) Bending Stiffness
<i>FDAL</i>	Functional Design Assurance Level
<i>FE(M)</i>	Finite Element (Model)
<i>FHA</i>	Fault And Hazard Assessment
<i>FT(A)</i>	Fault Tree (Analysis)
<i>GAF</i>	Generalized Aerodynamic Forces
<i>G_{ij}</i>	Participation Factor Mode I With Respect To Mode J
<i>GJ</i>	Torsional Stiffness
<i>GRA</i>	Green Regional Aircraft
<i>GVT</i>	Ground Vibration Test
<i>HD</i>	Harmonic Drive
<i>K</i>	Actuators Stiffness
<i>K_{eq}</i>	Actuators Equivalent Stiffness
<i>L/D</i>	Aerodynamic Efficiency
<i>L</i>	Lift
<i>LVDT</i>	Linear Variable Displacement Transducer
<i>MAC</i>	Mean Aerodynamic Chord
<i>MAV</i>	Micro Air Vehicle
<i>MT</i>	Maintenance Time
<i>MWL</i>	Morphing Winglet
<i>MZFW</i>	Maximum Zero Fuel Weight
<i>NS</i>	Navier-Stokes
<i>PSSA</i>	Preliminary System Safety Assessment
<i>RBE</i>	Rigid Body Element
<i>SSA</i>	System Safety Assessment
<i>TP90</i>	90-Pax Turboprop

<i>TRL</i>	Technology Readiness Level
<i>UAV</i>	Unmanned Aircraft Vehicle
<i>V_D</i>	Dive Speed
<i>V_F</i>	Flutter Speed

List of Figures

Fig. 1: Example of flutter shapes in case of movable surfaces	17
Fig. 2: Wright-Brothers aircraft: a detail of wing warping, [19]	25
Fig. 3: Morphing wing concept: (a) NASA Dryden inflatable wing during flight testing [24]; and (b) telescopic wing concept [25].....	27
Fig. 4: (a) Lockheed Martin folding-wing UAV concept, [26], and (b) NextGen Batwing morphing UAV concept, [27].....	27
Fig. 5: MAV roll control achieved via wing warping, [28]	28
Fig. 6: Drooped Nose structure, [30]	31
Fig. 7: Morphing flap architecture, top view	32
Fig. 8: Morphing winglet Finite Element Model (left) and architecture (right), [31]	32
Fig. 9: Morphing flap investigation domain, [32].....	34
Fig. 10: Aerodynamic pressure uniform distribution on tabs surfaces, [32]	35
Fig. 11: Morphing flap articulated rib, [32]	36
Fig. 12: Morphing flap target shape, mode 1, [32]	36
Fig. 13: B1/B2 gear ratio trend, [32].....	37
Fig. 14: Morphing flap preliminary design assumption, [32]	38
Fig. 15: Section view of through shaft actuation concept, [32]	39
Fig. 16: Wireframe view of through shaft actuation concept, [32].....	39
Fig. 17: Movable surfaces of the morphing winglet, [38]	40
Fig. 18: Upper (on left) and lower (right) deflection, [38]	41
Fig. 19: Example of C_p distribution on the morphing winglet for negative deflections of both the upper and lower surfaces, [38]	41
Fig. 20: Detail of the morphing winglet architecture, [38].	42
Fig. 21: Detail of the morphing winglet architecture, [38].	43
Fig. 21: EMA actuators: a) sectional and b) external view, [37]	43
Fig. 22: Aeroelasticity conceptual scheme, [40].....	45
Fig. 23: Aerodynamic Lattice, [40].....	47
Fig. 24: Example of V-g plot in case of two modes only, K-Method, [40]	52
Fig. 25: Non –linearity in a linear system, [40]	61
Fig. 26: LH morphing flap preliminary Finite Element Model developed by UniNa, [31]	66
Fig. 27: LH morphing winglet preliminary Finite Element Model developed by CIRA, [31]	66
Fig. 28: Elastic axis convergence parameter, [31]	68
Fig. 29: Logical Flow for the stiffness properties evaluation	69
Fig. 30: Example of load case applied for GJ evaluation, [31].....	70
Fig. 31: Flap tabs stiffness properties	71
Fig. 32: Winglet tabs stiffness properties	72
Fig. 33: TP90 Dynamic model in Sandy environment (ref. axes in meters), [31]	74

Fig. 34: TP90 aerodynamic model in Sandy environment (ref. axes in meters), [31]	74
Fig. 35: TP90 Aeroelastic model in Sandy Environment (ref. axes in meters), [31]	75
Fig. 36: Trade- off analyses parameters on flap tabs	77
Fig. 37: First trade-off Carpet Plot.....	77
Fig. 38: Flutter mode 31 - Symmetric wing tip/winglet bending	78
Fig. 39: Flutter Mode 37 - Symmetric outer wing torsion.....	79
Fig. 40: Flutter Mode 38 - Anti-symmetric outer wing torsion	79
Fig. 41: Participation Factors, Mode 31 [31]	80
Fig. 42: Participation factors, Mode 37, [31].....	81
Fig. 43: Participation factors, Mode 38, [31].....	81
Fig. 44: Minimum modal flutter association.....	82
Fig. 45: Minimum flutter speed as function of flap tabs degree of balancing, for a fixed value of tabs actuation line stiffness	84
Fig. 46: Minimum flutter speed as function of flap tabs actuation line stiffness, 30 % Degree of Balancing	85
Fig. 47: Flutter speed as function of tabs actuation line stiffness, 40% Degree of Balancing	85
Fig. 48: Trade-off analysis on winglet tabs combined with flap tabs in locked commands, carpet plot [31].....	87
Fig. 49: Mode 31: anti-symmetric wing tip torsion/winglet bending	88
Fig. 50: Mode 32: Symmetric outer wing torsion/winglet bending.....	88
Fig. 51: Anti-symmetric outer wing torsion/winglet bending	89
Fig. 52: Example of V-g plot on winglets tabs trade-off analysis, [31].....	90
Fig. 53: Mode 31, Participation factors	91
Fig. 54: Mode 32, Participation factors	91
Fig. 55: M33, Participation factors	91
Fig. 56: Minimum modal association, winglets tabs flutter modes	92
Fig. 57: Minimum flutter speed VS winglet tabs degree of balancing in two inertial configurations (nominal and 30% increase of the nominal mass).....	93
Fig. 58: Minimum flutter speed as function of tabs degree of balancing.	94
Fig. 59: Flutter speed trend as a function of plug stiffness gain factor.....	95
Fig. 60: Flutter speed trend as a function of tabs massbalancing, F DMIK = 5	96
Fig. 61: Winglets tabs mass gain factor as function of flutter speed, with plug stiffness gain factor equal to 5	97
Fig. 62: Winglets tabs mass gain factor as function of flutter speed, with plug stiffness gain factor equal to 2	97
Fig. 63: Winglet bending mode (M32), in case of no plug stiffness gain factor and 100% tabs mass	99
Fig. 64: V-g plot in the condition A.....	100
Fig. 65: – Simmetric wing torsional-bending mode in case of F DMIK=2 and wlet tabs mass 70%	101
Fig. 66: V-g plot in the condition B.....	102

Fig. 67: Load-Deflection non-linear law	103
Fig. 68: Winglet tabs actuators equivalent stiffness Vs tabs oscillation amplitude.....	104
Fig. 69: Flutter analyses results in case of tabs actuators free-play	105
Fig. 70: Example of electromechanical Actuator fault tree with failure rates per hour	107
Fig. 71: CS-25 safety assessment process overview.....	109
Fig. 72: Relationship between Probability and Severity of Failure Condition Effects, [2].....	110
Fig. 73: Required probability figures versus safety classification.....	113
Fig. 74: Safety factor vs probability in failure condition.....	115
Fig. 75: Morphing Flap High Lift Generation Fault Tree Analysis.....	121
Fig. 76: Morphing flap Undetected Inadvertent tab control at high speed Fault Tree Analysis	121
Fig. 77: Morphing winglet - Uncontrolled dynamic motion (left or right) Fault Tree Analysis	127
Fig. 78: Destruction of wing FTA.....	127
Fig. 79: LH winglet tabs actuators and gear ratio DMIG scheme, Baseline configuration	128
Fig. 80: CASE 1 – LH upper link isolated failure	129
Fig. 81: CASE 2 – LH lower link isolated failure	130
Fig. 82: CASE 3: LH upper tab actuator isolated failure.....	130
Fig. 83: CASE 4 - LH lower tab actuator isolated failure	131
Fig. 84: CASE 5 – LH upper actuator and link combined failure	132
Fig. 85: CASE 6 – LH lower actuator and link combined failure	132
Fig. 86: CASE 7 – LH upper actuator and lower link combined failure	133
Fig. 87: CASE 8 – LH lower tab and upper link combined failure	134
Fig. 88: Example of V-g plot	144

List of Tables

Table 1: Aerodynamic values in limit load condition, [32]	35
Table 2: Winglet materials mechanical properties.....	44
Table 3: Massbalancing values of morphing flap tabs.....	83
Table 4: Massbalancing solutions: impact on winglet weight	86
Table 5: Winglet weight in case of 130% DoB	94
Table 6: Winglet weight in case of doublet stiffness of plug and 30% saving of tabs mass	98
Table 7: Flutter Results of Condition A.....	98
Table 8: Flutter Results of Condition B	100
Table 9: Equivalent stiffness of winglet tabs actuation line	104
Table 10: Aircraft functions impacted by Morphing Wing concept, [43]-[44]	116
Table 11: Aircraft functions impacted by Morphing Flap concept, [45].....	119
Table 12: Potential failures identified in morphing winglet preliminary FHA	123
Table 13: Aircraft functions impacted by Morphing Winglet concept.....	125
Table 14: Failure scenarios investigated for morphing winglet.....	129
Table 15: Flutter analyses results in failure scenarios investigated for morphing winglet.....	134

1 Introduction

1.1 General

Over the last few years, aerospace research efforts are increasingly focusing on advanced solutions capable to improve aerodynamic efficiency for reducing fuel consumption and pollutant emissions of the next generation air transport. One of the ways to accomplish such benefits relies on morphing wing devices, capable of adapting their shape in a continuous manner during aircraft flight. From the structural perspective, this requires developing fully integrated structures with actuation and compliance control capable to fulfill conflicting requirements: the structure must be stiff to withstand the external loads, but must be flexible to enable shape changes.

There is no doubt that the achievement of adaptive structures entails more complex and heavier architectures, if compared to conventional ones, to withstand operative loads with adequate margins of safety. This aspect is predictable and manageable since the price to be paid for a technology implementation at aircraft level is proportioned to the benefits brought by it. Moreover, assuming the civil transportation as a target, also the smallest improvement becomes significant when multiplied by the massive amount of aircraft composing the fleet. It was demonstrated that by means of the adaptive wing trailing edge camber morphing, the aerodynamic efficiency increases by 2%; as a consequence, fuel burnt saving was estimated equal to the 3% per flight, [1]. These numbers give us the immediate perception of the environmental benefits; beyond that, such a decrease in fuel burnt allows for a strong operative cost saving (about 10 million dollars/year for a mid-size fleet of large commercial airplanes). Therefore, for larger fleets there are bigger advantages. Nevertheless, although morphing devices generally have favorable performance for small or unmanned aircraft applications, the most ambitious challenge is to explore true-scale solutions for manned flights, compliant with EASA (/FAA) airworthiness requirements part 25 ([2]) and with series production and implementation on modern civil aircraft. The associated technological development required for such aircraft segment is very high. However, it is also true that the payoff may be, in perspective, very high.

When dealing with the design of morphing wing devices, multidisciplinary aspects need to be thoroughly considered due to the systems complexity involving aerodynamics, structures, actuation architectures, control logics and aeroelasticity, [3].

Speaking about the latter, it regards the effect of aerodynamic forces on elastic bodies, such as aircraft wings or compressor blades, which fully depend on the deformed shape of the structure in the flow. One of the most serious aeroelastic phenomena is the instability of a structure in a flow. For a given initial shape of an elastic structure, the aerodynamic force increases rapidly with the flow speed, and there may exist a critical flow speed at which the structure becomes unstable. Such instability may cause excessive deformation, and may lead to the destruction of the structure. The interplay of aerodynamic, elastic, and inertia forces is usually referred to as flutter or dynamic aeroelastic instability. If a structure is excited with external forces in the absence of flow, the structure will oscillate and the oscillation will damp gradually. With the presence of a flow, the rate of damping of the oscillation may increase at low flow speeds and on increasing the flow speed, a point will be reached at which the damping rapidly decreases, and the oscillation can just maintain itself with a steady amplitude. This speed is known as the critical flutter speed, and at speed of flow just above that critical speed, a great violent oscillation will be triggered, at any small disturbance to the structure, and the structure is said to flutter.

There are many definitions of flutter within the literature. Some of the most recognized are [4] – [5]:

- Aeroelastic and self-excited vibration, in which the external source of energy is the air stream;
- Aerodynamic self-excited oscillations;
- Self-sustained oscillatory instability;
- Cyclic and high frequency oscillation of the airfoil caused by a struggle between the aerodynamic forces and the stiffness of the surfaces;
- Dynamic instability of an elastic body in an airstream produced by aerodynamic forces which result from the deflection of the elastic body from its undeformed state;
- Dynamic aeroelastic instability;
- Dynamic instability occurring in an aircraft in flight at a certain speed where the elasticity of the structure plays an essential part in the instability;
- Self-excited or unstable oscillation arising out of the simultaneous action of elastic, inertia and aerodynamic lift forces upon a mass or a system of masses;

- Oscillatory instability arising from the condition where one degree of freedom is driven at resonance by a second degree of freedom, both oscillating at the same frequency;
- Unstable divergent motion or vibration caused by the aerodynamic forces;
- A condition at which the total damping of a system under the action of air forces (and the inertia, elastic, and friction forces) changes from positive to negative, at flutter speed the damping is zero so that sustained oscillations would occur.

The parametric study of flutter is a crucial step of the aeroelastic assessment. Aeroelastic stability equations can be solved numerically by adopting different methods, detailed in Section 4. Typically, the outputs of flutter analyses are condensed in the so-called V-g plot, showing the trend of flutter modes speed as a function of the modal damping (further details are provided in APPENDIX B - CS 23.629 Flutter).

When dealing with conventional A/C movable surfaces (flaps, ailerons, rudder...), both bell-shaped and sharp flutter instabilities may occur, as shown in Fig. 1. Due to the unconventional arrangement of morphing systems and their **mutual interaction in a morphing wing**, especially in systems malfunctioning or failure conditions, such aeroelastic assessments are strongly recommended since the preliminary stage of the wing design process. In what follows, the aeroelastic behavior of a regional aircraft wing equipped with morphing flaps and adaptive winglets is investigated to estimate design feasibility and effectiveness from a structural standpoint.

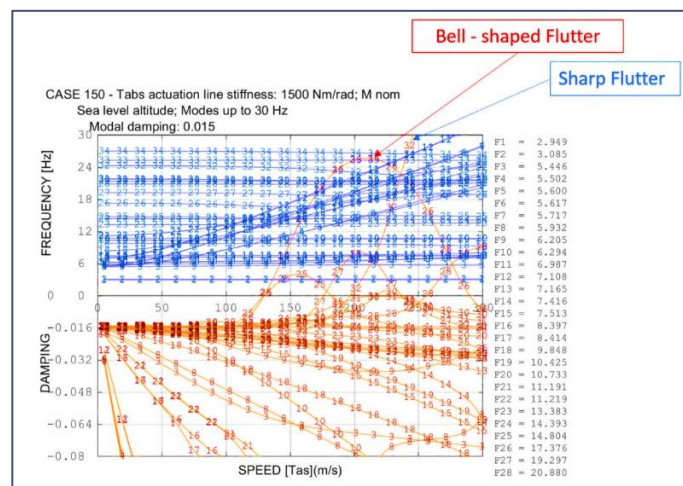


Fig. 1: Example of flutter shapes in case of movable surfaces

1.2 Motivation of work

In general, morphing structures can change their geometry in order to achieve a wide range of performance, [6]. In case of morphing aircraft, such goals include alleviating drag, or altering airfoil lift.

Conventional engineered structures, such as aircraft wings, are conceived to exhibit a desired aeroelastic response. This allows for obtaining small operational deflections, and hence well-defined aerodynamic and aeroelastic loading. Therefore, structural engineers feel certain that a wing with the required mass and stiffness, and with the shape set out by aerodynamics engineers, will allow achieving the predicted lift and drag properties. Well-developed aircraft systems sizing methods apply, speeding up the early stages of the design process, [7]. It is not possible to state the same for the design of morphing wing structures. The large changes in performance achievable have an inevitable impact in terms of the mass, stiffness and actuation requirements. This complicates the systems sizing, since it is not immediate defining which morphing configuration should dominate the design. In the literature, these difficulties are overcome by reducing the problem to its constituent components. These involve designing the aircraft structure ensuring the target morphing shapes, or performing aerodynamic optimization to find the optimum shapes that wings should morph between. A further step regards the interaction between structure and aerodynamics, to ensure aeroelastic stability during flight. The strategy of splitting the design problem into distinct disciplines has enabled production of a great amount of morphing aircraft concepts. However, it should be noted that a more comprehensive approach could emphasize the potential structural improvements in terms of weight and number of components while maintaining the requested aerodynamic benefits. A brief summary of these design methods is recalled below to highlight the difficulties of an integrated-design approach.

- *Structural optimization* solves a material distribution problem subject to constraints, [8]. For the majority of structural optimization problems, the aim is to conceive a structure which can support a given load, although achieving other characteristics as, for example, minimum total weight, optimal center of mass location, or meeting a given density requirement. Typically, the optimization problem is solved through parametrization schemes, such as sizing, material, shape and topology optimization [9] - [10] - [11] - [12].

- *Aerodynamic optimization* is the process of finding the geometry providing the best aerodynamic properties. A typical problem optimizes a set of decision variables governing the airfoil shape through a predefined parameterization scheme. The new shape's aerodynamic properties are then evaluated, and used to update the decision variables, until the geometry has converged to an optimal solution [13] - [14] - [15]. Aerodynamic optimization of morphing structures requires replacement of the shape parameterization by a structural model with optimizer-controlled actuation, [16]. The sensitivity analysis can then be performed to investigate the result of small perturbations in the actuation variables on the resulting structure, and subsequent flow properties. Computationally-efficient structural models are typically implemented, to reduce the expense of predicting structural displacements, [17]. This reduces the computational requirements of the sensitivity analysis, which are often dominated by aerodynamic calculations. A benefit of this type of analysis is that the aeroelasticity of the problem can be readily evaluated [18]; a summary of which follows below.
- *Aeroelastic tailoring* regards the effect of interaction between the aerodynamic loads due to normal operating flight and the elastic deformation of the aircraft structure [18]. It can have a huge impact on flight performance: stability, handling and structural load distribution can all be involved. When dealing with the design of morphing wing structures, due to the augmented Degree Of Freedom and weight with respect to conventional architectures, it is typically required to increase their compliance to enable shape changes. This can make them susceptible to large deformations due to aerodynamic loads, which in turn can influence aircraft stability; flutter boundaries can be reduced significantly with respect to rigid airfoils. This indicates that introducing compliance can lead to reduced stability.

All the aforementioned topics drove toward the scope of the present thesis. More in detail, to enable effective aeroelastic wing shape control, a more comprehensive design approach was developed to properly predict flutter boundaries and the related sensitivity by changing bending/torsional stiffness and mass distribution.

1.3 Objectives

Sensitivity analyses are a powerful tool to create an accurate representation of the “design space”, enabling the optimal design of a next generation aircraft wing equipped with morphing devices. *The main target of this work was to study the aeroelastic impact - at aircraft level – of an adaptive wing incorporating morphing flaps and winglets, in nominal and in failure conditions, in accordance with the CS-25 airworthiness requirements.* More in detail, the key objectives are:

- ✓ **Aeroelastic-driven design and stability investigations** of a regional aircraft wing equipped with morphing flaps and adaptive winglets. High-fidelity trade-off analyses are thus carried out to drive the design process of the morphing devices. The impacts of morphing systems kinematics, masses and distributed stiffness of the adaptive devices are evaluated in combination each other. This allows obtaining a stability range of such parameters by defining aeroelastic safety limits. On the other hand, in case of demonstrated aeroelastic unsafety, design solutions such as massbalancing of movable parts are adopted; also this stage requires trade-off analyses to evaluate the minimum degree of balancing ensuring flutter clearance. Moreover, the uncertainties in the structural dynamics due to actuators free-play are considered in this preliminary assessment, by reducing bi-linear actuation line stiffness into equivalent values by means of proper methods.
- ✓ **Aircraft stability robustness assessments** to morphing systems integration. The combination of “worst cases” simulating the mutual interaction among the adaptive systems is a key aspect while performing trade-off analyses. The “worst case” indicates that in addition to the case that the aircraft is aeroelastically safe with the nominal model, it should also be safe with a combination of morphing wing devices. This allows predicting satisfactory margins of stability and performance even in case of combined variations in the envisaged morphing systems parameters.
- ✓ **Safety and reliability issues of a morphing wing** by assessing different failure conditions to be included in the aeroelastic analyses of the morphing devices. It is worth mentioning that the total loss of a morphing device due to kinematic failures may result in free unforced

oscillations which may potential lead to flutter phenomena. Failure scenarios for the morphing wing devices were thus investigated by reproducing the rupture of primary hinges and/or actuation links of the movable parts.

Multi-parametric analyses results were thus used to identify and validate proper “aeroelastically safe” design solutions with respect to morphing surfaces. For that purpose, the proprietary code SANDY 3.0 code was adopted to solve the aeroelastic stability equations through theoretical modes association in frequency domain. Moreover, safety activities were performed to verify whether morphing flap and winglet concepts could comply with the standard civil flight safety regulations and airworthiness requirements. Fault and Hazard Analysis (FHA) was used to assess the severity of properly identified failure conditions and then allocate safety requirements. Fault Tree modelling technique was used to verify the compliance of the system architectures to the quantitative safety requirements resulting from the FHAs.

1.4 Organization of the thesis

The present thesis deals with a number of topics ranging from the generation of aeroelastic models, up to several cases of trade-off flutter analyses in nominal and failure conditions, and finally safety Fault and Hazard and Fault Tree analyses. The work is organized into seven chapters, as follows:

- Chapter 1 contains an introduction to the aircraft aeroelastic problem, due to interaction effects among elastic, inertial and aerodynamic forces. Particular focus is given to the aeroelastic impact at aircraft level of morphing wing devices and how aeroelastic assessments can drive their preliminary design.
- Chapter 2 details the state of the art of morphing wing structures, contextualized into Air Green 2 project, concerning the design of innovative devices enabling the controlled shape morphing of relevant segments of the wing. Such project investigates three adaptive architectures: wing leading edge, outer wing flap and winglet. Benefits resulting from the combined applications of the three morphing surfaces are herein set out.

- Chapter 3 illustrates morphing flap and winglet concepts, in terms of structural layouts and aerodynamic benefits. A detailed description of some key concepts is given, together with information on the enabling technology and design methods of both the morphing flap and adaptive winglet.
- Chapter 4 explains in detail the numerical approach to perform flutter analyses. All the steps needed to generate an aeroelastic model are described; aeroelastic stability equations are presented and the most common resolution methods are herein mentioned.
- Chapter 5 is the real heart of this activity. It addresses the aeroelastic stability investigation performed on the aircraft equipped with morphing flap and winglet tabs. Rational approaches were implemented in order to simulate the effects induced by variations of movable surfaces actuators stiffness on the aeroelastic behavior of the aircraft also in correspondence of several failure cases. Reliable aeroelastic models and advanced computational strategies were properly implemented to enable fast flutter analyses covering several configuration cases in terms of structural system failures.
- Chapter 6 deals with safety analyses performed to verify whether morphing flap and winglet concepts could comply with the standard civil flight safety regulations and airworthiness requirements. Rational failure scenarios were also simulated in aeroelastic analyses to be integrated into safety analyses results.
- Chapter 7 concludes the work, in terms of obtained results and future developments of the activity.

1.5 Author's published works

1. Noviello, M. C., Rea, F., Arena, M., Pecora, R., Amoroso, F., "Description of position control laws for functionality test of a bi-modal morphing flap", *International Journal of Mechanical Engineering and Robotics Research*, in printing.
2. Noviello, M. C., Dimino, I., Amoroso, F., Concilio, A., Pecora, R., "Preliminary assessment of morphing winglet and flap tabs influence

- on the aeroelastic stability of next generation regional aircraft”, Proceedings of SMASIS Conference on Smart Materials, Adaptive Structures and Intelligent Systems, September 2018.
3. Rea, F., Amoroso, F., Pecora, R., Noviello, M.C., Arena, M., “Structural Design of a Multifunctional Morphing Fowler Flap for a Twin-Prop Regional Aircraft”, Proceedings of SMASIS Conference on Smart Materials, Adaptive Structures and Intelligent Systems, September 2018.
 4. Arena, M., Noviello, M.C., Rea, F., Amoroso, F., Pecora, R., “Control strategy of an electrically actuated morphing flap for the next generation green regional aircraft“, Proceedings of SPIE - The International Society for Optical Engineering, April 2018.
 5. Pecora, R., Amoroso, F., Noviello, M.C., Dimino, I., Concilio, A., “Aeroelastic stability analysis of a large civil aircraft equipped with morphing winglets and adaptive flap tabs”, Proceedings of SPIE - The International Society for Optical Engineering, April 2018.
 6. Bellucci, M., Noviello, M.C., Amoroso, F., Pecora, R., Dimino, I., Concilio, A., Book Chapter “Stress Analysis of a Morphing System”, Morphing Wing Technologies: Large Commercial Aircraft and Civil Helicopters”, October 27th, 2017.
 7. Rea, F., Pecora, R., Amoroso, F., Arena, M., Noviello, M.C., Amendola, G., “Aeroelastic stability analysis of a wind tunnel wing model equipped with a true scale morphing aileron”, International Journal of Mechanical Engineering and Robotics Research, Vol.6, N. 6, November 2017.
 8. Noviello, M.C., Pecora, R., Amoroso, F., Rea, F., Arena, M., Dimino, I., “Experimental shape reconstruction of a morphing wing trailing edge in simulated operative conditions”, Proceeding of ICMAE – International Conference of Mechanical and Aerospace Engineering, 249-256, July 2017.
 9. Arena, M., Pecora, R., Amoroso, F., Noviello, M.C., Rea, F., Concilio, A., “Aeroelastic analysis of an adaptive trailing edge with a smart elastic skin”, Proceedings of AIP Conference, July 2017.
 10. Pecora, R., Amoroso, F., Arena, M., Noviello, M.C., Rea, F., “Experimental validation of a true-scale morphing flap for large civil aircraft applications”, Proceedings of SPIE - The International Society for Optical Engineering, April 2017.

11. Noviello, M.C., Rea, F., Arena, M., Pecora, R., Amoroso, F., “Actuation and control of a novel wing flap architecture with bi-modal camber morphing capabilities”, Proceedings of 2016 7th International Conference on Mechanical and Aerospace Engineering, ICMAE, July 2016.
12. Rea, F., Arena, M., Noviello, M.C., Pecora, R., Amoroso, F., “Preliminary failure analysis of an innovative morphing flap tailored for large civil aircraft applications”, Proceedings of 2016 7th International Conference on Mechanical and Aerospace Engineering, ICMAE, July 2016.
13. Arena, M., Noviello, M.C., Rea, F., Amoroso, F., Pecora, R., Amendola, G., “Modal stability assessment for a morphing aileron subjected to actuation system failures: Numerical analysis supported by test evidence”, Proceedings of 2016 7th International Conference on Mechanical and Aerospace Engineering, ICMAE, July 2016.

2 State of the art on morphing structures

2.1 Adaptive wings

Morphing wing structures are not a new concept. As well known, the Wright brothers exploited wing warping to accomplish roll control of some of their early aircraft.

They knew that aircraft mass reduction was critical to achieve with limited thrust, and this eliminated the potentiality of flight control by heavy and complex mechanisms. Instead, structure adaptability was utilized; cable actuation used to warp the wing, as shown in Fig. 2. The resulting rolling moment ensured flight control, corresponding with minimal weight penalty, [19].

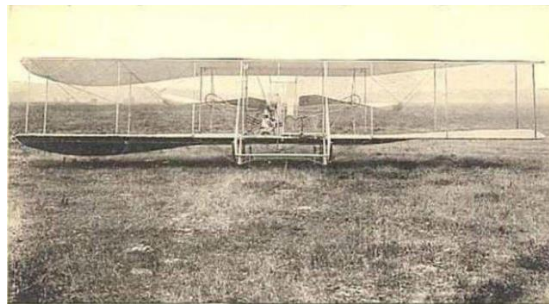


Fig. 2: Wright-Brothers aircraft: a detail of wing warping, [19]

Despite the benefits demonstrated by this “primeval” concept, morphing wing structures were strongly inadequate to make their way into commercial aircraft. For certification and reliability reasons, engineers instead are inclined towards rigid structures. Thus, current design conventions establish that aircraft should have rigid wings, with control achieved through movable surfaces such as leading and trailing edge flaps. However, advances in engineering are inducing these conventions to be redescribed.

The increasing development of smart systems technologies and improved analysis techniques made possible the fact that these structures can be designed and optimized relatively quickly, [20]. This allows engineers to face with feasibility aspects in ways not previously possible. All of these factors have led to renewed interest in the field of morphing wing devices, by providing the necessary confidence needed to invest in achieving the aerodynamic benefits they can convey. In the last twenty years, this has provoked a real explosion of literature on the subject, a full account of which is beyond the scope of this work. Instead,

a summary of key concepts is shown, combined with information on the enabling technology and design methods.

When dealing with morphing wing structures, the type of morphing is typically separated into two categories ([21]): morphs which occur in the plane of the wing itself (*planform morphing*), varying properties such as wing span, sweep and planform area; and those normal to it (*out-of-plane morphing*), where variations in camber, chord length, and airfoil profile are achieved.

Planform morphing typically results in significantly affected performance, ensuring the combination of aircraft design requirements previously in discordance each other. For example, high-altitude performance are often at the expense of low maneuverability and speed to achieve cruise and loiter characteristics. Similarly, military fighter aircraft achieve maneuverability and high speed, paying in terms of efficiency, [22]. Thus, planform morphing leads the way toward a multi-purpose vehicle, capable of operating optimally at both extremes, [23]. Some current concepts, and other novel ideas for large-scale planform morphs, are demonstrated below.

Functional inflatable wings have been used in aircraft applications since the 1950's. In 2001, an inflatable Unmanned Aircraft Vehicle, developed by NASA Dryden, was tested in flight. Such a vehicle was designed as a gun-launched surveillance vehicle, by adopting inflatable wings to assure the concept could fit inside a capsule suitable for launching. In-flight deployment of the inflatable concept, which takes approximately 0.3 s, is shown in Fig. 3, [24]. Once deployed to their 1.524 meters wingspan, the wings are capable of withstanding the aerodynamic loads due to the UAV flight. Although wings such as these are unlikely to support the large aerodynamic loads found on commercial aircraft, the concept has helped to produce new designs for more versatile UAVs. One such example is the telescopic spar concept, enabling aspect-ratio variation, shown in Fig. 3(b), [25]. Three concentric aluminum tubes, decreasing in diameter and increasing in length, compose the internal mechanism. Pressurized deployment of these tubes achieves a variety of wingspan configurations. During testing, the joints in the outer skin led to viscous drag, making the wing 25% less efficient than a single-piece wing of comparable size. The fully deployed structure exhibited a lift to drag ratio equal to 10. Although much less than some conventional wings, the additional benefit of reduced high-speed drag in the partially deployed state must also be considered.

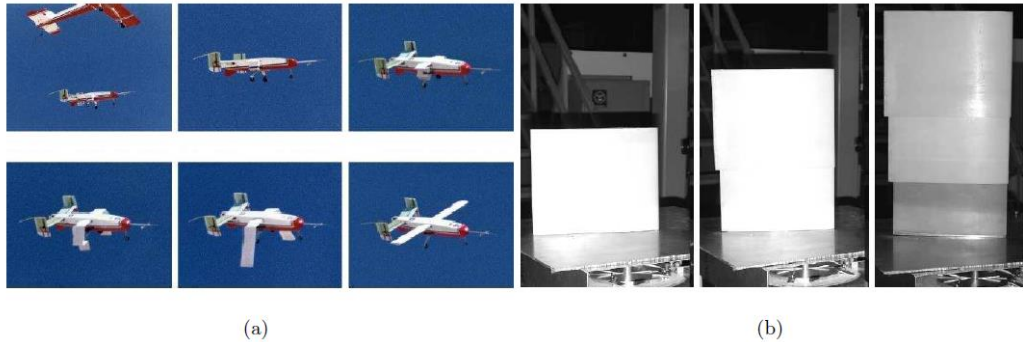


Fig. 3: Morphing wing concept: (a) NASA Dryden inflatable wing during flight testing [24]; and (b) telescopic wing concept [25]

[26] reports a Lockheed Martin investigation about the design of a planform morphing aircraft. In this concept, two chordwise hinges to fold the wing enables the morphing, as depicted in Fig. 4. Without changing planform edge alignment, an effective sweep change of 30° can be obtained, [27]: this is in association with 71% of span augment and 180% of total wing area increase. In this specific application, morphing allows for a wetted area 23% less in the folded configuration, although achieving a 52% increase in L/D in the unfolded state.

All the described characteristics would facilitate efficient high-speed low-altitude flight using the folded state to reduce drag and improve efficiency. Moreover, the transition to the unfolded configuration is conceived to improve range and endurance for high-lift and loiter situations. The folding-wing idea is, in this respect, suitable for a multi-purpose vehicle having characteristics such as efficiency, speed, agility relative to fixed wing counterparts.



Fig. 4: (a) Lockheed Martin folding-wing UAV concept, [26], and (b) NextGen Batwing morphing UAV concept, [27]

Out-of-plane morphs typically are in association with smaller deflections than in-plane variations. For this reason, they seek to aircraft control, instead of

providing multi-purpose capabilities. Conventional control surfaces and mechanism can be replaced by morphing wing architectures, enabling a smooth and continuous surface to cleave the flow, retarding the onset separation and the transition to a turbulent boundary layer. Expedients to reach the aforementioned targets are several: from camber shape changing, to wing twisting and/or banding variations.

These methods are deductible by the following concepts from the literature. [28] discusses a Morphing Micro Air Vehicle (MAV) using wing twisting for roll control. A carbon composite frame, together with a plastic-membrane wing, composes the MAV structure. Torque rods attached to electronic servos and located inside the fuselage are fixed into the membrane wing's leading edge: this enables morphing capabilities. Application of torque allows for the wing twist, through a large displacement at the trailing edge, as shown in Fig. 5. During flight tests, a sufficient roll control of the aircraft was demonstrated due to the wing warping. However, attachment of a rudder was required to give yaw control, also ensuring stability.

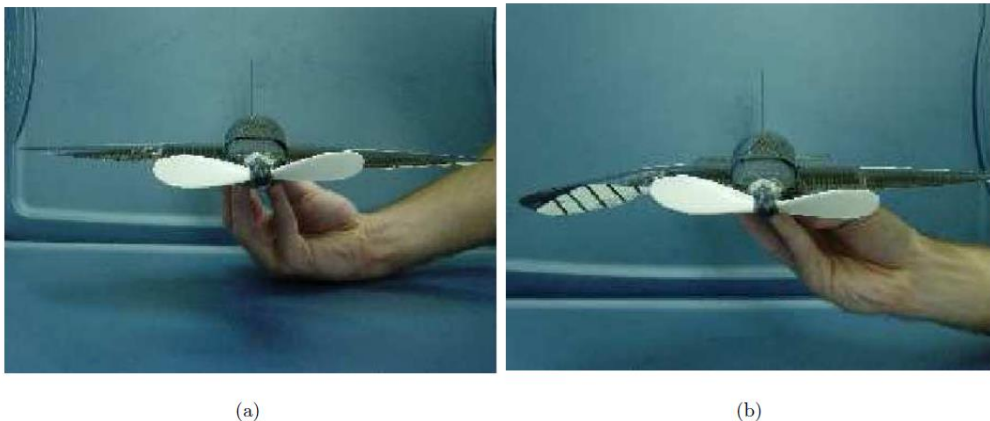


Fig. 5: MAV roll control achieved via wing warping, [28]

This variety of concepts demonstrates the feasibility of chordwise morphing, and all the improvements in control and efficiency it can bring. In addition, the possibility of an efficient multi-purpose aircraft vehicle becomes tangible, when chordwise adaptability is associated with the large-scale change achievable with planform morphing.

2.2 Clean Sky 2 Airgreen 2 Project

Clean Sky2 is one of the largest research program ever launched at European level. Funded by the EU's Horizon 2020 programme, it contributes to establish European aero-industry collaboration, global leadership and competitiveness [29]. Large efforts are currently spent through the CleanSky2 program to develop an efficient air transport system identified through a lower environmental impact combined to unequalled capabilities of ensuring safe and seamless mobility while complying with very demanding technological requirements.

Within CleanSky 2 scenario, AirGreen 2 project aims to develop and demonstrate novel concepts and methodologies for the purposes of a new generation wing realization. Such a wing will be characterized by:

- an innovative structure, resulting from improved life cycle design;
- a high level of adaptability (shape-changing), enabling load control and alleviation functions, and improving the aerodynamic performance at the different flight regimes;
- an innovative aerodynamic design, to preserve of the natural laminar flow and for the drag reduction.

The validation platform of the integrated technologies is what is currently presented -at European Level- as the next generation Green Regional Aircraft (GRA). Active from 2006, GRA panel aims to conceive, validate and demonstrate "green" aeronautical technologies best fitting the regional aircraft that will fly from 2020 onwards. For that purpose, specific and challenging domains are considered:

- Advanced low weight and high performance structures;
- All-electric systems and bleed-less engine architectures;
- Low noise/high efficiency aerodynamic;
- Environmentally optimized missions and trajectories management.

Such technologies are destined to two different aircraft concepts, identified by means of two seat classes, [29]:

1. 90-seat, with Turboprop engine (TP90);
2. 130-seat, with a combination of novel propulsion solutions, as the Geared Turbofan (GTF), the Advanced Turbofan (ATF) and the Open Rotor (OR) configuration.

TP90 will be considered as the reference platform for the integration of morphing flaps and winglets concepts in this thesis.

An overview of the AG2 morphing technologies investigated is provided in the following section, for the sake of completeness.

2.3 Overview on AG2 morphing devices

The REG IADP objective is to bring the integration of technologies for Regional Aircraft to a further level of complexity with respect to the achievements of Clean Sky GRA. Retaining GRA outcomes, advanced technologies for regional aircraft are being further developed and will be integrated and validated at aircraft level, so as to drastically de-risk their integration on future regional aircraft product, [29].

In the framework of Clean Sky 2 REG-IADP, three morphing wing devices are developed with the aim of improving aerodynamic performance of Leonardo TP90 A/C: drooped nose, morphing flap and morphing winglet. Such high TRL studies include A/C integration, on-ground testing and in-flight validation.

- The *Drooped nose* identifies the Morphing Leading Edge, which is one of the most investigated morphing concepts since many years. In particular, it can be included into the most general active camber-morphing sector, where the main goal is to modify the airfoil camber to improve the A/C aerodynamic performance. Moreover, specific performance requirements have been posed, in terms of C_{L_max} enhancement with respect the reference configuration, equal to 2.4% and 1.7%, considering both trailing and leading edge morphing effects in take-off and landing, respectively. To achieve these benefits, the drooped nose structure was conceived in a “bio-inspired” configuration based on a higher number of compliant rib. This architectural strategy, developed by University Of Milan (PoliMi) allows for reducing the thickness of the ribs and the number of stiffeners, only used as connection between the load paths and the skin. The leading edge target shape change can be obtained without skin length variation. In this way, the morphing LE can change its aerodynamic shape in an efficient way, without generating axial stresses, [30]. A representation of the drooped nose is depicted in Fig. 6.

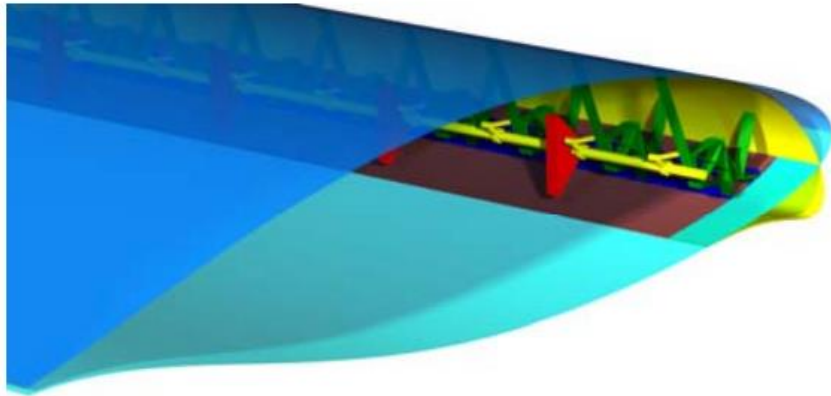


Fig. 6: Drooped Nose structure, [30]

- The *Morphing flap* concept, developed by University of Naples (UniNa), was motivated by the opportunity to replace a conventional double slotted flap with a single slotted morphing flap. This ensures an improvement of high lift performance (C_{L_max} and stall angle), reducing at the same time emitted noise, fuel consumption and the complexity of deployment system. Furthermore, load control and alleviation additional functions were then taken into account: dedicated smart architecture allows for an independent shape-control of the flap tip region along its flight path, [1]. In order to accomplish such benefits, morphing flap was conceived to enable three morphing modes:
 - Morphing mode 1: overall airfoil camber morphing. This function is supposed to be activated during A/C high-lift performance (take-off and landing) while flap is deployed, also allowing for steeper initial climb and descent, noise-abatement trajectories.
 - Morphing mode 2: $+10^\circ/-10^\circ$ (upwards/downwards) deflection of the flap tip segment (from the 90% to 100% of the local chord). Better known as “tip deflection mode”, it is related to the last chordwise segment of the flap and activated in cruise condition for high-speed function (load control).
 - Morphing mode 3: Tip segment twist ($\pm 5^\circ$ along the outer flap span). As well as morphing mode 2, this function is used to modulate the wing load during high lift performance.

Nine smart ribs dividing the structure into eight bays along the span compose morphing flap architecture. Moreover, each rib is segmented along chordwise direction into four consecutive blocks, hinged each other in a finger-like arrangement. Simple and efficient mechanisms are fully integrated into the ribs to

smoothly drive the motion of each block during morphing. The morphing mechanism is embedded in each rib, and actuated by a limited number of **rotary** EMAs placed within the flap bays and connected to the ribs by suitably designed through-shafts, Fig. 7 [31].

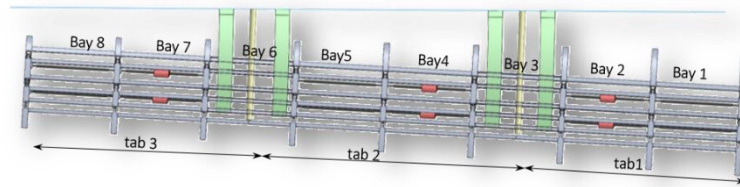


Fig. 7: Morphing flap architecture, top view

- The *morphing winglet* architecture was developed by Italian Aerospace Research Center (CIRA). The driving idea of such a concept was that the camber variation of the winglet trailing edge, combined with the outer wing trailing edge, allows for a cruise well-controlled and modulated wing load distribution. This enables trim drag and induced drag reduction at a parity of lift. The adaptability of the winglet trailing edge is obtained through the rotation of a movable surface divided into four tabs (two upper and two lower) along the span, capable of rotate each other by means of a proper gear ratio, [31]. Then, a rigid plug ensures the interfacing between wing and winglet, Fig. 8.

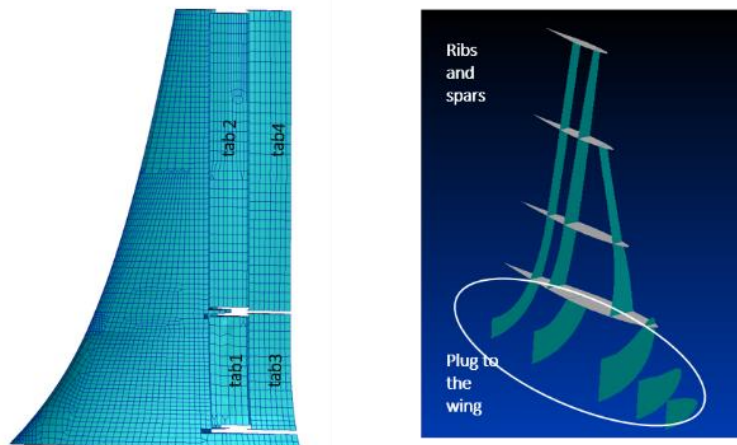


Fig. 8: Morphing winglet Finite Element Model (left) and architecture (right), [31]

Drooped nose is not objective of the presented work, while morphing flaps and winglets characterize the main topic of this thesis. Indeed, such devices are

described in detail in the following sections in terms of structural design and aeroelastic impact at aircraft level.

3 Morphing wing devices

3.1 Morphing flap

3.1.1 Scope and reference geometries

Within the scope of Clean Sky 2 Airgreen 2 (REG-IADP) European research project, a novel multi-modal morphing flap was studied to enhance the aerodynamic performance of the next generation 90-Seat Turboprop regional aircraft along its flight path. The idea driving the proposed true-scale device (spanning 5.15 meters, with a mean chord equal to 0.6 meters) is replacing and enhancing conventional Fowler flap with three new functions, as described below:

- Mode 1: overall airfoil camber morphing, up to $+30^\circ$;
- Mode 2: $+10^\circ/-10^\circ$ (upwards/downwards) deflections of the flap tip segment;
- Mode 3: flap tip “segmented” twist of $\pm 5^\circ$ along the outer flap span.

Morphing mode 1 is assumed operating during take-off and landing phases only to improve A/C high-lift performance. This function allows more airfoil shapes to be available at each flap setting; consequently, a concrete simplification of the flap’s deployment systems may be expected: actuating tracks could be embedded into wing airfoil, and no external fairing is needed. On the other hand, morphing modes 2 and 3 are associated with the last segment of the flap in the chord-wise direction; they are supposed to get going in cruise condition only (flap is in stowed configuration). These modes enable load control functionalities to improve lift/drag ratio, [32].

The investigation domain region selected for the full-scale outer Fowler flap, spanning 5.1 m from the wing kink, with a root chord equal to 0.9 m and a taper ratio equal to 0.75, is depicted in Fig. 9.

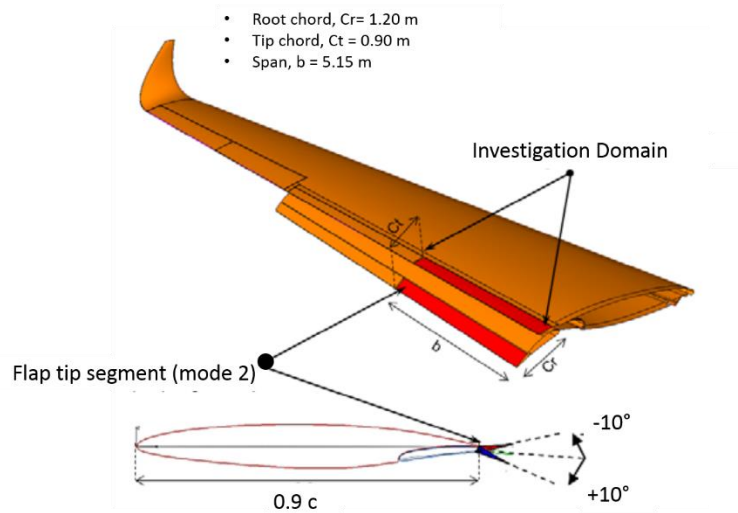


Fig. 9: Morphing flap investigation domain, [32]

The starting point for the development of the presented three-modal morphing flap was provided by the general structural layout discussed in [33] - [34] and successfully validated by experimental via in the framework of the JTI-Clean Sky project (GRA-ITD Low Noise Domain). The novel architecture was conceived responding to all the project design requirements.

3.1.2 Aerodynamics and Benefits

As known, when dealing with large civil aircraft, the design of any movable control surface must observe three fundamental requirements:

1. “Demonstrate that the device is able to support limit loads without permanent detrimental deformation and that the deformation levels don’t interfere with safe operation” (*EASA CS 25.305(a)*, limit loads);
2. Capability to withstand ultimate loads without any failure in actuation systems;
3. “Freedom from aeroelastic instability must be shown up to the speeds defined in CS 25.629 (b)”, (aeroelastic stability requirements).

Limit load to be used in the preliminary design can be considered by invoking the airworthiness regulation according to which a control surface must be capable of providing a rotation angle equal to 33% of its maximum value corresponding with A/C dive speed [2]. [32] reports the limit load condition obtained by using

an in-house 2D Doublet Lattice Method (DLM) code, herein showed in Table 1 for the sake of completeness.

Tab rotation (down)	+5 deg
Tab mean geometric chord	0.236 m
Pressure coefficient (upper),	0.3247
Pressure coefficient (lower),	0.5011
Dynamic pressure,	12005 Pa
Dynamic Pressure (upper), $q * C_{p,UP}$	3898 Pa
Dynamic Pressure (lower), $q * C_{p,LOW}$	6015 Pa
Force resultant (upper), F_{UP}	2378 N
Force resultant (lower), F_{LOW}	3668 N
Hinge moment around tab hinge axis, MB_3	475.8 N*m

Table 1: Aerodynamic values in limit load condition, [32]

At preliminary design stage, a pressure uniform distribution on tabs upper and lower external surfaces was assumed, as shown in Fig. 10.

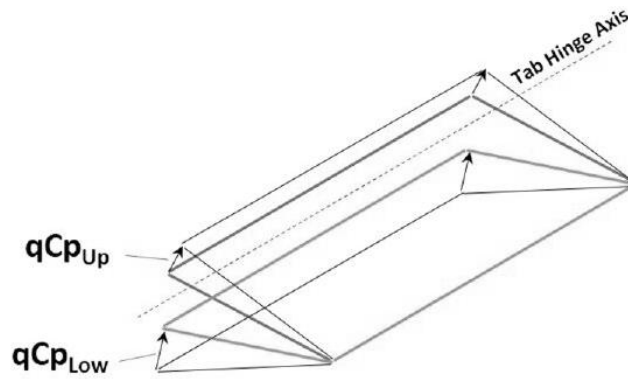


Fig. 10: Aerodynamic pressure uniform distribution on tabs surfaces, [32]

Hence, when designing multifunctional morphing structures, several requirements need to be observed to make the structures capable of withstanding the aerodynamic loads and, at the same time, to enhance aircraft performance and extend mission profiles, such as actuators power required and weight. This aspect leads the way toward a successful integration of actuation systems in large airplanes.

3.1.3 Morphing flap architecture

The successful technology demonstration of a bi-modal morphing flap (2MMF) in JTI-Clean Sky (GRA-ITD) project scenario drove the design of the herein presented three-modal morphing flap (3MMF), objective of the Clean Sky 2 REGIADP AG2 project. Several design improvements have been achieved, if comparing 3MMF with 2MMF, [32].

Nine articulated ribs in a finger-like configuration enable flap morphing capabilities. Each rib is divided into four consecutive blocks, namely B0, B1, B2 and B3, hinged each other by means of cylindrical hinges (A, B, C), positioned along the camber-line, Fig. 11.

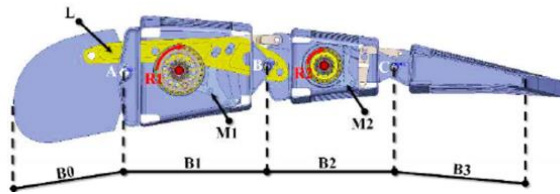


Fig. 11: Morphing flap articulated rib, [32]

Not adjacent block B0 and B2 are connected by means of a linking beam element (L), forcing the camber line segments to be geared in their relative rotations.

Aiming to reach specific target shapes (Fig. 12), an equivalent rotation of the flap edge around A hinge was taken into account in morphing mode 1, Fig. 13. Block B1 contains the inner leverage M1, connecting blocks B1 and B2; it amplifies the actuator torque. Such a leverage motion is ensured by a rotary actuator, R1, acting along the shaft.

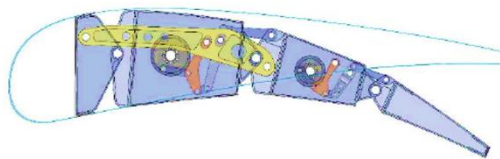


Fig. 12: Morphing flap target shape, mode 1, [32]

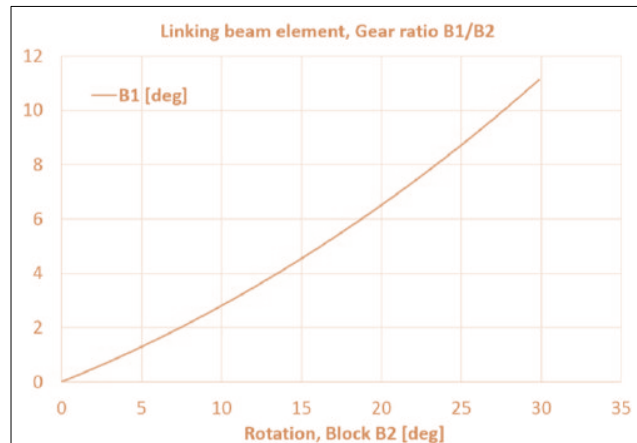


Fig. 13: B1/B2 gear ratio trend, [32]

Leverage M1 motion enables relative rotation of block B2 with respect to B1, geared through the linking element, L. Moreover, a second leverage (M2) - positioned into B2 - connects flap trailing edge (B3) to B2, driven by actuator R2. Thanks to mechanism M2, flap tip segment can rotate around the hinge C, ensuring morphing mode 2 and 3. Both M1 and M2 mechanisms are activated during morphing mode 1 to reach the target shape.

For what concerns morphing modes 2 and 3, only the mechanism M2 is activated, while keeping M1 fixed. An optimization of the hinges positions of both M1 and M2 mechanisms was considered to maximize the output and input torque ratio – namely, mechanical advantage - mechanical advantage –, also observing the encumbrance in B1 and B2.

A multi-box arrangement was adopted to transfer the ribs kinematic to the overall flap structure. In detail, each box is defined as the single-cell structural part included:

- in span-wise direction, within homologue blocks of consecutive ribs;
- in chord-wise direction, by consecutive spars.

When ribs actuation is activated, the synchronized motion of all the boxes ensures the morphing flap external shape changing; in a different way, when actuators are locked, elastic stability of the structure is maintained although the aerodynamic loads.

Each box was preliminarily sized referring to an equivalent static scheme based on the following assumptions:

- lumped elastic properties;

- Spars, rib plates and skin panels made of AL2024-T5 alloy;
- Ultimate load obtained multiplying limit loads by 1.5 (safety factor);
- Limit load condition: outboard flap in landing configuration, aircraft angle of attack equal to 0.57° , dynamic pressure equal to 5858 N/m^2 , $F_{Z,tot} = 40000N$;
- Boxes were considered as separated structures each other;
- Fixed rib planes adjacent to the deployment system tracks; this made possible to transfer internal solicitations from the morphing flap to the deployment system (Fig. 14).

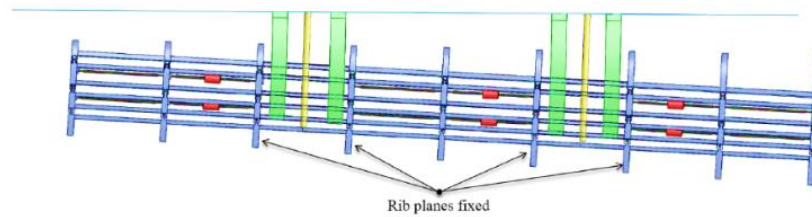


Fig. 14: Morphing flap preliminary design assumption, [32]

Elementary methods were adopted during the structural preliminary design to obtain the thickness of the front (rear) spar web, the thickness of (upper/lower) skin panels; the thickness of the rib plate was assumed to be equal to the maximum value among the ones of spars and skin panels.

Referring with a limit load case, preliminary Finite Elements analyses results confirmed the assumptions made, [32].

In an advanced design loop, further developments were carried out the design of the transmission line to reduce number of rotary actuators enabling morphing functionalities. For that purpose, referring to the limit load condition, a through shafts solution was adopted in the transmission line to enable the torque transfer to three rib blocks with a single rotary motor, Fig. 15.

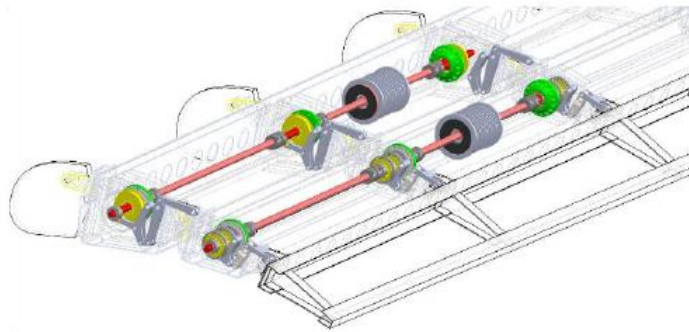


Fig. 15: Section view of through shaft actuation concept, [32]

A segmented shaft transfers the torque provided by the actuators (R1 and R2) to the Harmonic Drive gear box; each gear box is enabled to transfer the torque to the crank of the inner pertinent mechanism (M1 or M2), being jointed to the rib block plate (Fig. 16).

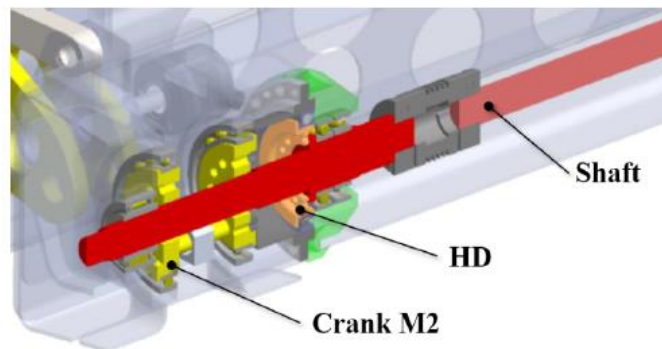


Fig. 16: Wireframe view of through shaft actuation concept, [32]

Friction effects between movable parts in relative motion each other are reduced by using proper ball bearings.

It is important to outline how the total weight reduction was always observed as structural target; indeed, at each design loop, a great amount of components was reduced (i.e. rotary actuators, smart ribs). According to [35], a conventional flap system weight is around the 3 per cent of the airplane Maximum Zero-Fuel Weight (MZFW). Since the final weight of the outboard three modal morphing flap results equal to 92.5Kg, the 12 per cent of weight saving has been estimated with respect to a conventional outboard flap (104.6Kg) for a regional Turboprop aircraft.

3.2 Morphing winglet

3.2.1 Scope and reference geometries

Research on morphing aircraft structures aims to wing design optimization by considering co-factors involving both aerodynamics and structures. Morphing devices applications can bring to several benefits in terms of aircraft performance, as literature studies teach. Among such applications, shape-changing winglets can enhance Lift-on-Drag ratio in off-design conditions and reduce aerodynamic wing loads by providing adapted geometry and wing lift distribution throughout the A/C flight envelope. This can potentially lead the way toward adaptive winglets application to the next generation aircraft. For that purpose, the structural design of a multi-modal morphing winglet is collocated within the scope of Clean Sky 2 Regional Aircraft IADP (see section 2), made in compliance with the pertinent requirements posed by the airworthiness regulations.

The morphing winglet concept observes the following assumptions:

- Morphing winglet system chord equal to the 40% of the mean winglet chord;
- Deflection range = $[-15^\circ, +10^\circ]$ (negative deflections when reducing root bending moment).

Morphing is ensured by a dedicated mechanism composed by movable surfaces (upper and lower), whose deflection is driven by dedicated actuators, [36] – [37]. Upper and lower surfaces are shown in Fig. 17, together with morphed shapes. Fig. 18 shows two possible settings of the morphing winglet device achieved by moving independently upper and lower surfaces, respectively.

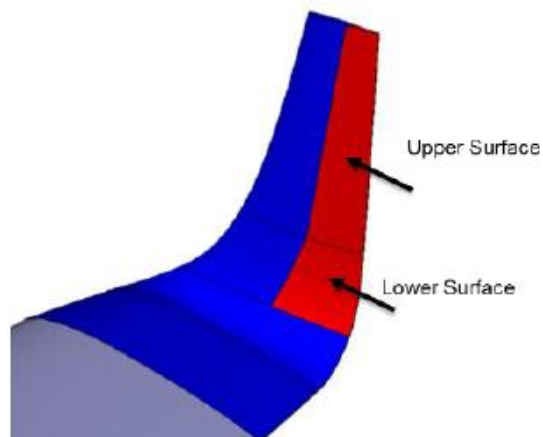


Fig. 17: Movable surfaces of the morphing winglet, [38]

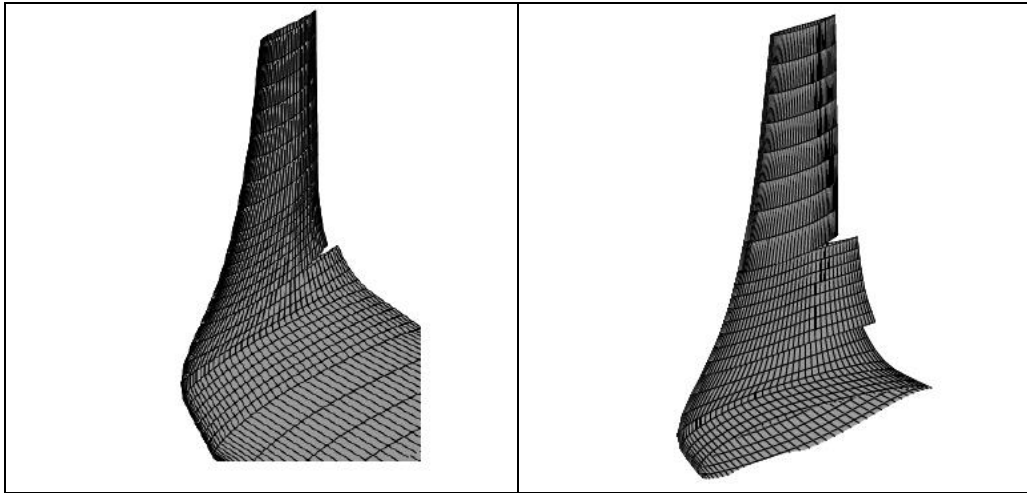


Fig. 18: Upper (on left) and lower (right) deflection, [38]

3.2.2 Aerodynamics and Benefits

Accurate aerodynamic assessments were performed to predict the enhanced aerodynamic performance (estimated about 3%) ensured by the integration of morphing winglets on a regional aircraft. Such results were gained through a panel-based method (Morino) applied to the isolated wing, corrected by 2D Navier Stokes results (Quasi 3D results), together with the drag increment related to the nacelle and the body [37] – [39].

CIRA performed aerodynamic simulations to evaluate the worst hinge moment values and sizing loads required for the design of the morphing winglet structure. Fig. 19 shows an example of C_p distribution on the morphing winglet for negative deflections of both the upper and lower surfaces.

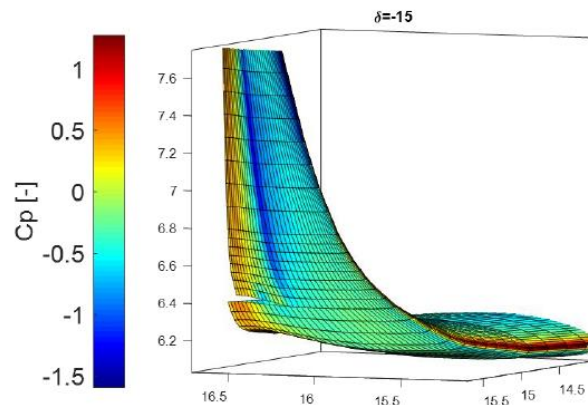


Fig. 19: Example of C_p distribution on the morphing winglet for negative deflections of both the upper and lower surfaces, [38]

Lift on Drag improvements are achieved by separately controlling the downward deflections of the control surfaces in climb and cruise conditions. On the other hand, aerodynamic assessments showed that varying the angles between inner and outer winglet may lead to further aerodynamic benefits [36].

3.2.3 *Morphing winglet architecture*

The main body of the winglet fully embeds the morphing architecture, conceived to reduce the induced drag by modulating span-wise aerodynamic loads. Moreover, such architecture allows also for load alleviation functions, by means of negative deflections of the movable parts. Winglet morphing capabilities are ensured by relative rotations of three consecutive hinge-connected blocks, namely B0, B1 and B2, Fig. 20. The term “block” refers to the structural part including a pair of segments connected by a spar box. Both lower and upper electromechanical linear actuators are located in B1; in order to activate morphing, each actuator induces B1 rotation around its hinge axis through a rigid rod. Great part of the incoming loads conveys on such structural element, making its design very crucial, Fig. 21. Fig. 22 shows the EMA actuators chosen for the morphing activation.

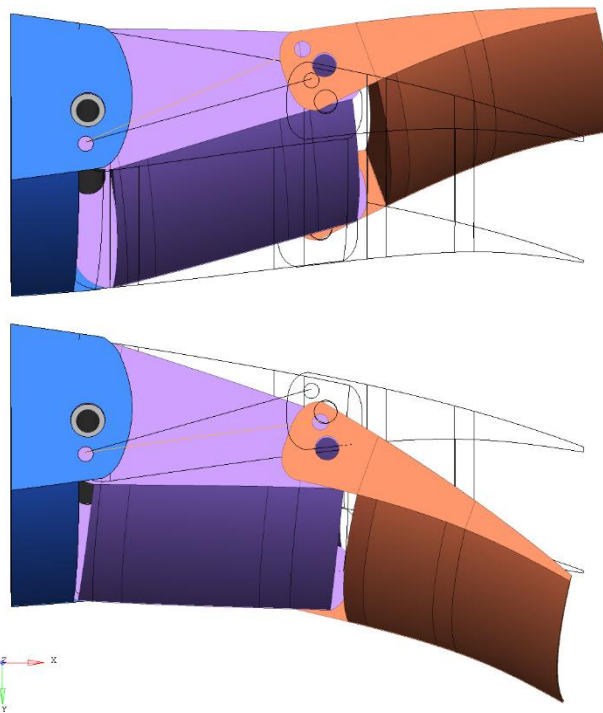


Fig. 20: Morphing blocks of the finger-like architecture, [40]

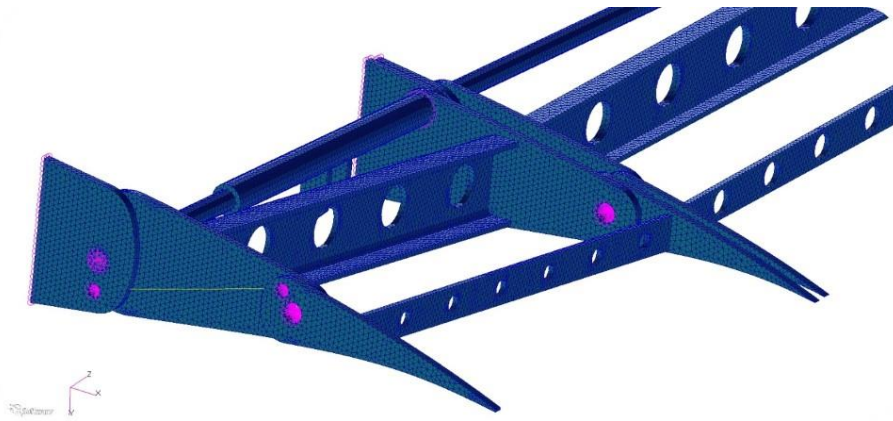


Fig. 21: Detail of the morphing winglet architecture, [38]

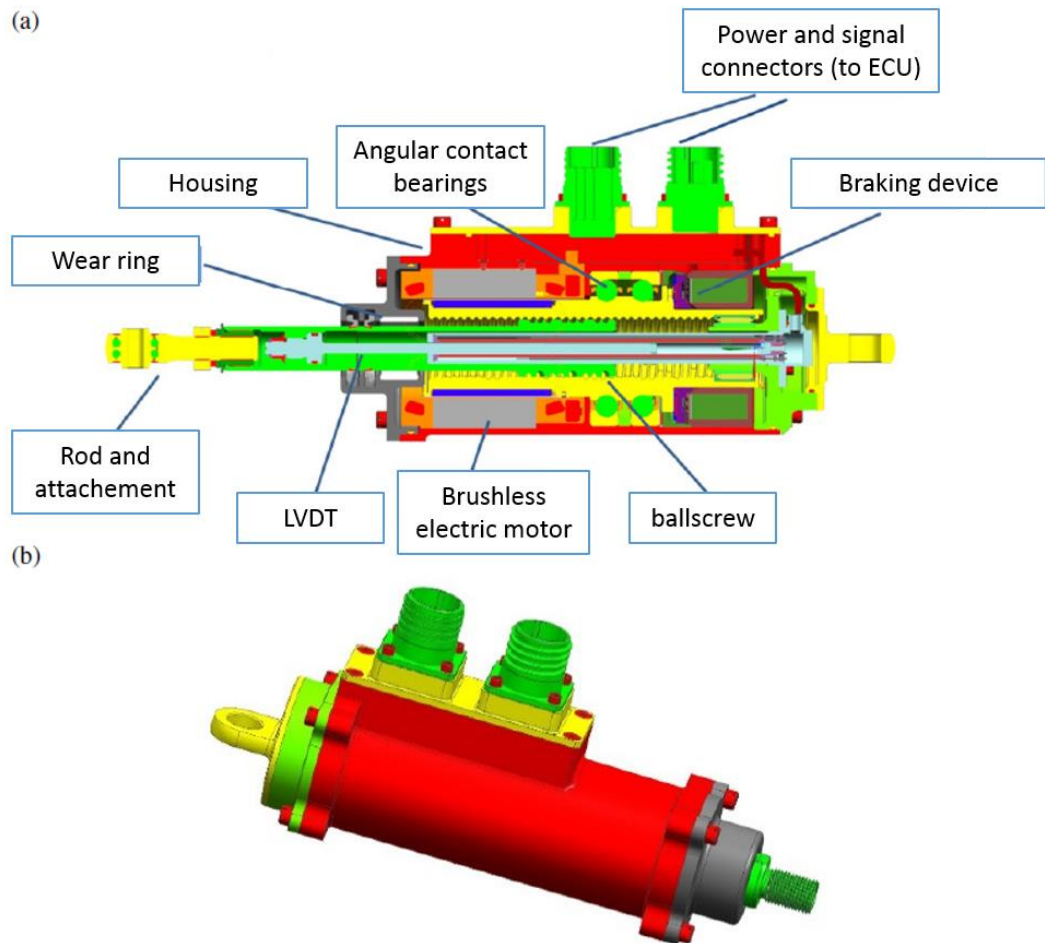


Fig. 22: EMA actuators: a) sectional and b) external view, [37]

The system conceived in such a way results at Single Degree of Freedom; the rotation of consecutive blocks occurs according with a proper gear ratio. B0 is also defined as “dead box”, since it is rigidly connected to the winglet rear spar (non-morphing part). The skin covering winglet trailing edge (upper and lower) is segmented into two panels for each block, properly connected to the ribs edges and spars underneath it. The materials considered for movable and not movable parts were different; in particular:

- Carbon-fiber, for the not movable part;
- Aluminum alloy, for the movable parts.

Material mechanical properties are reported in Table 2

Mechanical Property	Carbon-fiber	Aluminum Alloy
Young Modulus, E [MPa]	33000	70000
Poisson Coefficient, ν	0.32	0.30
Density, ρ [Ton/mm ³]	$1.7 \cdot 10^{-9}$	$2.8 \cdot 10^{-9}$

Table 2: Winglet materials mechanical properties

Morphing winglet weight, comprehensive of actuators and ECU, is equal to 36.90 Kg, [31].

4 Aeroelasticity

4.1 Introduction

Aeroelasticity is the science involving studies about the mutual interaction effects among elastic, inertial and aerodynamic forces. These interactions (Fig. 23) may lead to instabilities and/or load increases with detrimental impact on the integrity of the system. Airworthiness standards as JAR, FAR, VLA provide for arrangements for flutter and other instability phenomena to ensure flight safety by means of an adequate structural design. According to such standards, the absence of aeroelastic instabilities must be proved through analyses, flight test or a combination of both.

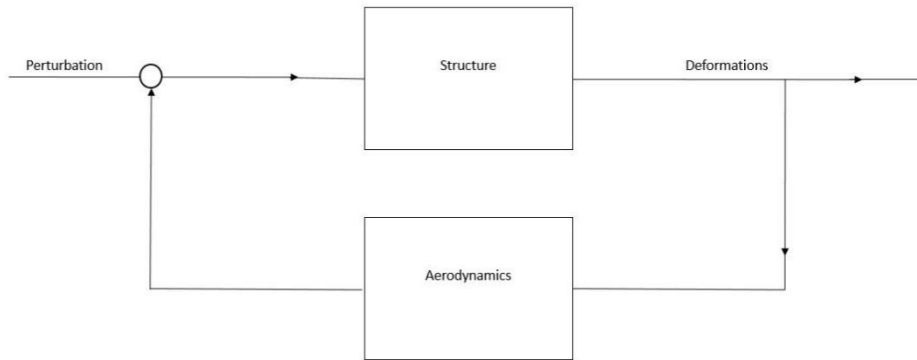


Fig. 23: Aeroelasticity conceptual scheme, [41]

Proper models representative of the aircraft behavior have to be conceived for analytical and experimental analyses. In general, the models can be divided into two classes.

1. Dynamic model, including the structural and inertial ones;
2. Aerodynamic model.

4.1.1 Structural Model

The structural model simulates the elastic behavior of the aircraft.

The structural models can be divided in two categories:

1. Stick-beam model;
2. Finite Element model.

The aforementioned distinction is not completely marked, since the two models may co-exist. For this reason, the choice of the scheme to adopt strongly depends on the structural complexity and on the experience gained dealing with similar configurations.

However, the model must properly describe the links among the movable surfaces and the commands, and must be “adaptable”, to include all the stiffness variations in potentially association with the aeroelastic instabilities, [43]. Particular attention must be paid in modelling the interface areas that are fundamental for the evaluation of flutter or/and loads induced by aerodynamic turbulence:

- Wing-engine;
- Wing-fuselage;
- Tails-fuselage.

4.1.2 Inertial Model

The inertial model simulates the mass distribution of the whole aircraft. This allows for the transition from an almost continuous representation of the aircraft mass to one based on a set of lumped masses, with their moments of inertia.

The results of the dynamic model are normal modes, frequencies and generalized masses.

4.1.3 Aerodynamic Model

The aerodynamic model simulates the aerodynamic behavior of the aircraft. It must involve the use of unsteady aerodynamics for compressible fluid (two-dimensional strip theory or three-dimensional panel theory).

The choice of the theory strongly depends on the complexity of the lifting surfaces and on the flight envelope speed of the aircraft.

4.2 Aeroelastic stability equations

4.2.1 Generalized Aerodynamic Forces

Lifting surfaces are divided into N panels (Fig. 24).

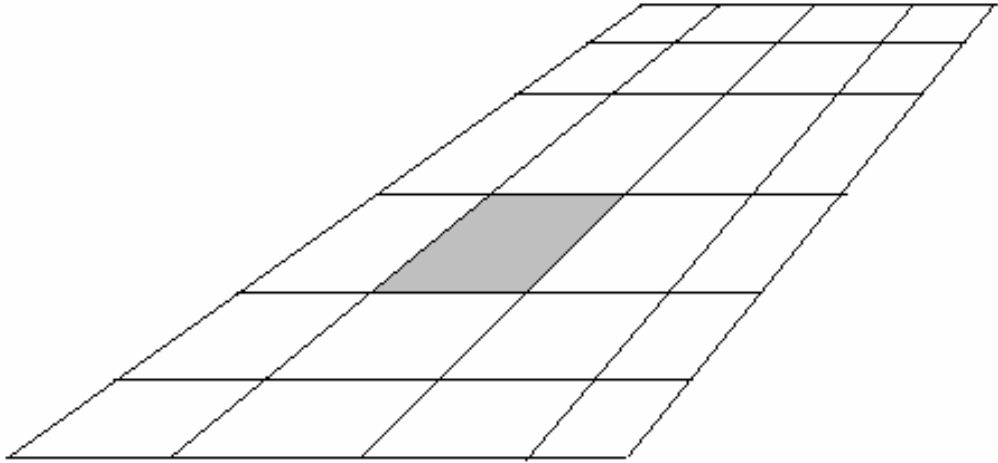


Fig. 24: Aerodynamic Lattice, [41]

For each oscillating panel, the *normalwash* is associated to the pressure difference by means of the relation:

$$\frac{w}{v_{\infty}} = \bar{\bar{A}} * \underline{\Delta C_p} \rightarrow \underline{\Delta C_p} = \bar{\bar{A}}^{-1} \frac{w}{v_{\infty}}$$

While the relation expresses the elementary aerodynamic forces:

$$\underline{\Delta F} = q \bar{\bar{\Delta S}} * \underline{\Delta C_p} \rightarrow \underline{\Delta F} = q \bar{\bar{\Delta S}} \bar{\bar{A}}^{-1} \frac{w}{v_{\infty}}$$

Where:

$\bar{\bar{A}}^{-1}(r, kr, M)$ = Aerodynamic Influence Matrix, depending on the geometry (r), reduced frequency ($kr = wcr/V$) and Mach number (M);

$\bar{\bar{\Delta S}}$ = Diagonal matrix of panels' area;

$q = \frac{1}{2}\rho v^2$ = aerodynamic pressure of asymptotic flow;

$$\frac{w}{v_{\infty}} = \left\langle \frac{d}{dx} + j \frac{kr}{cr} \right\rangle \underline{h_c} = \bar{\bar{D}} \underline{h_c}$$

$\overline{\overline{D}}$ = substantial derivative matrix;

x = asymptotic flow direction;

$\underline{h_c}$ = normal displacements vector in correspondence with control points.

The virtual work of the aerodynamic forces is given by:

$$\delta L = \delta \underline{h_i^t} \underline{\Delta F} \rightarrow q \delta \underline{h_i^t} \overline{\overline{\Delta S \bar{A}^{-1} \overline{\overline{D}}}} \underline{h_c} \quad (1)$$

where:

$\underline{h_i}$ = normal displacements vector in correspondence with integration points.

Both h_i and h_c are related to the structural displacements Z_{st} through interpolation matrix depending exclusively on the geometry.

$$\underline{h_c} = \overline{\overline{G_{AK}^C(r)}} \underline{Z_{st}} \underline{h_i} = \overline{\overline{G_{AK}^I(r)}} \underline{Z_{st}} \quad (2)$$

By integrating the Eq. 2 into Eq. 1, the latter becomes:

$$\delta L(\underline{Z_{st}}) = q \delta \underline{Z_{st}}^T \overline{\overline{G_{AK}^I(r)}}^T \overline{\overline{\Delta S \bar{A}^{-1} \overline{\overline{D}}}} \overline{\overline{G_{AK}^C(r)}} \underline{Z_{st}} \quad (3)$$

By projecting the structural displacements in the normal mode space, $\underline{Z_{st}} = \overline{\overline{\Phi(r)}} \underline{\eta(t)}$, where:

$\overline{\overline{\Phi(r)}}$ = normal modes matrix;

$\underline{\eta(t)}$ = lagrangian coordinates vector,

The virtual work of aerodynamic forces expressed as a function of η is:

$$\delta L(\underline{\eta}) = q \delta \underline{\eta}^T \overline{\overline{Q(kr, M)}} \underline{\eta},$$

$$\text{With } \overline{\overline{Q(kr, M)}} = \overline{\overline{\Phi^T}} \overline{\overline{G_{AK}^I(r)}}^T \overline{\overline{\Delta S \bar{A}^{-1} \overline{\overline{D}}}} \overline{\overline{G_{AK}^C(r)}} \overline{\overline{\Phi}}.$$

4.2.2 Impedance matrix

Kinetic energy (T), elastic energy (U) and dissipation function (D) have the following expressions, [41]:

$$T = (1/2)\underline{\dot{Z}}^T \bar{\bar{M}} \underline{\dot{Z}}$$

$$U = (1/2)\underline{Z}^T \bar{\bar{K}} \underline{Z}$$

$$D = (1/2)\underline{\dot{Z}}^T \bar{\bar{C}} \underline{\dot{Z}}$$

And by introducing the modal coordinates:

$$T = (1/2)\underline{\dot{\eta}}^T \bar{\bar{M}}_g \underline{\dot{\eta}}$$

$$U = (1/2)\underline{\eta}^T \bar{\bar{K}}_g \underline{\eta}$$

$$D = (1/2)\underline{\dot{\eta}}^T \bar{\bar{\sigma}}_g \underline{\dot{\eta}}$$

Where:

$\bar{\bar{M}}_g$ = generalized diagonal mass matrix

$\bar{\bar{K}}_g$ = generalized diagonal stiffness matrix

$\bar{\bar{\sigma}}_g$ = modal damping matrix (diagonal under the Basile Hypothesis).

Given the Lagrange relation:

$$\frac{d}{dt} \frac{\partial T}{\partial \underline{\dot{\eta}}} + \frac{\partial D}{\partial \underline{\dot{\eta}}} + \frac{\partial U}{\partial \underline{\eta}} = \frac{\partial L}{\partial \underline{\eta}}$$

Its Fourier transform in presence of the external forces, $\underline{F}_{g \text{ ext}}(j\omega) = \bar{\bar{\Phi}}^T \underline{F}_{\text{ ext}}(j\omega)$, totally independent from the movement of the structure leads to the aeroelastic equilibrium equation:

$$\bar{\bar{H}}(j\omega; V_\infty) \underline{\eta}(j\omega) = \underline{F}_{g \text{ ext}}(j\omega)$$

Where:

$$\bar{\bar{H}}(j\omega; V_\infty) = [(j\omega)^2 \bar{\bar{M}}_g + (j\omega) \bar{\bar{\sigma}}_g + \left(\bar{\bar{K}}_g - \frac{1}{2} \rho V_\infty^2 \bar{\bar{Q}}(kr, M) \right)] \quad (4)$$

Is the **impedance matrix**, the inverse of which is the **transfer matrix**.

Both of them are dependent from the flight speed.

The time-domain solutions of the generalized coordinates are obtained by the inverse Fourier transform of the (4), as expressed in the (5):

$$\underline{\eta}(t) = \frac{1}{2\pi} \int_{-\infty}^{+\infty} \bar{\bar{H}}^{-1}(j\omega; V_\infty) \underline{F}_{g \text{ ext}}(j\omega) \exp(j\omega t) d\omega \quad (5)$$

The asymptotic stability¹ of the system under an imposed unit impulse forcing is ensured by the condition:

$$\int_{-\infty}^{+\infty} |H^{-1}(j\omega; V_\infty)| d\omega \leq 0$$

The transfer matrix at a fixed speed is expressed as a polynomial ratio:

$$\bar{\bar{H}}^{-1}(j\omega; V_\infty) = \frac{\sum_{i=0}^n \bar{\bar{A}}_i(j\omega)^i}{\sum_{i=0}^n b_i(j\omega)^i}$$

Where the numerator is a polynomial of real matrixes of order n , while the denominator is a scalar polynomial with real coefficients of order m , equal to the number of the generalized coordinates multiplied by 2. Due to the system causality, n at maximum can reach the value m . In order to guarantee the dynamic stability of the system, the denominator cannot have any root with negative real part. In other words, the poles of the rational representation of the transfer matrix must be included into the negative quadrant of the complex plane. The denominator is the determinant of the impedance matrix $\bar{\bar{H}}(j\omega; V_\infty)$.

A numerical and very efficient method to calculate the determinant of a matrix is based on the calculus of its eigenvectors.

Flutter speed is defined as the speed value corresponding to a pole with real part equal to zero at least.

4.3 Classification of the methods for flutter evaluation

The aeroelastic stability equation in absence of the constant term has the following expression ([41] – [43]):

$$-\omega^2 \bar{\bar{M}} \underline{\eta} + j\omega \bar{\bar{\sigma}}_G \underline{\eta} + \bar{\bar{K}} \underline{\eta} = \left(\frac{1}{2}\right) \rho v^2 \bar{\bar{Q}}(kr) \underline{\eta} \quad (6)$$

¹ $|\underline{\eta}(t)| \leq 0$, if $t \rightarrow \infty$

With kr is the *reduced frequency*, equal to $\omega \underline{cr}/v$ (\underline{cr} is the reference length).

The methods to calculate the roots of the (6) as functions of the speed can be divided into three classes:

- a) K methods;
- b) PK methods;
- c) Methods of state equations.

4.3.1 K methods

4.3.1.1 K method, First version

By using the definition of reduced frequency discussed in §4.3 and by substituting the following expression:

$$v^2 = \left(\frac{\omega \underline{cr}}{kr}\right)^2$$

The Eq. 6 becomes:

$$[j\omega \overline{\sigma}_G + \overline{K}] \underline{\eta} = \omega^2 \left[\frac{\rho \underline{cr}^2}{2} * \frac{\overline{Q}(kr)}{kr^2} + \overline{M} \right] \underline{\eta}$$

And considering the hysteretic damping $\overline{\sigma}_G = \frac{g}{\omega} \overline{K}$:

$$(1 + jg) \overline{K} \underline{\eta} = \omega^2 \left[\frac{\rho \underline{cr}^2}{2} * \frac{\overline{Q}(kr)}{kr^2} + \overline{M} \right] \underline{\eta}$$

From which:

$$\lambda \underline{\eta} = \overline{A} \underline{\eta},$$

where:

$$\lambda = \lambda_R + j\lambda_I = \frac{1+jg}{\omega^2}$$

$$\overline{A} = \overline{K}^{-1} \left[\frac{\rho \underline{cr}^2}{2} * \frac{\overline{Q}(kr)}{kr^2} + \overline{M} \right]$$

The roots are found by means of the solution of the eigenvalues of a complex matrix, according to what described as follows:

1. Reduced frequency fixed, Kri;
2. \overline{Q} (Kri;) matrix evaluation;
3. \overline{A} matrix construction:

The calculus must be done according to descending values of the reduced frequency: $Kr_1 > Kr_2 > Kr_3$, etc.

In this version, K – method is very quick. Nevertheless, since it requires a non-singular matrix, this method can deal neither with the rigid modes of the aircraft nor with the control surfaces modes with free commands. Talking about the latter, the difficulty can be overcome by introducing low values of stiffness.

4.3.1.2 K method, Second version

The limitation of the first version of the K-method can be prevented through a different expression of the aeroelastic stability equation. By imposing as LHS of the (6):

$$\omega^2 = \frac{(Vkr)^2}{(cr)}$$

It becomes:

$$-V[(kr/cr)^2 * \bar{M} + \left(\frac{\rho}{2}\right) * \bar{Q}(kr)]\underline{\eta} + (1 + jg)\bar{K}\underline{\eta} = 0 \quad (7)$$

From which:

$$\lambda\underline{\eta} = \bar{A}\underline{\eta}$$

Where:

$$\lambda = \frac{v^2}{1+jg} \bar{A} = \left[\left(\frac{kr}{cr}\right)^2 * \bar{M} + \left(\frac{\rho}{2}\right) * \bar{Q}(kr)\right]^{-1} * \bar{K} \quad (8)$$

For each step, a complex matrix will be inverted. The latter formulation allows for the calculation of the static divergence speed. Indeed, on the basis of the expression of \bar{A} for zero reduced frequency:

$$\lambda\underline{\eta} = \left[\left(\frac{\rho}{2}\right) * \bar{Q}(0)\right]^{-1} * \bar{K} * \underline{\eta} \quad (9)$$

And λ is the divergence speed squared. By imposing $\omega = kr = 0$ in the (1), the following expression is obtained:

$$V^2 \underline{\eta} = \left[\left(\frac{\rho}{2} \right) * \bar{Q} (0) \right]^{-1} * \bar{K} * \underline{\eta} \quad (10)$$

The term $C = (g/\omega)*K$ does not alter the matrix A structure, but provides for the imaginary part of the eigenvalue.

The K methods are not much used in the industrial field, since not including the structural damping.

4.3.2 PK methods

4.3.2.1 PK method, First version (English version)

In the (6), the aerodynamic matrix is split into its real and imaginary parts:

$$\left(\frac{1}{2} \right) \rho v^2 [\bar{Q}_R + j \bar{Q}_I] \underline{\eta}$$

By considering:

$$\left(\frac{1}{2} \right) \rho v^2 [j \bar{Q}_I] \underline{\eta} = \left(\frac{1}{2} \right) \rho v \left(\frac{v}{cr * \omega} \right) (cr * \omega) j \bar{Q}_I \underline{\eta} = \left(\frac{1}{2} \right) \rho v cr \frac{\bar{Q}_I}{kr} j \omega \underline{\eta}$$

And:

$$-\omega^2 \underline{\eta} = \ddot{\eta}; j \omega \underline{\eta} = \dot{\eta}$$

The (6) becomes:

$$\bar{M} \ddot{\eta} + [\bar{\sigma}_G - \left(\frac{1}{2} \right) \rho v cr \frac{\bar{Q}_I}{kr}] \dot{\eta} + [\bar{K} - \left(\frac{1}{2} \right) \rho v^2 \bar{Q}_R] \underline{\eta} = 0$$

And in a compact expression:

$$\bar{M} \ddot{\eta} + \bar{C} \dot{\eta} + \bar{K} \underline{\eta} = 0 \quad (11)$$

By imposing $\underline{\eta} = \underline{\eta} e^{pt}$:

$$p^2 \bar{M} \underline{\eta} + p \bar{C} \underline{\eta} + \bar{K} \underline{\eta} = 0 \quad (12)$$

The Eq. 12 is an eigenproblem of an II order complete system. Its roots, in general complex, will have imaginary part depending on the pulsation, and the real part depending on the damping.

If N modes are present, the (12) is a second-degree and N-order system, due to a first-degree and 2N-order one:

$$\begin{bmatrix} I & 0 \\ 0 & M \end{bmatrix} p \begin{bmatrix} \eta \\ p\eta \end{bmatrix} - \begin{bmatrix} 0 & I \\ -K_s & -C_s \end{bmatrix} \begin{bmatrix} \eta \\ p\eta \end{bmatrix} = 0 \quad (13)$$

By considering:

$$\begin{bmatrix} \eta \\ p\eta \end{bmatrix} = Y$$

The Eq. 13 becomes:

$$pY = AY$$

With:

$$A = \begin{bmatrix} 0 & I \\ -M^{-1}K_s & -M^{-1}C_s \end{bmatrix}$$

A is a real matrix.

The “free” parameter is the reduced frequency for the K-method, while is the speed for the PK-method.

The calculation procedure is the following:

For a fixed speed value, as a first step the aerodynamic and A matrices are calculated for a reduced frequency $K_{1,0}$ close to zero. Then, the eigenvalues are evaluated and ordered by increasing values of the imaginary part; the ω deriving from the imaginary part of the first eigenvalue $\omega_{1,0}$ and the reduced frequency $K_{1,1} = \omega_{1,0} * cr/V$ associated with it are calculated.

If $|K_{1,0} - K_{1,1}| > \varepsilon$ (where ε is an arbitrarily small real number indicative of the precision of the solution), the A matrix and the eigenvalues for this new reduced frequency are recalculated. After ordering the eigenvalues by the imaginary part and while indicating the pulsation of the first mode with $\omega_{1,1}$, $K_{1,2} = \omega_{1,1} * cr/V$ is then calculated. If $|K_{1,1} - K_{1,2}| < \varepsilon$, the iteration on the first mode is stopped and the next level is reached by taking as initial value for the pulsation the ω_2 obtained after the previous iteration. The process continues until the convergence is reached for all the modes, corresponding with the fixed value of V.

For the general mode i, the complex eigenvalue $p_R + jp_i$ is associated with the roots of a mass-spring-damper dynamic system:

$$p = -\zeta\omega + j\omega\sqrt{(1-\zeta^2)}, p_R = -\zeta\omega, p_i = \omega\sqrt{(1-\zeta^2)}$$

From the ratio $\frac{p_i}{p_R} = \frac{\sqrt{(1-\zeta^2)}}{\zeta}$ the quantity $\zeta\omega$ can be evaluated and then $\omega = -\frac{p_R}{\zeta}$.

Compared to the K method, the PK-method is more costly from a computational point of view. Anyway, it allows for taking into account the structural damping and, in this version (called English version), the solutions can be obtained regardless of the previous solutions.

4.3.2.2 PK method, Second Version (Continuation method)

The aeroelastic stability equation:

$$\left[p^2 M + p\sigma + K - \frac{1}{2}\rho V^2 Q(kr) \right] \eta = 0 \quad (14)$$

can be considered as a vectorial equation as a function of p, η :

$$\underline{F}(p, \eta) = 0 \quad (15)$$

By adding to the (15) a normalization condition for η :

$$\eta^t * W * \eta = 1$$

And by imposing:

$$G(\eta) = \eta^t * W * \eta - 1 = 0 \quad (16)$$

The Eq. 15 and 16 can be seen as non linear equations system as functions of p and η :

$$\underline{F}(p, \eta) = 0 \quad (17)$$

$$G(\eta) = 0$$

By expanding the (17) about a fixed speed value point, p_0, η_0 :

$$\begin{aligned} \underline{F}(p, \eta) &= \underline{F}(p_0, \eta_0) + \frac{\partial F}{\partial p} * \Delta p + \frac{\partial F}{\partial \eta} * \Delta \eta \\ G(\eta) &= G(\eta_0) + \frac{\partial G^R}{\partial \eta} * \Delta \eta \end{aligned} \quad (18)$$

Where:

$$\begin{aligned} \underline{F}_p &= \frac{\partial F}{\partial p} = [2p M + \sigma - \frac{1}{2} \rho v^2 \frac{\partial Q(kr)}{\partial kr} \frac{\partial kr}{\partial p}] * \eta \\ \underline{F}_\eta &= \frac{\partial F}{\partial \eta} = [p^2 M + p\sigma + K - \frac{1}{2} \rho v^2 Q(kr)] \\ \underline{G}_\eta^R &= \frac{\partial G^R}{\partial \eta} = 2 \eta^T * W \end{aligned}$$

\underline{G}_η^R row vector.

By using the (17), the (18) becomes:

$$\begin{aligned} -\underline{F}(p_0, \eta_0) &= \underline{F}_p * \Delta p + \underline{F}_\eta * \Delta \eta \\ -G(\eta_0) &= \underline{G}_\eta^R * \Delta \eta \end{aligned} \quad (19)$$

And by imposing:

$$\underline{V}_1 = F_\eta^{-1} * \underline{F}(p_0, \eta_0); \underline{V}_2 = F_\eta^{-1} * \underline{F}_p$$

From the first of the (19):

$$\Delta \eta = -\underline{V}_1 - \underline{V}_2 * \Delta p \quad (20)$$

And by replacing in the second of the (19):

$$\Delta p = \frac{G_{\eta}^T * V_1 - G(\eta_0)}{G_{\eta}^T * V_1} \quad (21)$$

Known Δp , from the (20) $\Delta \eta$ can be obtained and then:

$$p_1 = p_0 + \Delta p; \eta_1 = \eta_0 + \Delta \eta$$

If $|\Delta p| < \varepsilon$, the convergence for the i-mode is reached and the procedure goes on for a new speed value. At first, for the i-mode calculation for a speed close to zero the assumptions are the following:

$$p_{or} = -\zeta_i \omega_{ni}$$

$$p_{oi} = \omega_{ni} \sqrt{(1 - \zeta_i^2)}$$

$$\omega_{ni} = \text{natural pulsation}$$

$$\zeta_i = \text{modal damping coefficient}$$

$$\eta_0 = \text{null vector, with the only } i \text{ unitary component}$$

For the second speed, the previous iteration values are taken, while for the next speeds all the p values are linearly extrapolated between the two immediately previous iterations. For η the value of the last iteration is assumed.

The computational speed of the PK-method is comparable to the K-method one.

4.4 Aerodynamic forces approximation

At each step of the solution methods, the aerodynamic matrix Q must be calculated, [41].

In general, Q matrices evaluation occurs for a limited range of reduced frequencies and, if required, they need to be interpolated.

The interpolation techniques are basically two:

- a) Linear splines;
- b) Rational approximations.

Roger [42] provides an excellent rational approximation:

$$Q(kr) = A_0 + (jkr)A_1 + (jkr)^2A_2 + \sum_{L=1}^4 B_L * \frac{(jkr)}{(jkr) + \gamma_L} \quad (22)$$

The values of γ_L depend on the reduced frequencies values for which Q matrices are known.

To speed up the convergence of the method, $A_0 = Q(0)$. The unknown real matrices: $A_1 A_2 B_1 B_2 B_3 B_4$ are evaluated by means of the least square method about the difference $Q(kr) - Q(0)$. It is simple to obtain the Q matrix corresponding with a proper reduced frequency value, if the coefficients matrices are known. The derived matrix $Q(kr)_{kr}$ can be also achieved through the expansion, and this is useful in the II PK method.

4.4.1 P method

By exploiting the Rogers approximation and by imposing:

$$q_0 = \frac{1}{2}\rho V^2 ; q_1 = \frac{1}{2}\rho V \underline{cr}; q_2 = \frac{1}{2}\rho \underline{cr}^2$$

The following expression can be obtained:

$$q_0 Q(kr)\eta = [q_0 A_0 + q_1 A_1(j\omega) + q_2 A_2(j\omega)^2] * \eta + q_0 \sum_{L=1}^4 B_L * \frac{(j\omega)*\eta}{(j\omega)+\gamma_L*\frac{v}{cr}} \quad (23)$$

By substituting it into the aeroelastic stability equation:

$$(j\omega)^2 [M - q_2 A_2] \eta + (j\omega) [\sigma - q_1 A_1] \eta + [K - q_0 A_0] \eta - q_0 \sum_{L=1}^4 B_L * \frac{(j\omega)*\eta}{(j\omega)+\gamma_L*\frac{v}{cr}} = 0 \quad (24)$$

Then, setting:

$$M_s = [M - q_2 A_2]; C_s = [\sigma - q_1 A_1]; K_s = [K - q_0 A_0]; \gamma_L = B_L * \frac{(j\omega) * \eta}{(j\omega) + \gamma_L * \frac{v}{cr}}; L=1.4$$

(24) becomes:

$$(j\omega)^2 M_s \eta + (j\omega) C_s \eta + K_s \eta - q_0 \sum_{l=1}^4 Y_l = 0 \quad (25)$$

$$\gamma_L * [(j\omega) + \gamma_L * \frac{v}{cr}] = B_L * (j\omega) * \eta; L=1.4$$

Then assuming:

$$(j\omega)^2 \eta = \ddot{\eta}; (j\omega) \eta = \dot{\eta}; (j\omega) Y_L = \dot{Y}_L$$

(25) can be written as follows:

$$M_s \ddot{\eta} + C_s \dot{\eta} + K_s \eta - q_0 \sum_{l=1}^4 Y_l = 0 \quad (26)$$

$$\dot{Y}_l + \left(\frac{\gamma_L v}{cr} \right) Y_l - B_L \dot{\eta} = 0; L=1.4$$

Adding the identity:

$$\dot{\eta} - \dot{\eta} = 0$$

It is possible to express constant coefficients differential equations system:

$$\dot{Z} = AZ \quad (27)$$

Where:

$$A = \begin{bmatrix} 0 & I & 0 & 0 & 0 & 0 \\ -M_s^{-1}K_s & -M_s^{-1}C_s & q_0M_s^{-1} & q_0M_s^{-1} & q_0M_s^{-1} & q_0M_s^{-1} \\ 0 & B_1 & -I\gamma_1v/cr & 0 & 0 & 0 \\ 0 & B_2 & 0 & -I\gamma_2v/cr & 0 & 0 \\ 0 & B_3 & 0 & 0 & -I\gamma_3v/cr & 0 \\ 0 & B_4 & 0 & 0 & 0 & -I\gamma_4v/cr \end{bmatrix}$$

$$Z = \begin{bmatrix} \eta \\ \dot{\eta} \\ Y_1 \\ Y_2 \\ Y_3 \\ Y_4 \end{bmatrix}$$

Compared to the first PK-method, the P-method is characterized by the lack of iterations on the generic mode; on the other hand, the problem dimensions increase from 2-order up to 6N-order. Moreover, this formulation is affordable with the modern techniques of systems control.

4.5 Harmonic Balance Method

The harmonic balance method investigates the oscillations of limit cycle of systems with lumped non-linearity by using frequency-domain techniques (Fourier-series).

The behavior of the linear systems with lumped non-linearity can be explained through the following block diagram in Fig. 26:

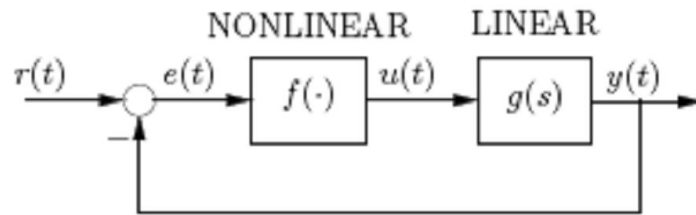


Fig. 26: Non-linearity in a linear system, [41]

Such a system can provide auto-oscillations with limited amplitude, defining periodical movements called limit cycles.

If the system is enabled to filter the high-frequency harmonics, as a first attempt, the amplitude and the frequency of the only first harmonic can characterize the whole limit cycle. This hypothesis is valid in flutter conditions.

If the system is described by the following equation:

$$\ddot{x} + f(x, \dot{x}) = 0 \quad (28)$$

Setting:

$$x = A\sin(\omega t) \quad (29)$$

From which:

$$\dot{x} = \omega A\cos(\omega t) \quad (30)$$

The function will be:

$$f(x, \dot{x}) = f(A\sin(\omega t), \omega A\cos(\omega t))$$

Approximating the function $f(x, \dot{x})$ by its first Fourier harmonic:

$$f(x, \dot{x}) = a_0 + a_1 \cos(\omega t) + b_1 \sin(\omega t)$$

Where:

$$a_0 = \frac{1}{T} \int_0^T f(t) dt$$

$$a_1 = \frac{2}{T} \int_0^T f(t) \cos(\omega t) dt$$

$$a_2 = \frac{2}{T} \int_0^T f(t) \sin(\omega t) dt$$

From the (29) and (30) the following expressions can be obtained:

$$\sin(\omega t) = \frac{x}{A}$$

$$\cos(\omega t) = \frac{\dot{x}}{\omega A}$$

Inserting them into (28), it becomes:

$$\ddot{x} + \left(\frac{a_1}{A\omega}\right)\dot{x} + \left(\frac{b_1}{A}\right)x = 0 \quad (31)$$

(31) is the representation of the linearized equation of the system: the non-linearity is contained into the (hysteretic) damping term $\frac{a_1}{A\omega}$ and in the stiffness term $\left(\frac{b_1}{A}\right)$. Both of them depend on the oscillation amplitude, in case of resonance.

If the non-linear function is odd, the damping term is zero, being:

$$a_1 = \frac{2}{T} \int_0^T f(t) \cos(\omega t) dt = 0$$

The Eq. 31 can also be expressed as:

$$\ddot{x} + K_{eq}x = 0 \quad (32)$$

Where the multiplying coefficient K_{eq} is the equivalent stiffness. According with the Optimal Linearization Blaquiére Method, K_{eq} must minimize the mean square deviation between the non-linear function f and its approximation $K_{eq}x$.

The error is equal to:

$$\varepsilon(K_{eq}, t) = f(x, \dot{x}) - K_{eq}x \quad (33)$$

While the mean square deviation is:

$$E(K_{eq}, t) = \varepsilon^2 = f^2(x, \dot{x}) - 2K_{eq}xf(x, \dot{x}) + K_{eq}^2x^2 \quad (34)$$

The mean square deviation minimization in the period T is given by the following expression:

$$\frac{1}{T} \int_0^T \frac{\partial E(K_{eq}, t)}{\partial K_{eq}} dt = 0 \quad (35)$$

Where:

$$\frac{\partial E(K_{eq}, t)}{\partial K_{eq}} = -2xf(x, \dot{x}) + 2K_{eq}x^2 \quad (36)$$

Substituting (36) in (35), the latter becomes:

$$-\frac{2}{T} \int_0^T xf(x, \dot{x}) dt + \frac{2}{T} K_{eq} \int_0^T x^2 dt = 0 \quad (37)$$

(37) provides the expression of the equivalent stiffness, K_{eq} :

$$K_{eq} = \frac{\int_0^T xf(x, \dot{x}) dt}{\int_0^T x^2 dt} \quad (38)$$

5 Aeroelasticity of morphing devices

This chapter addresses the aeroelastic stability investigation performed on the reference aircraft (TP90) equipped with morphing flaps and winglets. Rational approaches were implemented in order to simulate the effects induced by variations of such movable surfaces actuators stiffness on the aeroelastic behavior of the A/C also in correspondence of several failure cases.

More in detail, rational analyses were implemented by considering:

- ✓ The impact of morphing systems kinematics, masses and distributed stiffness of the **adaptive flaps** and **winglets** at aircraft level;
- ✓ The adoption of massbalancing to guarantee flutter clearance;
- ✓ The uncertainties in the structural dynamics due to actuator free-play nonlinearity.

Moreover, aircraft stability robustness with respect to morphing systems integration was evaluated through a combination of “worst cases” simulating the mutual interaction among the adaptive systems. The “worst case” indicates that, in addition to the case that the aircraft is aeroelastically safe with the nominal model according with the CS-25 requirements [2], it should also be safe with a combination of morphing wing devices.

For that purpose, sensitivity studies were carried out on the base of fast aeroelastic approaches involving simplified and reliable structural and aerodynamic models. Outcomes of trade-off studies provided useful guidelines to judge the adequacy of the morphing surfaces structural configuration in the framework of their potential impact on flutter instability.

5.1 Dynamic Model

5.1.1 Structural Model

In order to perform fast sensitivity analyses [3] – [31], a representative structural model of the whole aircraft² was generated referring to a stick-equivalent formulation to catch the entire system dynamics. For that purpose, rational criteria were adopted in terms of the dynamic structural condensation; then, well-

² The need of a full aircraft model is connected to the investigation of the aeroelastic effects induced by asymmetrical failures, as reported in Section 6.

consolidated approaches were used to reduce distributed aircraft inertial properties into an equivalent set of lumped masses.

More in detail, the stiffness and inertial properties were extracted by two preliminary FE models respectively elaborated by the University of Naples (Fig. 27) and by the Italian Aerospace Research Centre (CIRA) (Fig. 28).

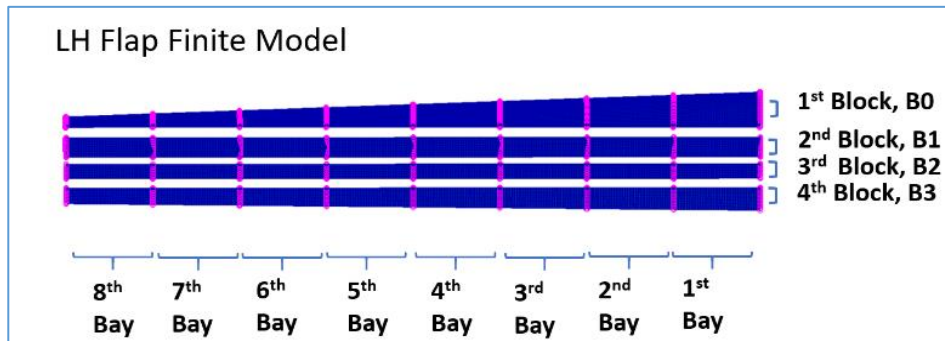


Fig. 27: LH morphing flap preliminary Finite Element Model developed by UniNa, [31]

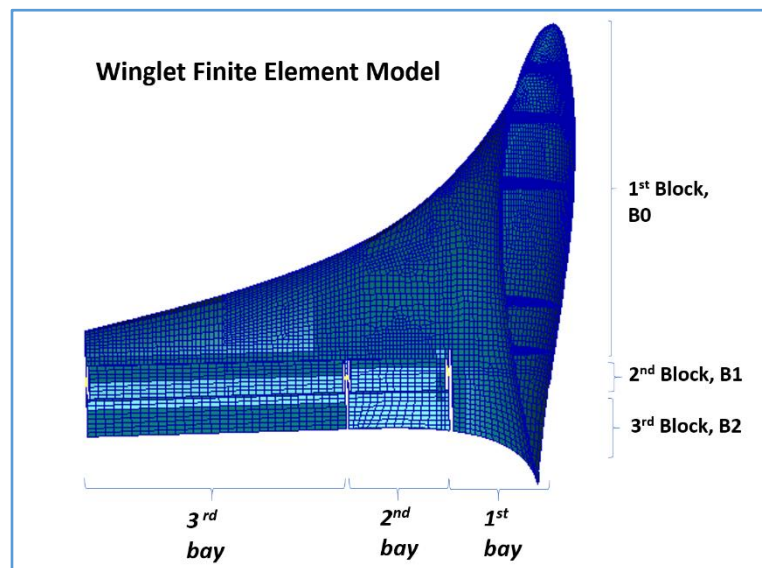


Fig. 28: LH morphing winglet preliminary Finite Element Model developed by CIRA, [31]

From now on, the term “block” will address the structure sub-assy made up by the rib homolog blocks and the spars linking them in a closed box.

All the properties were condensed in a discrete number of structural grids, which position was driven by the intersection among each hinge/elastic axis and morphing rib, [31].

More in detail, the elastic axis evaluation of the wing and of the first block of both morphing flap and winglet was carried out by means of an iterative procedure, described as follows:

1. A trial position of the elastic axis was assumed;
2. Nodes were added to the structural model in correspondence of the intersection points between the elastic axis (point 1) and ribs' planes;
3. At each rib, available RBE2 elements had to slave the nodes of the rib boundary to the node at the intersection between the rib plane and the (imposed) elastic axis;
4. An arbitrary torque M_T , was applied along the elastic axis and in correspondence of its intersection with the plane of the rib located at wing tip. The master node on the rib plane at the wing root was constrained in all the degrees of freedom;
5. Static analysis was performed in MSC-NASTRAN® environment and the following displacements were evaluated ([44]):
 - TY_i : displacement of the master node on the i -th rib along the axis Y perpendicular to the elastic axis and to the wing box middle plane (vertical bending displacement induced by M_T);
 - RX_i : rotation of the master node on the i -th rib around the axis X coincident with elastic axis (torsion induced by M_T);
6. Ratios $l_i = |TY_i/RX_i|$ were evaluated at each rib location thus providing the offset of the actual shear centre with respect to its supposed position.
7. At each rib location, the master node defined at point 3 was shifted chordwise by the amount l_i ;
8. Steps from 4 to 7 were repeated until all ratios l_i resulted quite equal to zero, Fig. 29.

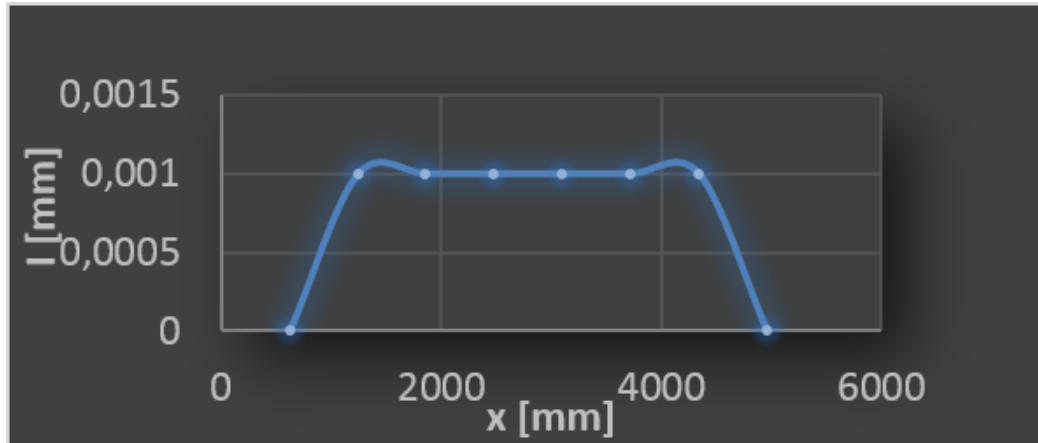


Fig. 29: Elastic axis convergence parameter, [31]

Stiffness distributions along the span of the blocks of both the morphing devices (Fig. 27 and Fig. 28), to be applied to the equivalent beam, were determined by constraining the first node of the (assessed) elastic/hinge axis and by imposing a known load value at the tip (last node of the elastic/hinge axis), [3].

Then:

- A Torque M_x , about the elastic/hinge axis, yielded rotations of master nodes around x-axis (=elastic/hinge axis). The derivative of these rotations with respect to x coordinate was evaluated and the torsional stiffness was obtained according to the following equation:

$$GJ(x) = M_x \left(\frac{dR_x(x)}{dx} \right)^{-1}$$

- A Bending moment, about y (and z) axis, yielded rotations of master nodes around y (and z)-axis. The derivative of these rotations with respect to y (and z) coordinate was evaluated and the bending stiffness was obtained according to the following equations:

$$EI_{\min}(x) = M_y \left(\frac{dR_y(x)}{dx} \right)^{-1}$$

$$EI_{\max}(x) = M_z \left(\frac{dR_z(x)}{dx} \right)^{-1}$$

- A Normal force, aligned to the elastic axis, produced displacements of master nodes along x-axis (=elastic/hinge axis). The derivative of these displacements with respect to x coordinate was evaluated and the axial stiffness was obtained according to the following equation:

$$EA(x) = N_x \left(\frac{dT_x(x)}{dx} \right)^{-1}$$

The logical flow for the stiffness distributions evaluation is depicted in Fig. 30:

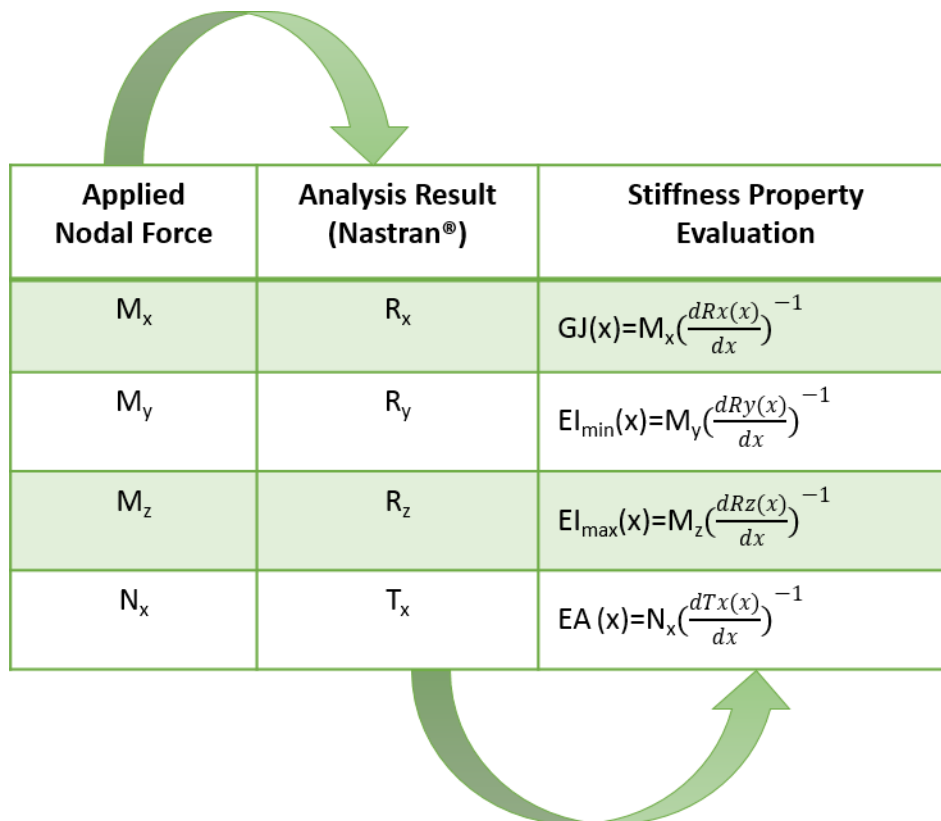


Fig. 30: Logical Flow for the stiffness properties evaluation

Where:

- x is the generic coordinate along the X-axis (Fig. 31);
- $GJ(x)$ is the torsional stiffness distribution (Fig. 32, Fig. 33, a))
- $EI_{\min}(x)$ is the vertical bending stiffness distribution (stiffness to bending across XY plane, Fig. 32, Fig. 33, b));

- $EI_{max}(x)$ is the lateral (fore & aft) bending stiffness distribution (stiffness to bending across XZ plane, Fig. 32, Fig. 33, c));
- $EA(x)$ is the distribution of the stiffness exhibited with respect to forces acting along the elastic axis (normal-to-sections solicitations), Fig. 32, Fig. 33, d));
- M_x and $R_x(x)$ are respectively an arbitrary torque moment acting around the elastic axis (X-axis) at its free-end and $R_x(x)$ is the rotation around the X-axis of the cross section at span-wise location x ;
- M_z and $R_z(x)$ are respectively an arbitrary bending moment acting around Z-axis at elastic axis free-end and $R_z(x)$ is the rotation around the Z-axis of the cross section at span-wise location x ;
- N_x and $T_x(x)$ are respectively an arbitrary force acting along elastic axis (X-axis) at its free-end and $T_x(x)$ is the displacement along the X-axis of the cross section at span-wise location x .

The stiffness properties were obtained using a polynomial interpolation limited to the first or second order. Fig. 32 and Fig. 33 show all the stiffness properties obtained for the morphing flap and winglet.

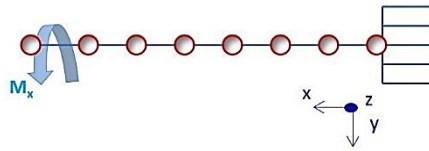
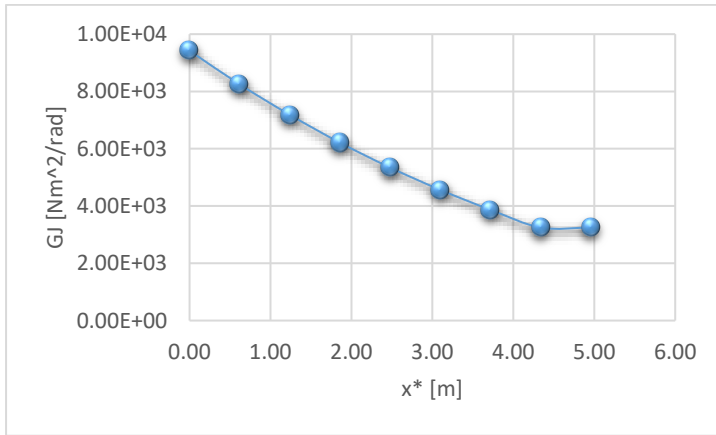
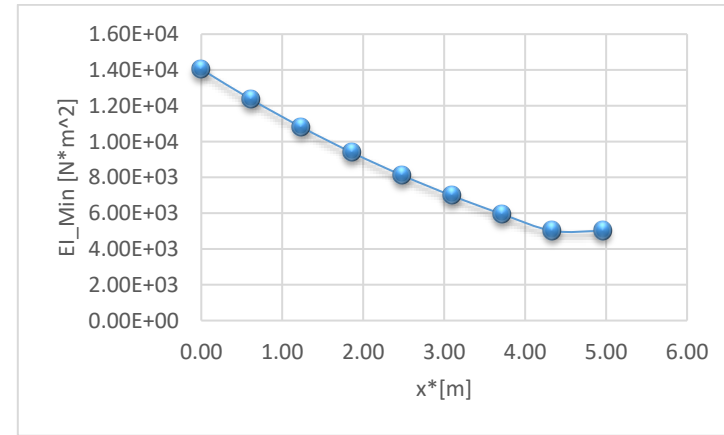


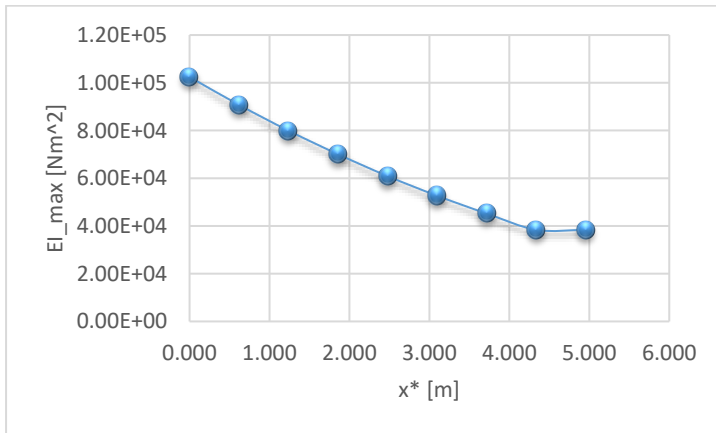
Fig. 31: Example of load case applied for GJ evaluation, [31]



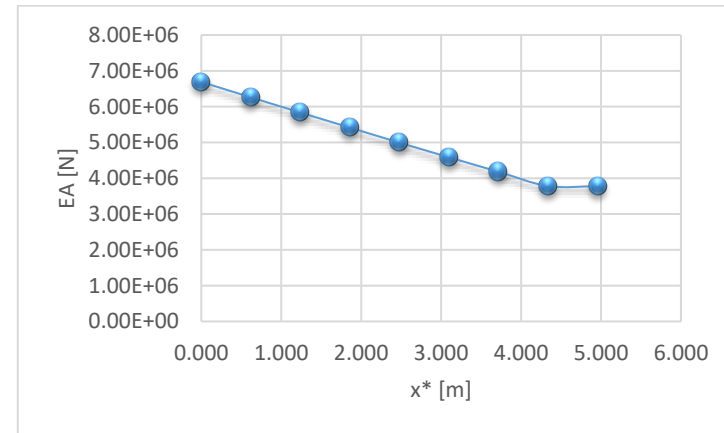
(a) GJ Evaluation, morphing flap



(b) EI min evaluation, LH morphing flap

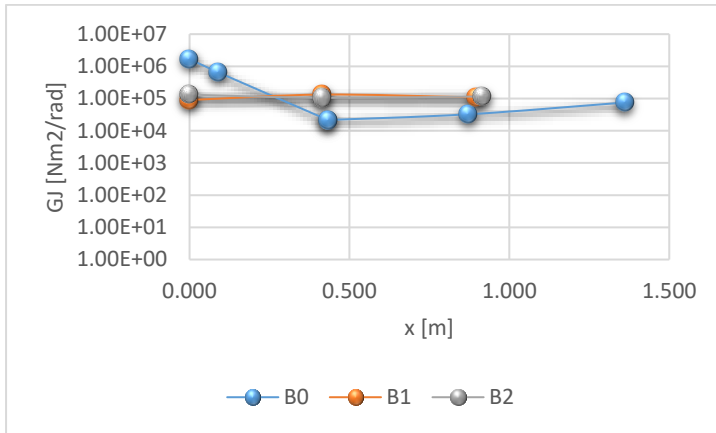


(c) EI max Evaluation, morphing flap

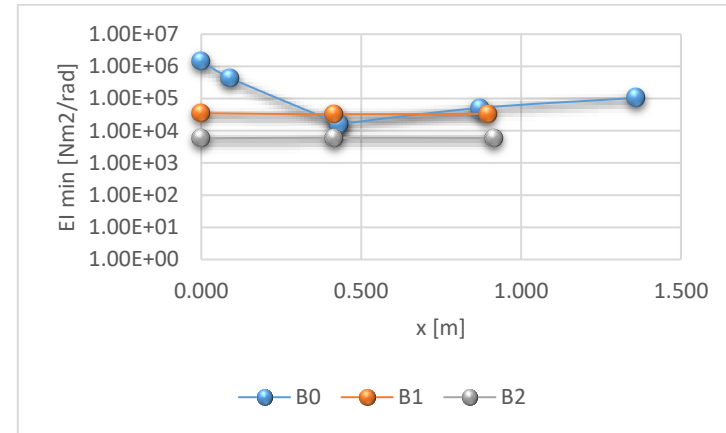


(d) EA Evaluation, morphing flap

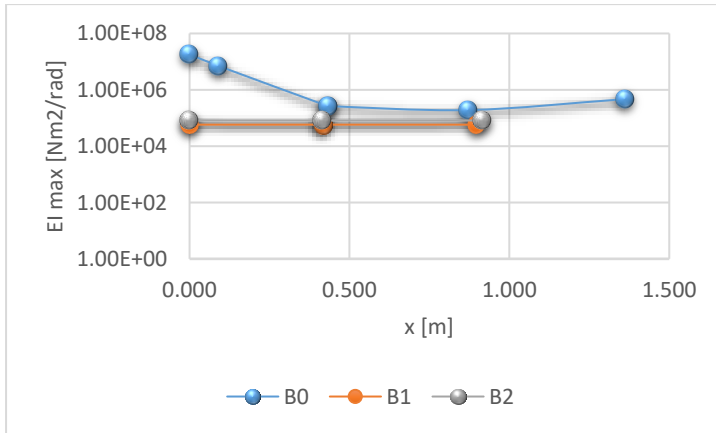
Fig. 32: Flap tabs stiffness properties



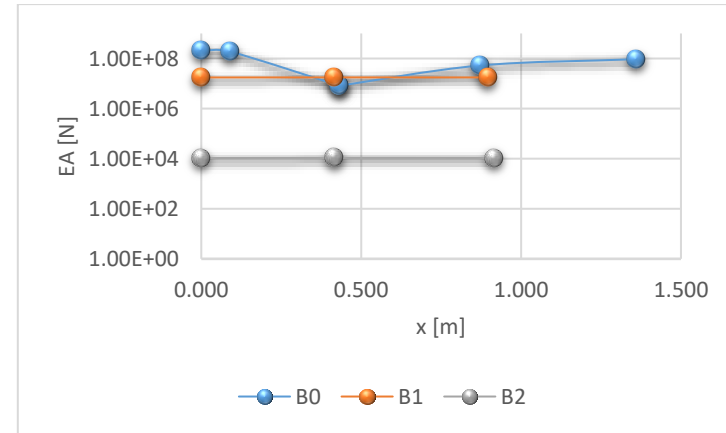
(a) GJ Evaluation, morphing winglet



(b) EI min evaluation, LH morphing winglet



(c) EI max Evaluation, morphing winglet



(d) EA Evaluation, morphing winglet

Fig. 33: Winglet tabs stiffness properties

For the flaps, the B3 tabs hinge lines were linked to the elastic axis of the wing by means of stiff beam elements; pin flags were properly imposed at the end-nodes of such elements to release the rotation around the hinge lines. It is fundamental to underline that only the B3 tabs were considered, since they are involved during high-speed performance and impact the aeroelastic behavior of the A/C.

For the winglets, the stiff beam elements with pin flags were introduced among B3-B2, B2-B1, and B1-B0 respective hinge/elastic axes.

Flap and winglet tabs actuators were modelled by means of grounded spring elements linked to the end grid of each movable surface. Moreover, direct input matrices condensed at grids (DMIG, [44]) were introduced to properly reproduce stiffness and inertial characteristics of each jointing region of the aircraft (namely, wing-fuselage, fuselage-tails and wing-winglet interface).

Auxiliary (not structural) grids were used to assure high quality interpolation of modal displacements along the aerodynamic lattice; auxiliary grids were linked to structural grids by means of RBE elements.

5.1.2 Inertial Model

Mass properties of the movable surfaces of the flaps tabs and winglets were evaluated by considering a system of lumped masses obtained by the weight of the intersection zone between each bay (the portion of the flap and of the winglet located between two consecutive ribs, Fig. 27 and Fig. 28) and the tabs' blocks. Such masses were located at the gravity center of each item, and then rigidly connected to the closest grid of the beam-equivalent model of the pertaining item. This is possible thanks to the hypothesis of considering all the lifting surfaces chordwise deformations negligible with respect to the spanwise ones. In this way, the inertial effect of each trunk can be represented through a node located at the gravity center, with its weight and barycentric inertial moments.

The leading edge and not movable trailing edge portions aeroelastic impact on the wing was only considered from the inertial standpoint, while their effect in terms of stiffness was hypothesized negligible.

The complete dynamic model is depicted in Fig. 34.

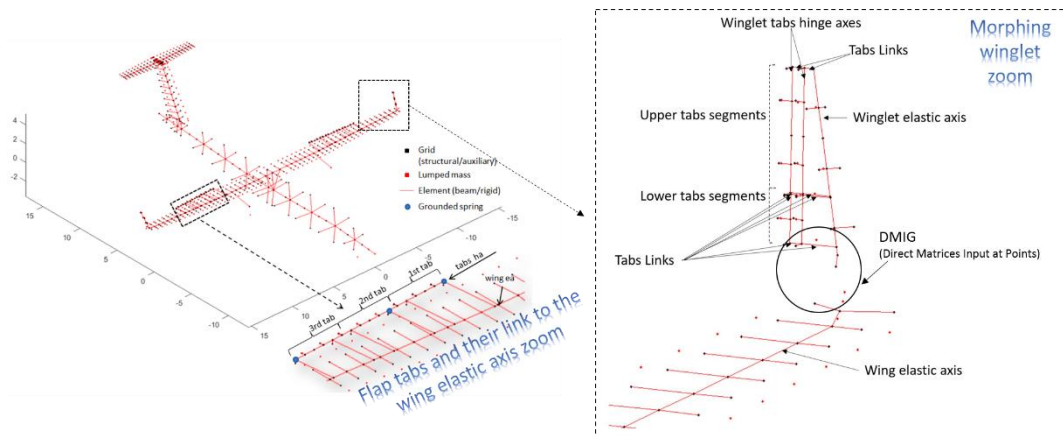


Fig. 34: TP90 Dynamic model in Sandy environment (ref. axes in meters), [31]

5.2 Aerodynamic and Interpolation Model

The aerodynamic schematization is based on the Doublet Lattice Method (DLM), allowing for the calculation of the matrices of unsteady aerodynamic influence coefficients (AIC).

The aircraft is divided in a proper number of panels; each of them is divided into strips, and subpanels called “box” compose each strip.

A higher boxes density was considered for the movable trailing edge and -to assure mesh uniformity- for the not-movable trailing edge.

The aerodynamic model is depicted in Fig. 35.

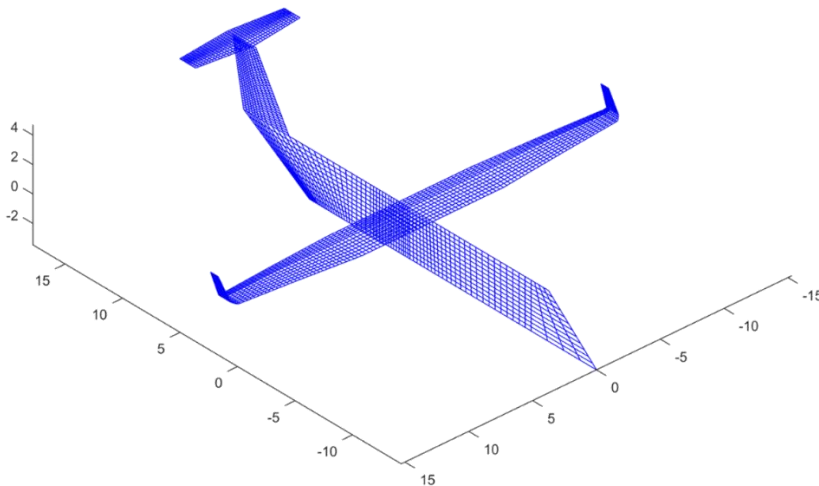


Fig. 35: TP90 aerodynamic model in Sandy environment (ref. axes in meters), [31]

Modal displacements at the center of each aerodynamic box were obtained by means of superficial spline functions attached to auxiliary (not structural) grids, used to assure high quality interpolation of modal displacements along the aerodynamic lattice. Auxiliary grids were linked to structural grids by means of RBE elements.

A representation of the aerostructural model is shown in Fig. 36.

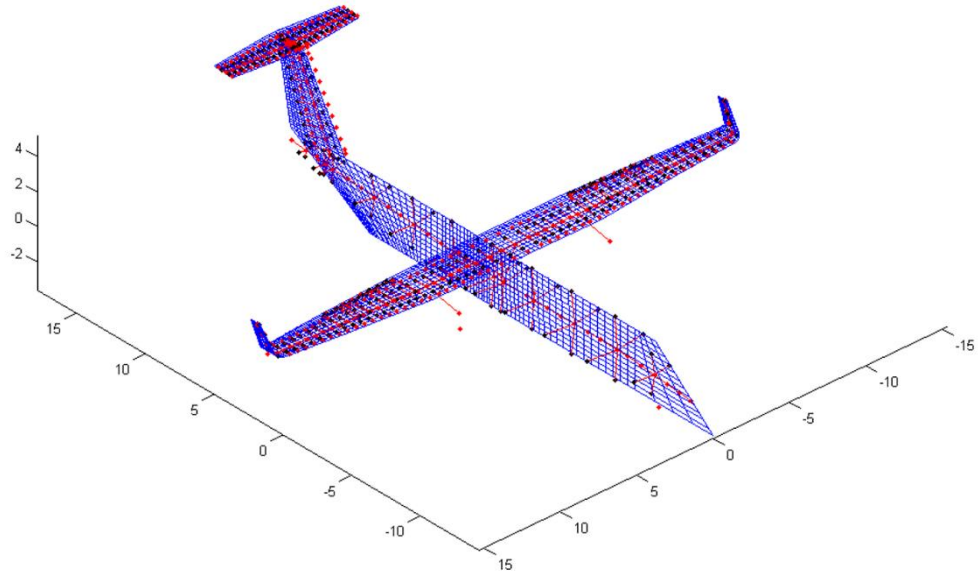


Fig. 36: TP90 Aeroelastic model in Sandy Environment (ref. axes in meters), [31]

5.3 Flutter Analyses

The overlap between structural and aerodynamic models provided the aerostructural scheme to study the A/C aeroelastic behavior. Several cases of flutter analyses, by means of Sandy© code, were investigated in order to meet the safety requirements imposed by the applicable aviation regulations, [2]:

- System fully operative;
- System in the failure condition

5.3.1 Trade-off flutter analysis on flap tabs

5.3.1.1 Carpet plot Generation

Flutter analyses on flap tabs were carried out under the following assumptions:

- PK-continuation method with rationalization of generalized aerodynamic forces for the evaluation of modal frequencies and damping trends versus flight speed;
- Theoretical elastic modes association in the frequency range 0Hz-50Hz (elastic modes being pertinent to free-free aircraft, with only plunge and roll motions allowed);
- Modal damping (conservatively) equal to 0.015 for all the elastic modes;
- Sea-level altitude, flight speed range 0-200 m/s ($1.25 V_D$, V_D (dive speed) = 200.00 m/s, [2]);
- All ailerons control surfaces locked;
- Winglets tabs locked.
- Flutter speeds were evaluated corresponding with different settings for the movable flap, each setting being defined by means of two (trade-off) parameters:
 1. Inertial distribution (to cover possible deviations from preliminary design figures);
 2. Actuation line stiffness distribution.

Investigated cases mapped three different inertial distributions in combination with fifteen different stiffness distributions of the actuation line moving the flap tabs; the trade-off domain was therefore composed by forty-five different configurations of the flap tabs, Fig. 37.

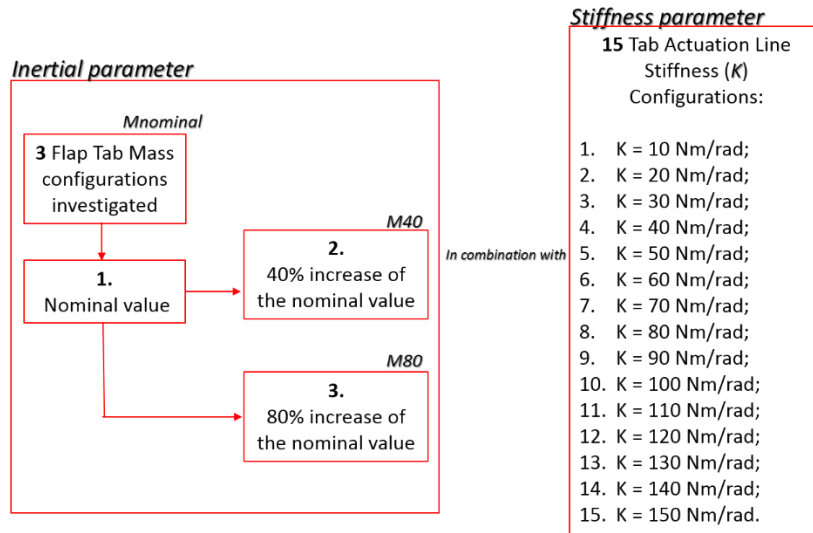


Fig. 37: Trade-off analyses parameters on flap tabs

The condition $k=0$ Nm/rad was then taken into account to simulate the failure (free rigid oscillation) of the tabs; the highest value was defined on the basis of practical considerations regarding the probability of coalescence of tabs harmonics with wings modes in the flight speed range $[0; 1.25] V_D$.

A stability carpet plot was generated to provide a thorough overview of flutter speed trends versus stiffness of flaps tabs actuation line (Fig. 38).

From this moment on, “K” will denote the actuation line stiffness.

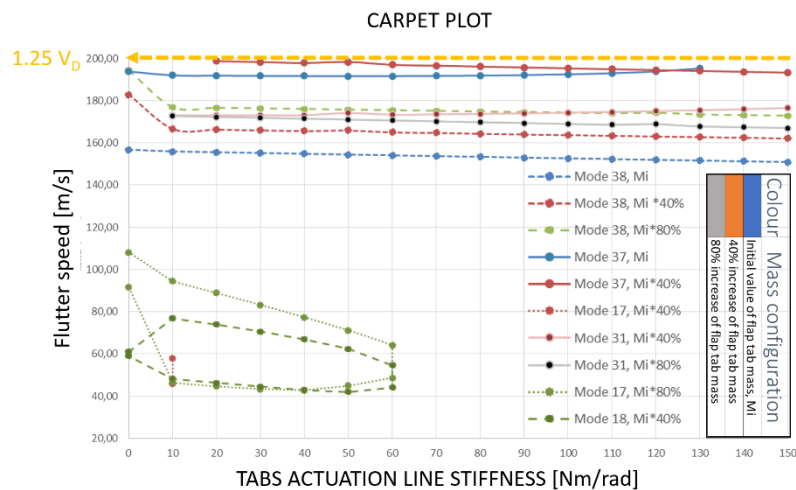


Fig. 38: First trade-off Carpet Plot

Each curve of the carpet plot is the representation of a specific flutter mode, colored according with the inertial configuration it refers to.

The yellow dotted line defines the safe domain for flutter speed according to CS-25, paragraph 629: if a flutter mode occurs at a speed greater than $1.25V_D$ (V_D =dive speed), it is aeroelastically safe.

Among the 34 modes investigated, only five appear in the carpet plot since the remaining one's exhibit flutter speed greater than 200 m/s.

All modes corresponding to each mass configuration are present for each tab actuation line stiffness value, except the modes number 17, 18, not present for $K > 60$ Nm/rad.

The most critical flutter modes – judged in such way because of their independence from the K values - resulted:

- *Mode 31*: symmetric wing tip/winglet bending (Fig. 39);
- *Mode 37*: symmetric outer wing torsion (Fig. 40);
- *Mode 38*: anti-symmetric outer wing torsion (Fig. 41).

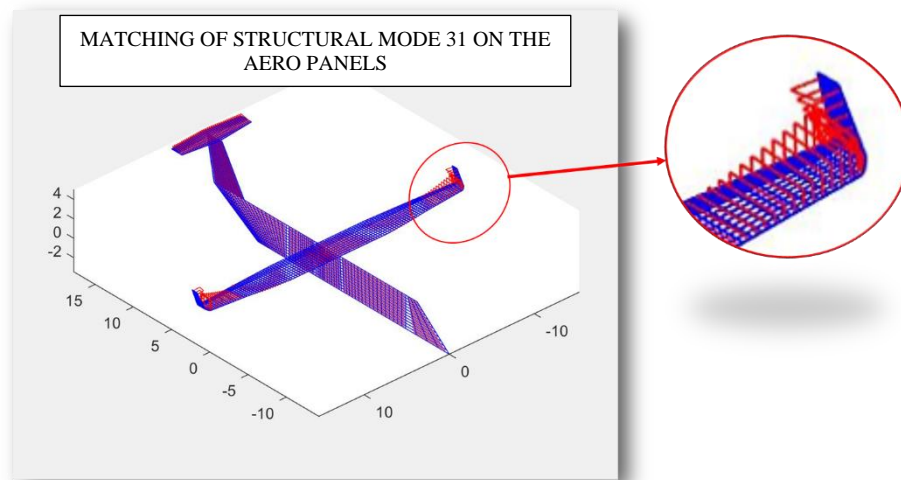


Fig. 39: Flutter mode 31 - Symmetric wing tip/winglet bending

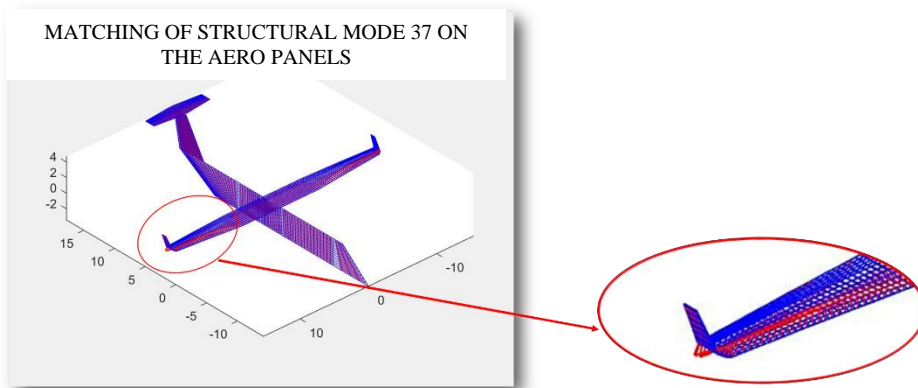


Fig. 40: Flutter Mode 37 - Symmetric outer wing torsion

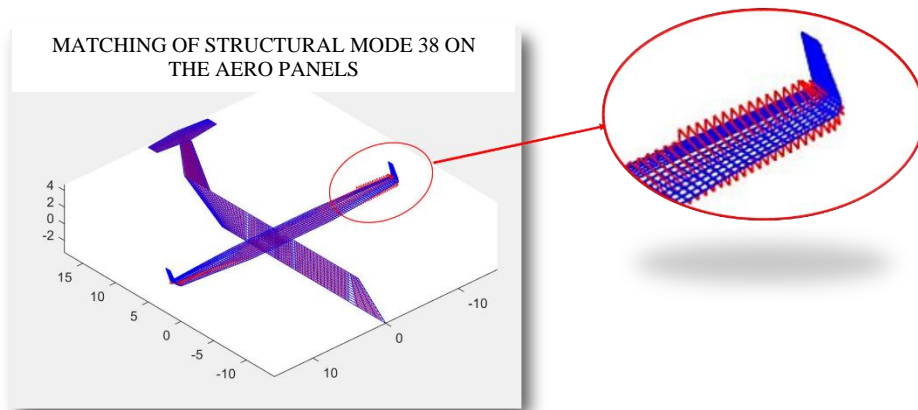


Fig. 41: Flutter Mode 38 - Anti-symmetric outer wing torsion

By zooming in the outer flap tabs region, a typical underbalanced and unstable motion of the flap tabs appears evident.

5.3.1.2 Flutter dynamics investigation

Accurate analysis of modal cross participation factors into flutter modes was performed in order to isolate the principal modes involved in detected flutter.

More in detail, the investigation protocol followed during this stage is set out below:

1. Flutter speed was calculated by considering all modes as participating;

2. Most critical flutter modes were identified (namely, 31, 37 and 38);
3. Participation factors were evaluated with respect to each most severe flutter mode described at point 2;
4. Flutter speed was furthermore evaluated by considering the only modes with the highest participation factors (point 3) at the flutter speed of the point 1.
5. New flutter analyses were performed excluding one by one the modes of point 4, until the flutter speed of point 1 was almost reached (**isolated flutter condition**).

Participation factors of the modes 31, 37 and 38 are depicted in Fig. 42, Fig. 43, Fig. 44.

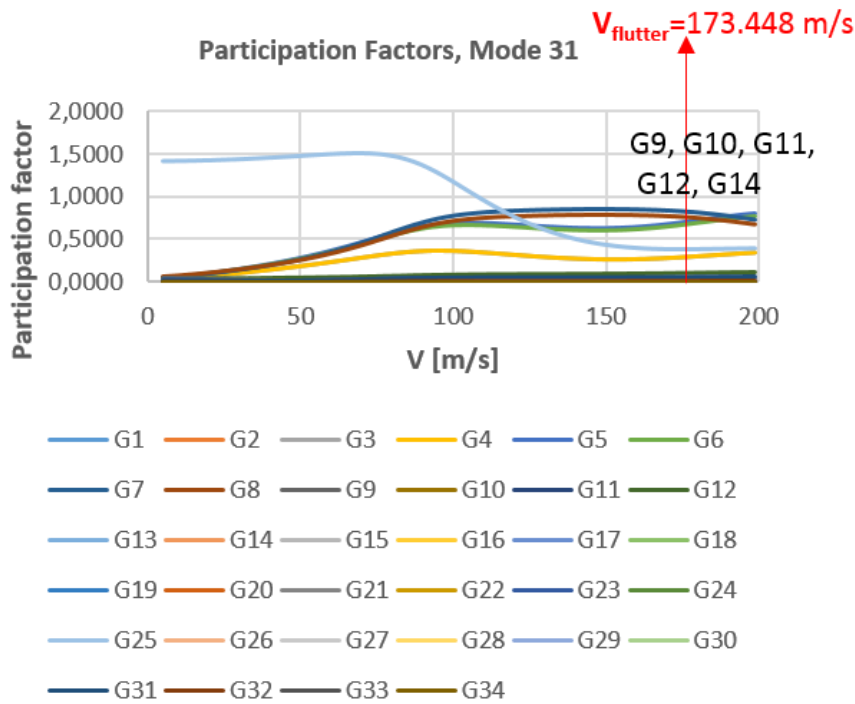


Fig. 42: Participation Factors, Mode 31 [31]

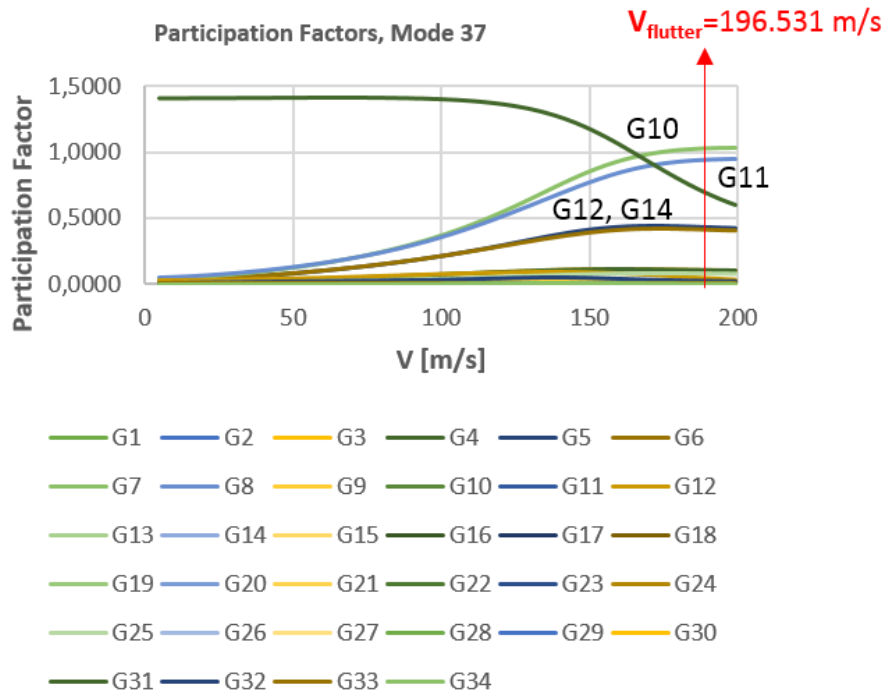


Fig. 43: Participation factors, Mode 37, [31]

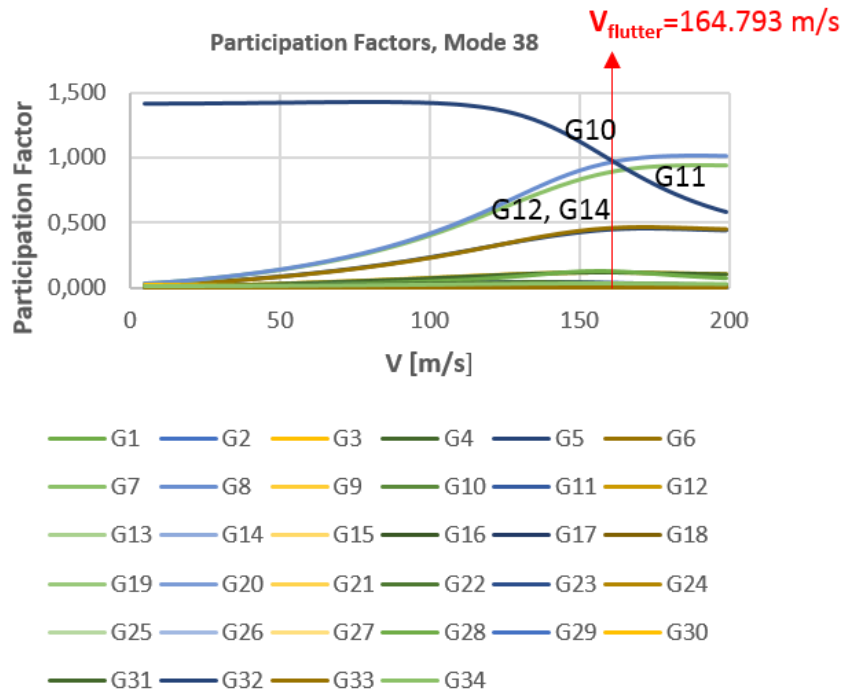


Fig. 44: Participation factors, Mode 38, [31]

Main results of the flutter dynamic investigation are shown in Fig. 45.

Minimum modal association		
Flutter mode	Associated Modes	
38	10, 11, 12, 14	
37	10, 11, 12, 14	
31	9, 10, 11, 12, 14	

↓

Mode	Flutter condition, all modes, K=70 Nm/rad; M40	Flutter condition, associated modes only, K=70 Nm/rad; M40
38	$V_{flutter} = 164.793 \text{ m/s}$ $f = 31.557 \text{ Hz}$	$V_{flutter} = 216.56 \text{ m/s}$ $f = 30.470 \text{ Hz}$
37	$V_{flutter} = 196.531 \text{ m/s}$ $f = 31.106 \text{ Hz}$	$V_{flutter} = 245.58 \text{ m/s}$ $f = 30.12 \text{ Hz}$
31	$V_{flutter} = 173.448 \text{ m/s}$ $f = 22.809 \text{ Hz}$	$V_{flutter} = 180.86 \text{ m/s}$ $f = 22.67 \text{ Hz}$

Fig. 45: Minimum modal flutter association

By analysing the minimum flutter association of the most critical flutter modes, it can be concluded that the instabilities of M31, M37 and M38 are essentially due to the flap tabs underbalancing which in turns leads to a critical coupling with the external tabs harmonics (M13 and M14), while the inner tabs harmonics just act as flutter supporting modes.

This first result totally justifies the almost independence of such instabilities from tabs actuation line stiffness, K (as already observed), while a significant effect due to tabs inertial distribution is present.

5.3.1.3 Massbalancing of flap tabs

The definition of massbalancing can be given by indicating with:

- M_i the generic mass of the mobile surface;
- D_i the distance of M_i with respect to the hinge axis (positive if located behind the axis);
- M_b the massbalancing;

- D_b the distance of M_b with respect to the hinge axis.

Under the hypothesis of absence of friction effects, *100% Degree of Balancing* (DoB, in what follows) is the condition according to which the mobile surface returns in its original horizontal position, after a small angle deviation.

This is possible only if the hinge axis static moment is zero:

$$\sum_{i=1}^n M_i D_i - M_b D_b = 0$$

By imposing the distance D_b , the massbalancing M_b can be obtained:

$$M_b = \frac{\sum_{i=1}^n M_i D_i}{D_b} \quad (39)$$

This value, for definition, is associated with 100% Degree of Balancing.

It is obviously possible to calculate massbalancing values corresponding with other DoB, DoB^* , by multiplying $M_b * DoB^*$.

In this specific case of study, Table 3 shows massbalancing values obtained for the flap tabs by using (39).

	M_i [kg]	D_i [m]	S_i [Kg*m]	S_{tot} [Kg*m]	D_b [m]	M_b100 % [Kg]
1st Flap Tab	0.83975	0.09956	0.08361	0.20451	0.10000	2.04422
	0.81678	0.09955	0.08131			
	0.39775	0.09955	0.03959			
2nd Flap Tab	0.39775	0.10004	0.03979	0.22545	0.10000	2.25348
	0.76343	0.10004	0.07668			
	0.73887	0.09996	0.07362			
	0.35216	0.10042	0.03536			
3rd Flap Tab	0.35216	0.09992	0.03519	0.17056	0.10000	1.70487
	0.67884	0.09991	0.06782			
	0.67884	0.09951	0.06755			

Table 3: Massbalancing values of morphing flap tabs

The mathematical formulation of the massbalancing into the aeroelastic stability equation is described in [41].

Trade-off analyses were then performed by considering the massbalancing as a function of a decreasing degree of balancing, varying it from 100% up to the minimum value needed to ensure the absence of any flutter instability within the safety envelope.

Under the assumption of $K=150$ Nm/rad as fixed value in combination with each of the three inertial configuration -as already described in §5.3.1- of the tabs mass, the minimum flutter speeds have been plotted in Fig. 46 as functions of the Degree of Balancing.

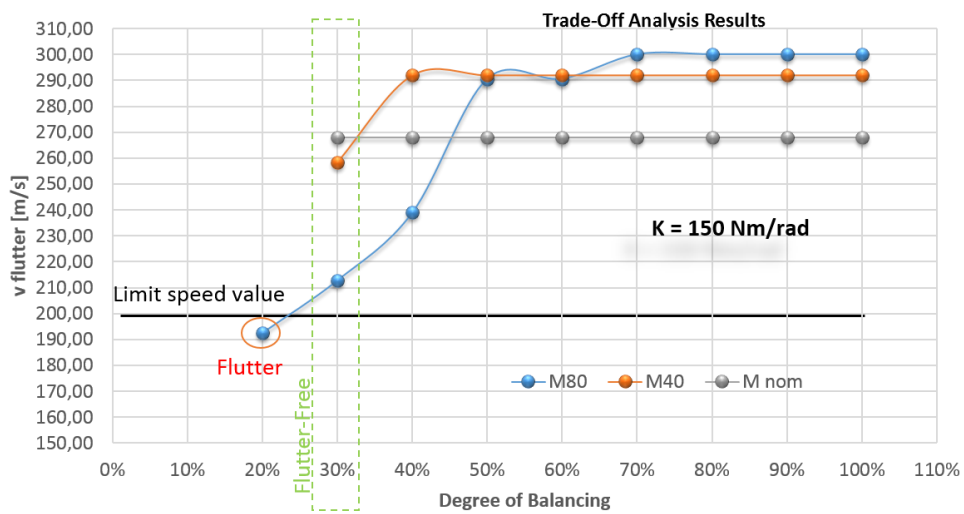


Fig. 46: Minimum flutter speed as function of flap tabs degree of balancing, for a fixed value of tabs actuation line stiffness

Fig. 46 shows that the minimum degree of balancing ensuring flutter clearance over the limit imposed by the CS-25 requirements (black horizontal line) is equal to 30%, for the fixed value of $K=150$ Nm/rad.

To understand the potential adequacy of the DoB value found equal to 30% even for the other values of tabs actuation line stiffness, a new sensitivity was performed in an inverse manner with respect to the previous one. In this case, the degree of balancing value was fixed, while the stiffness was considered variable into the range $[0; 200]$ Nm/rad. The results are depicted in Fig. 47.

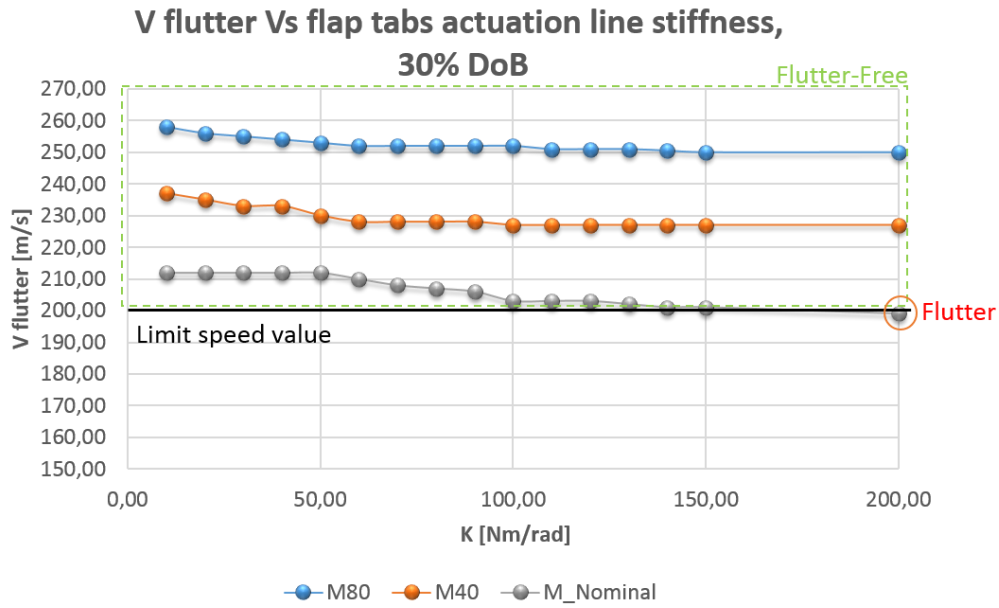


Fig. 47: Minimum flutter speed as function of flap tabs actuation line stiffness, 30 % Degree of Balancing

Fig. 47 shows a flutter within the speed certification envelope at $K=200$ Nm/rad, for 30% DoB. This led to extend the range of variability of K values up to 500 Nm/rad, by repeating the trade-off and increasing DoB to 40%.

Fig. 48 shows the results.

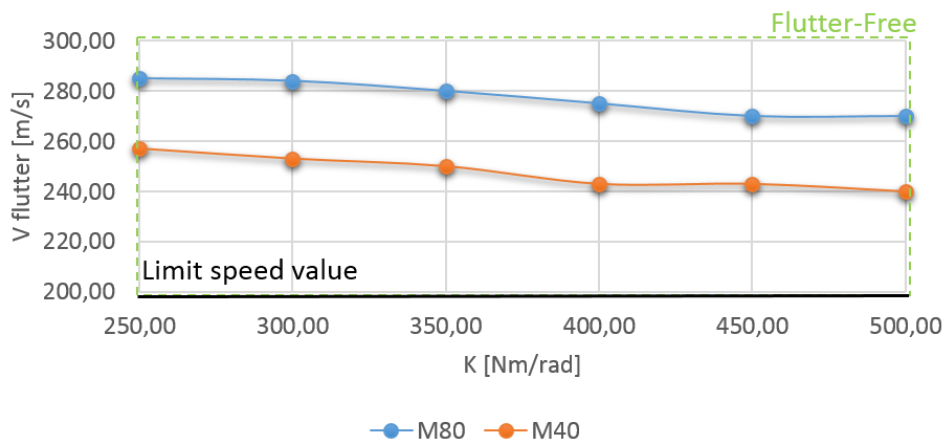


Fig. 48: Flutter speed as function of tabs actuation line stiffness, 40% Degree of Balancing

A comparison between the results of Fig. 47 and Fig. 48 is summarized below in terms of minimum Degree of Balancing ensuring flutter clearance:

- $K < 200 \text{ Nm/rad} \rightarrow 30\% \text{ Degree of Balancing}$;
- $K \geq 200 \text{ Nm/rad to } K \leq 500 \text{ Nm/rad} \rightarrow 40\% \text{ Degree of Balancing}$.

This difference affects the weight, as described in Table 4:

Flap Nominal Mass [Kg]	56.74
M_{bal} DoB 30% [Kg]	5.81
M_{nom} 30% DoB	62.55
M_{bal} DoB 40% [Kg]	7.75
M_{nom} 40% DoB	64.49

Table 4: Massbalancing solutions: impact on winglet weight

Two values of degree of balancing were identified for flap tabs as design solution to avoid flutter; aiming to minimize the flap weight, the design solution involving 30% of DoB was judged as the best one to assure the aeroelastic safety of the morphing flap.

5.3.2 Trade-off flutter analysis on winglet tabs combined with flap tabs

5.3.2.1 Carpet plot Generation

To study the aeroelastic impact of the morphing winglets tabs at aircraft level in combination with flaps tabs, a further aeroelastic stability assessment was carried out under the following assumptions:

- PK-continuation method with GAF rationalization was adopted for the evaluation of modal frequencies and damping trends as a function of the flight speed (V-g plots);
- Frequency range for the theoretical modes association: [0; 30] Hz;
- Modal damping: 0.015 for all the elastic modes;
- Sea-level altitude;
- Flight speed: [0; 1.25 V_D], where V_D is the dive speed of the TP90 aircraft, equal to 160 m/s.
- All ailerons control surfaces locked;

- Flap tabs unlocked;
- Flap tabs in the worst combined conditions of inertial distribution (M80) and actuation line stiffness ($K=150$ Nm/rad).

Flutter speeds were evaluated for different inertial configurations of the movable surfaces of the winglets.

Trade-off parameters were considered in combination with each other:

- Inertial distribution:
- Nominal mass, $Mw_nominal$;
- 30% mass increase, $Mnominal*1.3$ (Mw_30);
- Stiffness distribution

For each inertial distribution, a wide variation range was considered for winglet actuation line stiffness: $[0; 1500]$ Nm/rad. Obtained results are depicted in Fig. 49.

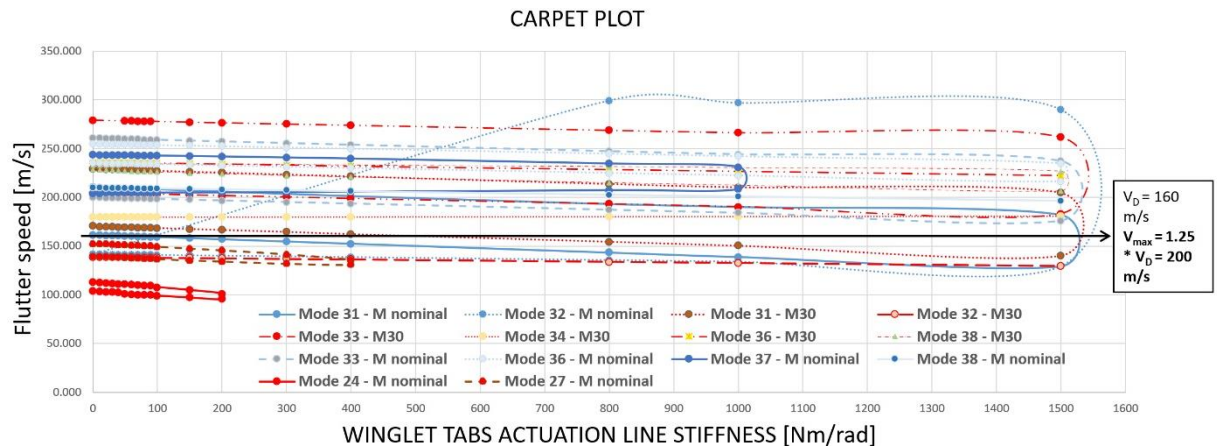


Fig. 49: Trade-off analysis on winglet tabs combined with flap tabs in locked commands, carpet plot [31]

The main points of the carpet plot shown in Fig. 49 are listed below:

- The flutters of Mode 24 and 27 respectively disappear for $K > 200$ and $K > 400$ Nm/rad.
- The most critical modes belonging to both inertial configurations and for each K value are:
 1. *Mode 31*: anti-symmetric wing tip torsion/winglet bending (Fig. 50);
 2. *Mode 32*: symmetric outer wing torsion/winglet bending (Fig. 51);

3. *Mode 33: anti-symmetric outer wing torsion/winglet bending* (Fig. 52).

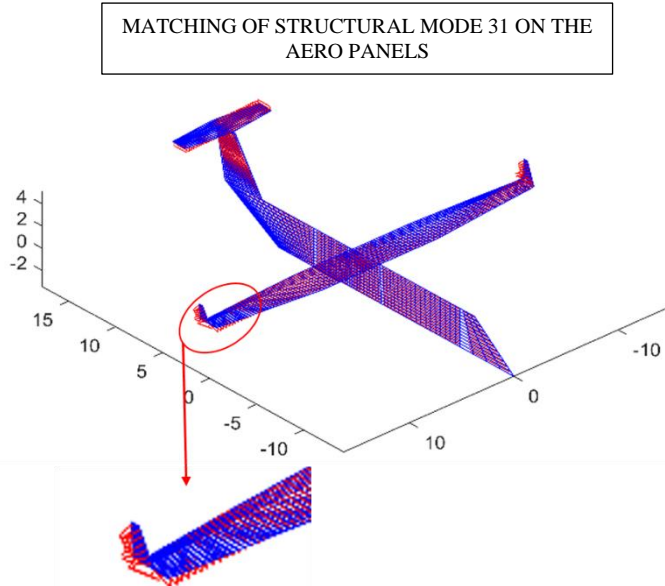


Fig. 50: Mode 31: anti-symmetric wing tip torsion/winglet bending

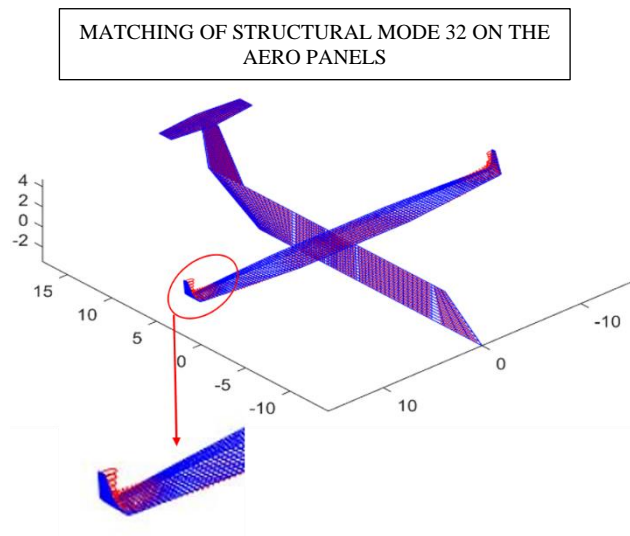


Fig. 51: Mode 32: Symmetric outer wing torsion/winglet bending

MATCHING OF STRUCTURAL MODE 33 ON THE
AERO PANELS

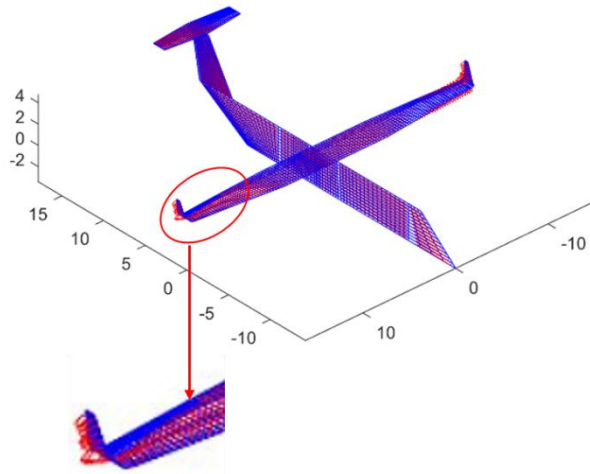


Fig. 52: Mode 33: Anti-symmetric outer wing torsion/winglet bending

By analyzing the previous figures, it appears evident the fact that the flutter modes strictly involve the winglet area.

Moreover, two kinds of flutter occurred for all the cases of study:

- Bell-shaped flutter;
- Sharp flutter.

Both flutter types appeared in all investigated cases, but at different speeds. In Fig. 53, the trend of the resulting modes frequencies and damping versus flight speed are plotted with reference to a generic case of investigation for which both flutter types are present in the speed investigation range ($K=1500$ Nm/rad; $M_{w_nominal}$).

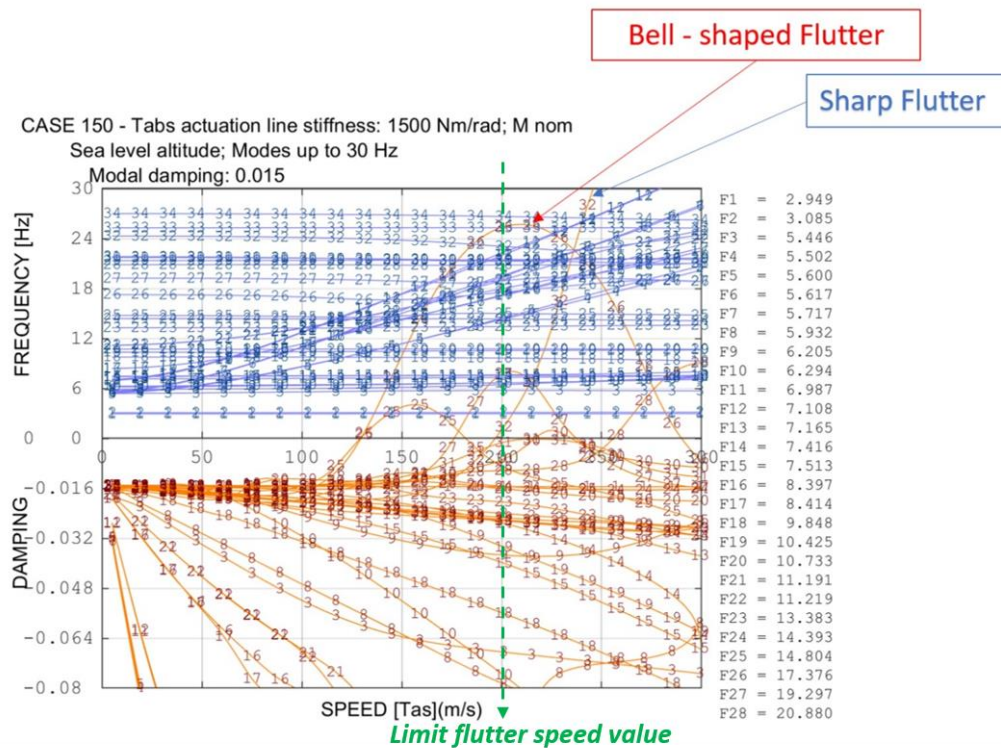


Fig. 53: Example of V-g plot on winglets tabs trade-off analysis, [31]

The results show that for the most critical combinations of flap and winglet tabs actuation line stiffness and inertial distributions, flutter modes poorly depend on the value of K. As a result, proper design solutions of the winglets tabs were studied to avoid any flutter instability within the aircraft certification envelope.

5.3.2.2 Flutter dynamics investigation

Repeating the procedure as already described in §5.3.1.2, the minimum flutter modal association was studied for the winglet modes 31, 32 and 33. A representation of the corresponding participation factors is reported in Fig. 54, Fig. 55 and Fig. 56 for K=400 Nm/rad and nominal value of the winglet tabs mass.

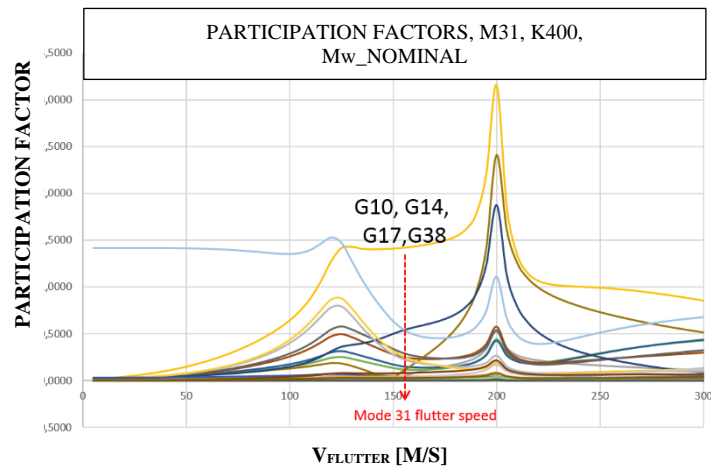


Fig. 54: Mode 31, Participation factors

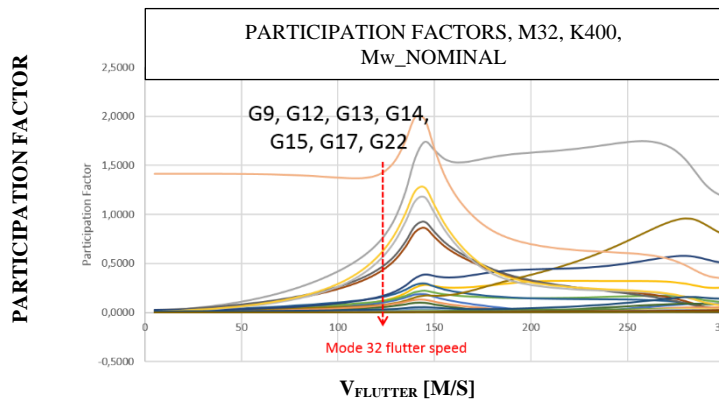


Fig. 55: Mode 32, Participation factors

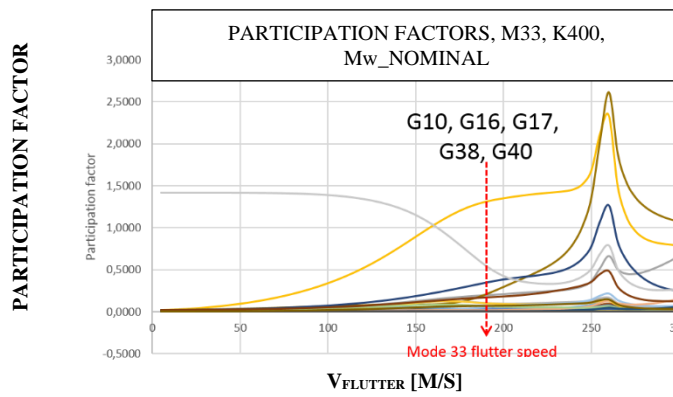


Fig. 56: M33, Participation factors

Main results of the flutter dynamics investigation are shown in Fig. 57.

Minimum modal association		
Flutter mode	Associated Modes	No Tabs harmonics
31	10, 14, 17, 38	
32	9, 12, 13, 14, 15, 17, 22	
33	10, 16, 17, 38, 40	

Mode	Flutter condition, all modes, K=400 Nm/rad; Mw_Nominal	Flutter condition, associated modes only, K=400 Nm/rad; Mw_nominal
31	V _{flutter} = 152.439 m/s; f = 14.418 Hz	V _{flutter} = 153.53 m/s; f = 14.359 Hz
32	V _{flutter} = 138.898 m/s; f = 16.718 Hz	V _{flutter} = 146.282 m/s; f = 16.368 Hz
33	V _{flutter} = 193.590 m/s; F = 18.497 Hz	V _{flutter} = 193.675 m/s; f = 18.564 Hz

Fig. 57: Minimum modal association, winglets tabs flutter modes

In all cases, many are the modes involved in the dynamics acting as supporting modes with respect to the principle ones, but among them, no tabs harmonics (or fundamental mode, at zero frequency) are present.

The design solutions suggested to abolish this complex flutter within the safety envelope are described in the following sections.

5.3.2.3 Massbalancing of winglets tabs

Further flutter analyses were then carried out in correspondence of trial values of winglets tabs massbalancing. Analyses assumptions are listed below ([31]):

- Two inertial configurations considered for the winglets: nominal mass (M_{w_nom}) and 30% mass increase (M_{w_30});
- Tabs actuation line stiffness, $K = 150$ Nm/rad;
- Decreasing values of Degree of Balancing considered from 100% up to 10%, (underbalancing).

A modular approach was followed by studying the effect of massbalancing on B2 tabs only (Fig. 28) and then on B1 and B2 tabs at the same time.

In any case positive effects in terms of flutter behavior were reached, as depicted in Fig. 58.

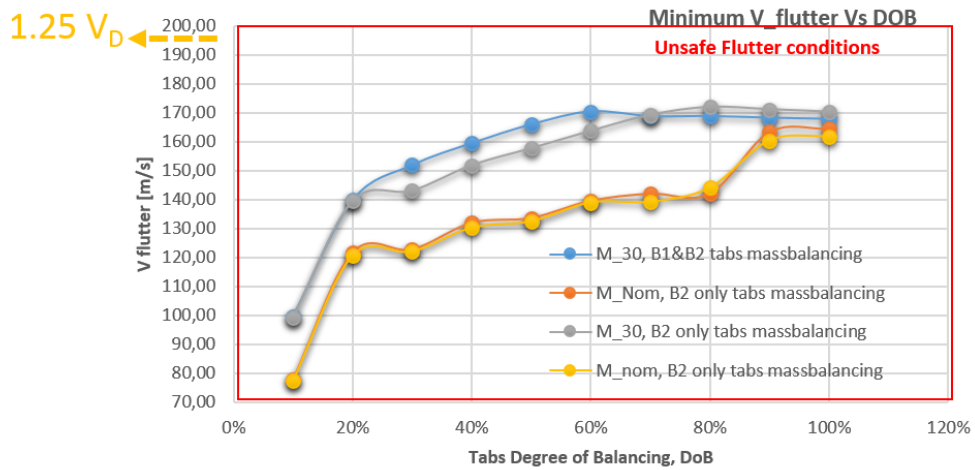


Fig. 58: Minimum flutter speed VS winglet tabs degree of balancing in two inertial configurations (nominal and 30% increase of the nominal mass)

For this reason, other analyses were performed by changing the trade-off parameters (except the inertial configurations) as follows:

- increasing the values of tabs actuation line stiffness, $K=400$ Nm/rad;
- overbalancing the tabs (DoB>100%).

Obtained results are shown in Fig. 59.

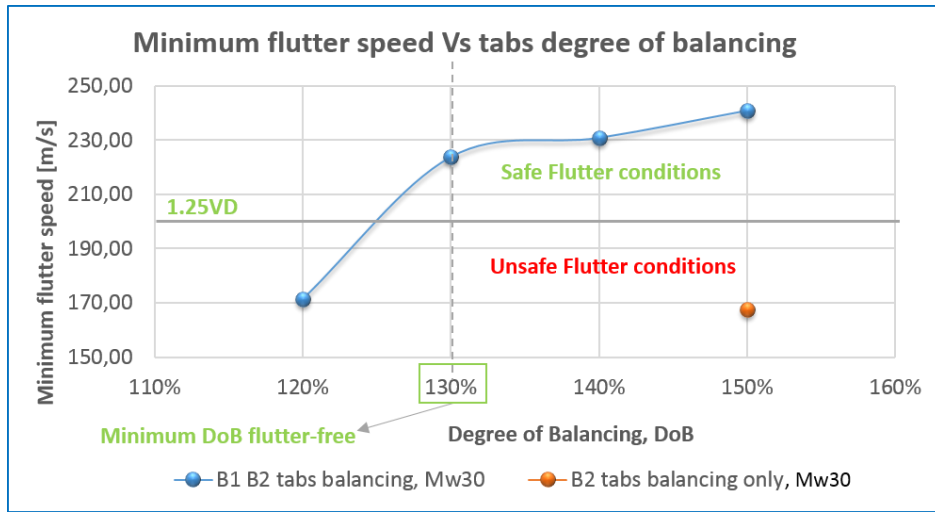


Fig. 59: Minimum flutter speed as function of tabs degree of balancing.

Fig. 59 presents the speed of the flutter modes (minimum value among the several occurring) as a function of winglets tabs degree of balancing, in case of massbalancing of both B1 and B2, and B2 tabs only. The orange point, corresponding with the latter condition, is unique since it returns a flutter within the speed certification envelope, although a DoB equal to 150%. On the other hand, the blue curve interpolates analyses results dealing with the case of B1 and B2 tabs concomitant massbalancing: it appears evident how the winglets tabs minimum degree of balancing required to expel flutter is equal to 130%.

This solution involves an unavoidable winglet mass increase with respect to its nominal mass value, as depicted in Table 5

Mass	[Kg]
M_{w_Nom}	36.90
M_{w_30}	47.97
$M_{bal_130\%}$	20.66
$M_{w_30} + M_{bal_130\%}$	68.63

Table 5: Winglet weight in case of 130% DoB

5.3.2.4 Wing/Winglet plug stiffness increment

A stiffness increment was adopted with respect to the interface plug between the wing and the winglet to prevent any flutter instabilities. This operation was

numerically handled by introducing a gain factor (F DMIK, in what follows) to the stiffness value of the plug.

For that purpose, a trade-off analysis was firstly performed to evaluate the F DMIK value - within the range [5; 100] - ensuring the worst case of flutter, for the sake of conservatism. Fig. 60.

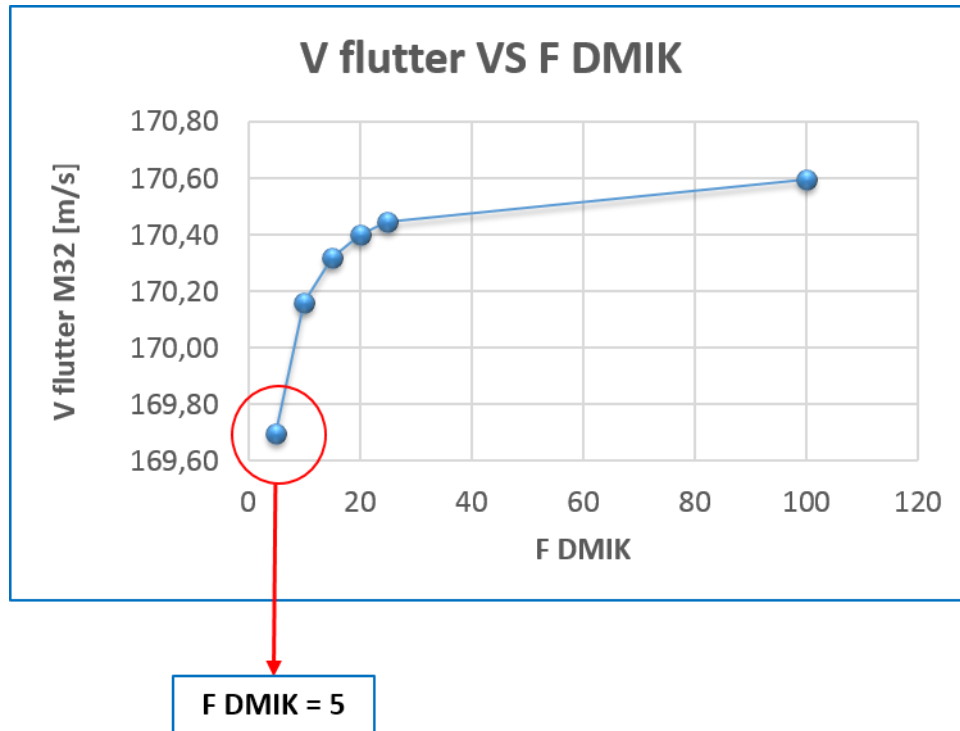


Fig. 60: Flutter speed trend as a function of plug stiffness gain factor

A new sensitivity was then performed to study the combined effect of the plug stiffness increment (F DMIK = 5) and winglet tabs massbalancing (B2 only and B1+B2 at the same time). Obtained results are presented in Fig. 61.

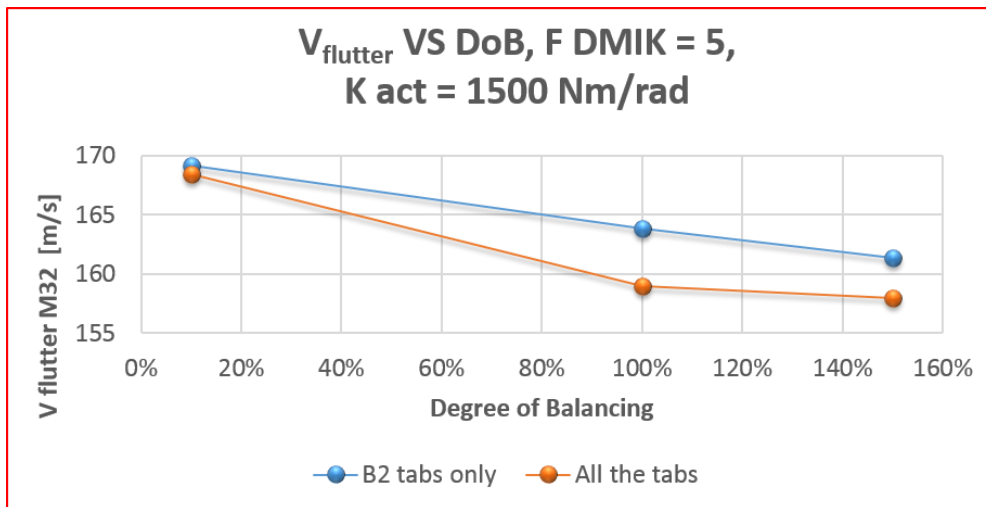


Fig. 61: Flutter speed trend as a function of tabs massbalancing, $F_{DMIK} = 5$

Fig. 61 shows a decreasing trend of the flutter speed corresponding with increasing values of winglets tabs massbalancing.

Winglet augmented mass - due to the presence of massbalancing – involves negative flutter behavior; this led to perform further trade-off analyses, under the assumptions:

- no tabs massbalancing;
- Gain factor of the plug stiffness (F_{DMIK}): decreasing values from 5 to 2;
- Gain factor of the tabs mass (F): decreasing values, in order to evaluate the minimum one to ensure flutter speed out of the speed certification envelope condition.

Fig. 62 and Fig. 63 collect the results obtained.

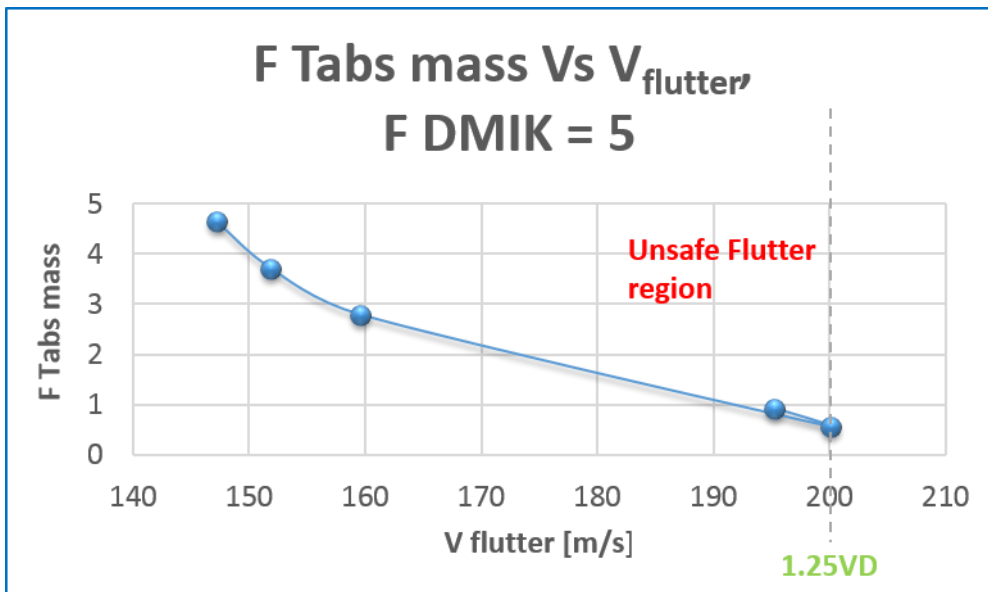


Fig. 62: Winglets tabs mass gain factor as function of flutter speed, with plug stiffness gain factor equal to 5

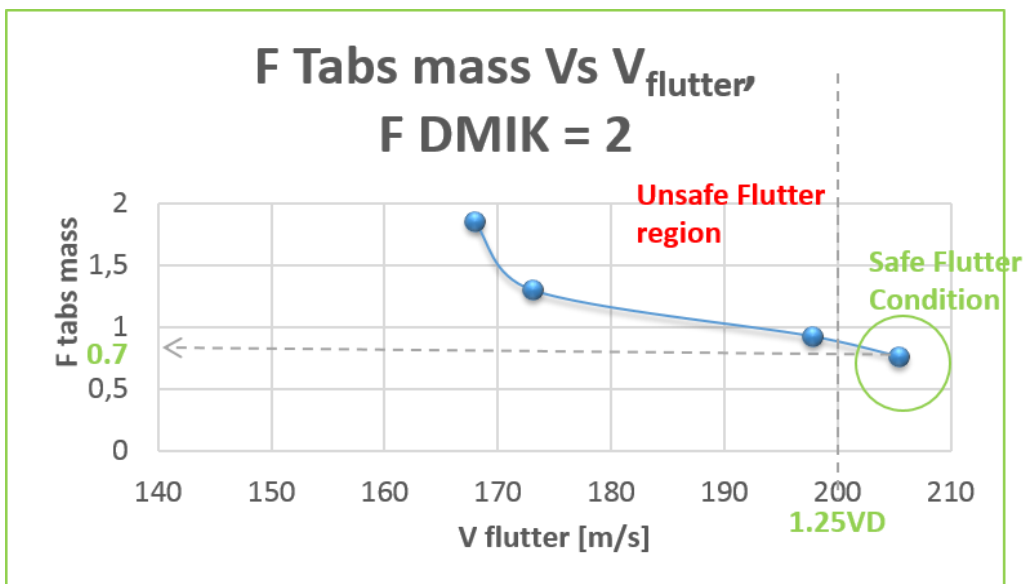


Fig. 63: Winglets tabs mass gain factor as function of flutter speed, with plug stiffness gain factor equal to 2

More in detail, trade-off results of Fig. 62 allowed for understanding flutter behavior improvement due to decreasing values of tabs mass. Nevertheless, no flutter speed resulted out of the speed certification envelope in this case.

Positive results were instead achieved by adopting plug stiffness gain factor (F DMIK) equal to 2 and winglets tabs mass gain factor (F) equal to 0.70 (Fig. 63): this led to a flutter speed greater than 200 m/s ($1.25 V_{\text{dive}}$).

This design solution, identified to guarantee flutter clearance, entails a winglet mass saving of 2.58 Kg, as described in Table 6.

Mass	[Kg]
$M_{\text{nominal winglet}}$	36.90
$M_{\text{nominal tabs}}$	8.60
$M_{\text{tabs} \times 0.7}$	6.02
$M_{\text{winglet_no_Tabs}} =$ $M_{\text{nominal wlet}} - M_{\text{tabs}}$	28.3
$M_{\text{winglet_no_Tabs}} +$ $M_{\text{tabs} \times 0.7}$	34.32

Table 6: Winglet weight in case of doublet stiffness of plug and 30% saving of tabs mass

5.3.2.5 Generalization of the results

For a generalization of the results, it is helpful to compare the following conditions in terms of outcomes:

- *Condition A*
 - No plug stiffness gain factor;
 - Tabs mass 100%;
 - Actuation line stiffness, $K = 1500 \text{ Nm/rad}$;
 - Winglet inertial configuration listed in Table 7.

M_WLET No- minal [Kg]	Flutter speed [m/s]	Mode ID
36.90	120	31, 32

Table 7: Flutter Results of Condition A

In this condition, flutter dynamics mainly involves the winglets (Fig. 64). Flutter instabilities of modes 31 and 32, occurring at a speed equal to 120.0 m/s

(Fig. 65), are sustained by supporting modes not associated with the winglet tabs; for this reason tabs massbalancing has no positive effect on flutter behavior.

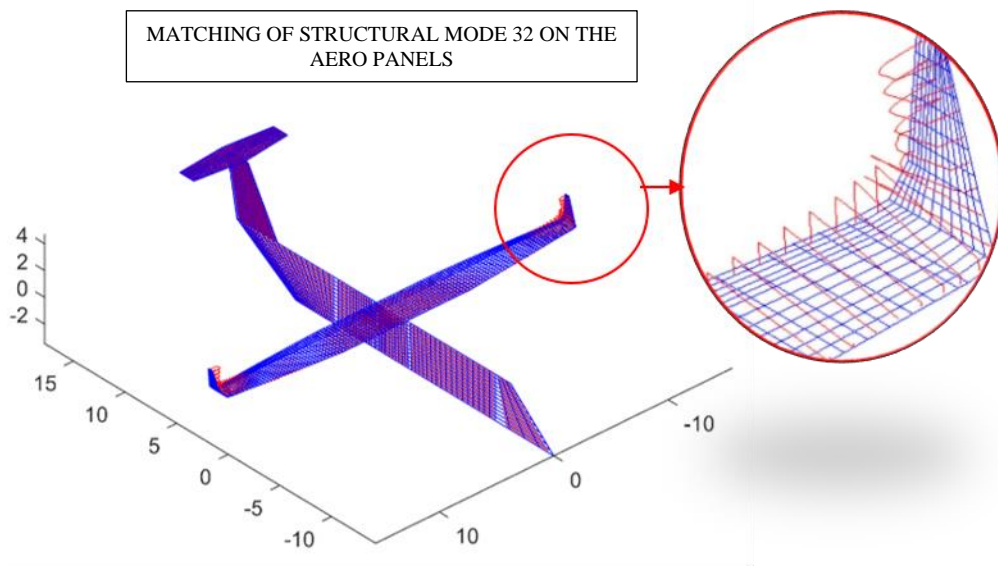


Fig. 64: Winglet bending mode (M32), in case of no plug stiffness gain factor and 100% tabs mass

CASE 150 - Tabs actuation line stiffness: 1500 Nm/rad; MwNom

Sea level altitude; Modes up to 30 Hz

Modal damping: 0.015; F DMIK=0; M tab 100%

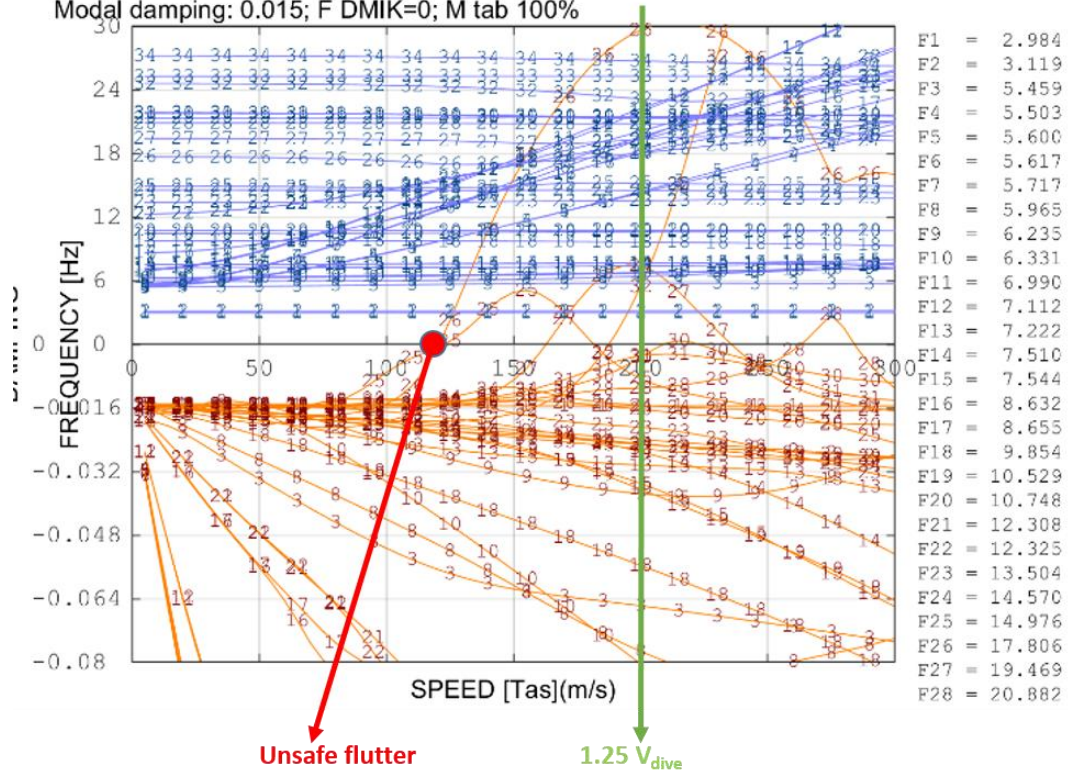


Fig. 65: V-g plot in the condition A

- Condition B
 - Plug stiffness gain factor = 2;
 - Tabs mass 70%;
 - Actuation line stiffness, $K = 1500$ Nm/rad;
 - Winglets inertial configuration shown in Table 8.

M_WLET Nominal + tabs mass X 70% [Kg]	Flutter speed [m/s]	Mode ID
34.32	205.40	35

Table 8: Flutter Results of Condition B

In this condition, flutter dynamics involves the wing (Fig. 66). M35 is a symmetric torsional-bending flutter mode in association with flap tabs harmonics, occurring at 205.40 m/s (Fig. 67). Tabs mass reduction ($F=70\%$) has beneficial effects on flutter dynamics, since the coalescence between winglets tabs harmonics and wing modes occurs above $1.25 V_{\text{div}}$.

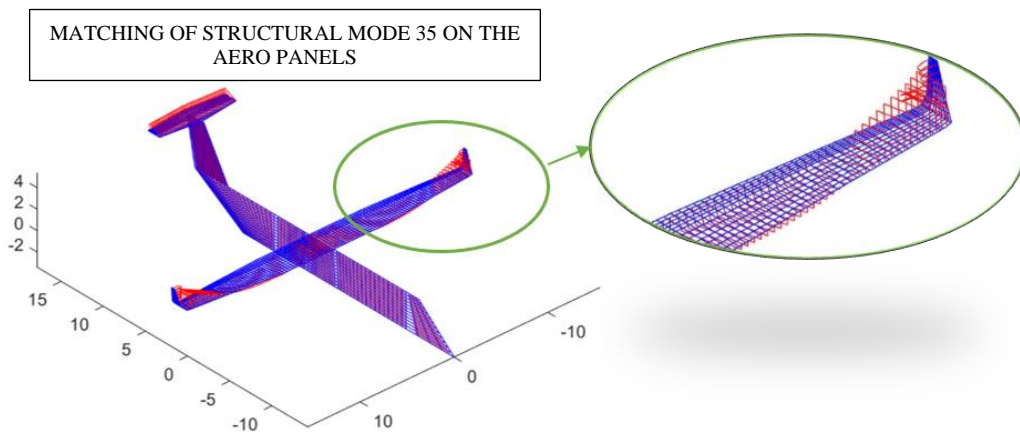


Fig. 66: – Symmetric wing torsional-bending mode in case of $F_{DMIK}=2$ and wlet tabs mass 70%

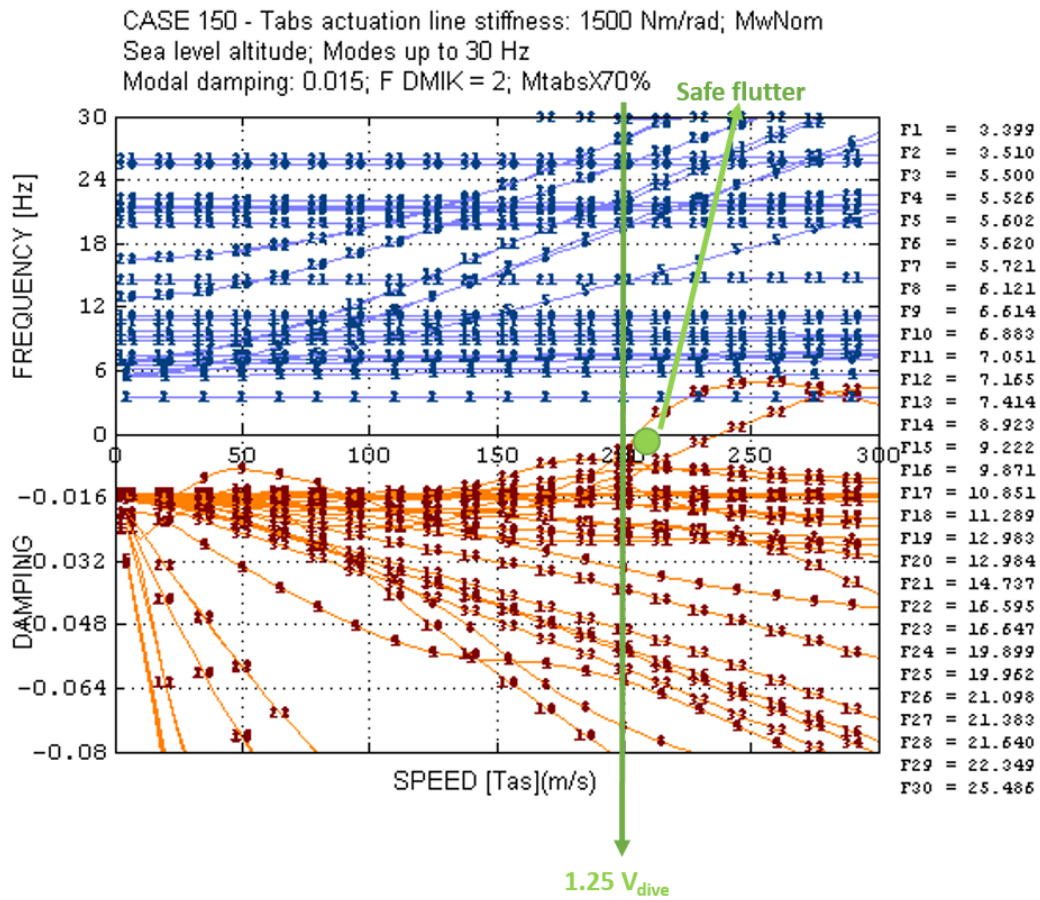


Fig. 67: V-g plot in the condition B

In light of all the previous considerations, winglet nominal configuration (condition B) was identified in terms of aeroelastic safety:

- Tabs actuation line stiffness: 1500 Nm/rad;
- Winglet mass baseline value;
- Tabs mass 70%.
- Plug stiffness Gain Factor: 2

Obtained results showed that the combination of morphing flaps and winglets is not responsible for any flutter instability; moreover, compliance with the airworthiness requirements for aeroelastic stability provided by CS-25 was demonstrated.

5.3.3 Free-Play Analyses Results, Harmonic Balance Method

This section describes flutter analyses results obtained in case of morphing winglet actuators free-play by using the harmonic balance method (see section 4.5).

Tabs actuators non-linearity has been described through a bi-linear stiffness law; the trend of the deflection θ as a function of the applied moment $M(\theta)$ is shown in Fig. 68.

Corresponding with two characteristic values of tabs actuation stiffness (Fig. 68):

1. $K_1 = 0 \text{ Nm/rad}$, if $-1^\circ < \theta < +1^\circ$;
2. $K_2 = 1500 \text{ Nm/rad}$, if $\theta < -1^\circ$ and $\theta > +1^\circ$,

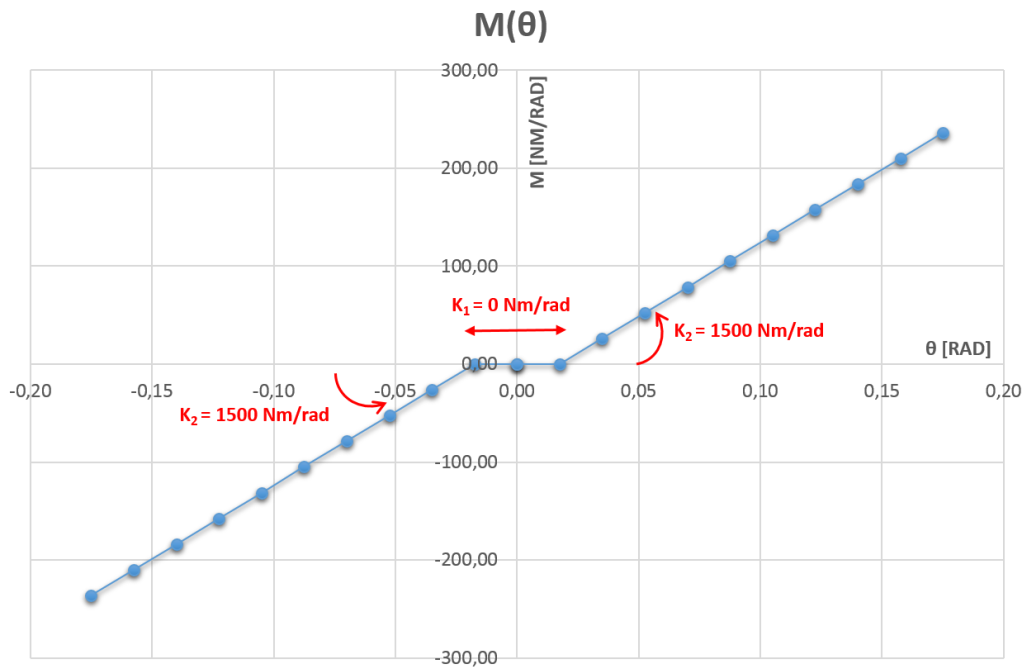


Fig. 68: Load-Deflection non-linear law

A sinusoidal signal was then introduced, $x=A\sin(2\pi f_{\text{flutter}}t)$, where A is the oscillation amplitude to change and f_{flutter} is the flutter mode frequency. It is important to underline how the equivalent stiffness is independent from the frequency.

By referring to the morphing winglet nominal configuration, the flutter mode resulted M35 (see Table 8), which frequency is $f_{M35}=21.767$ Hz.

This value was used to calculate the period of the oscillation imposed to the tabs.

Based on the relation shown in Fig. 68, different calculations corresponding with as many oscillation amplitude values were performed. Gained results are shown in Table 9 and in Fig. 69.

A [°]	K _{eq} [Nm/rad]
1	0,0000
2	1408,4189
3	1474,4108
4	1487,8081
5	1493,3661

Table 9: Equivalent stiffness of winglet tabs actuation line

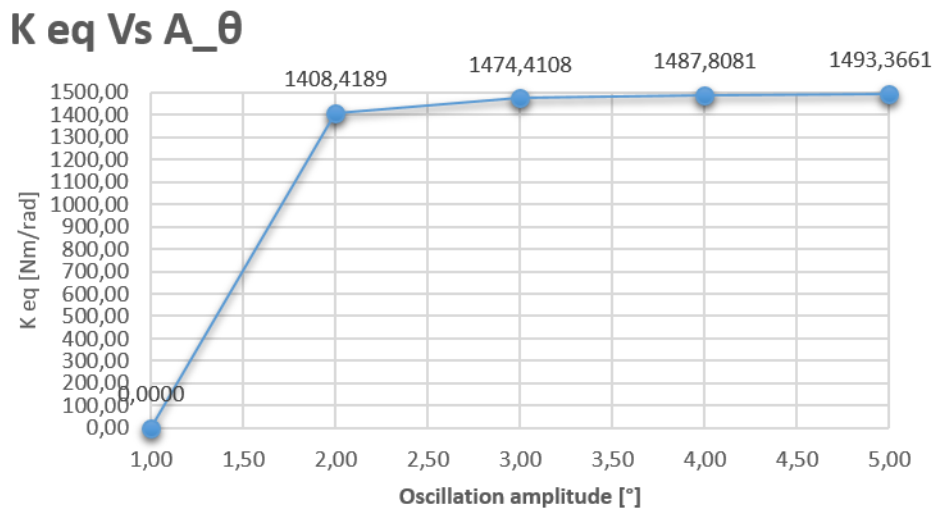


Fig. 69: Winglet tabs actuators equivalent stiffness Vs tabs oscillation amplitude

A flutter analysis was accomplished for each equivalent stiffness value depicted in Fig. 69. All obtained results are collected in Fig. 70.

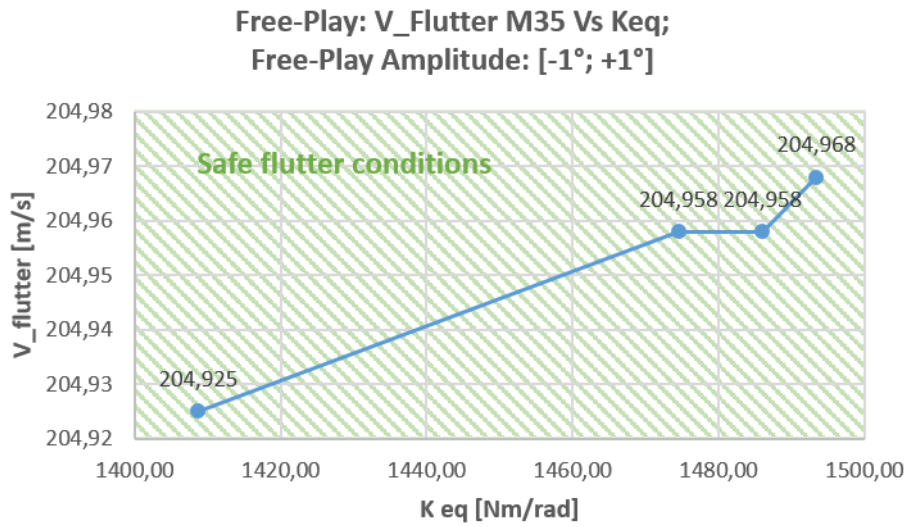


Fig. 70: Flutter analyses results in case of tabs actuators free-play

Interesting results emerge: even in case of tabs actuators free-play, M35 is an aerodynamically “safe mode”, since it exhibits all speed values are greater than $1.25 V_{\text{dive}}$ (200 m/s).

Although the presence of free-play, these results furthermore confirm an almost independence of the flutter speed from the actuation line stiffness values.

6 Morphing Wing – Safety and Reliability issues

6.1 Introduction

A functional analysis is a prerequisite to address safety and certification aspects of aircraft equipped with morphing systems. In particular, it is fundamental to identify firstly the aircraft functions which can be enhanced by the use of such devices and the corresponding aircraft flight segments. After that, all the potential failures of the morphing kinematics shall be evaluated by demonstrating that they do not compromise any aircraft general function and capability.

Despite the growing advances in morphing wing technologies, morphing devices continue to be perceived as highly difficult to certify by the aviation industry. Due to the augmented DOF, morphing wings are highly prone to aeroelastic instabilities with respect to conventional wing architectures. However, beyond structural or any other consideration of airworthiness nature, the novel aircraft functions enabled by morphing systems imposes a thorough examination of the associated risks which may impact on aircraft flight capabilities and crew workload. However, as investigated in this work, for systems related to structural load alleviation and control functions, the safety classification and relevant safety figures shall also be managed as a structural design driver. This is because a safety factor (SF) is recommended for those failures whose probability of occurrence is higher than 10^{-5} per flight hour.

The safety properties of morphing devices are established primarily by analysis. The potential failures of electromechanically actuated morphing devices, for instance, may range from jamming to loss of power supplies and control lanes, thus resulting in specific technical requirements that can be traced to the top-level aircraft functions. An example of a fault tree of an electromechanical actuator is given in Fig. 71. The extensive use of EMA actuation in the most advanced examples of morphing devices confirms the sensitivity of this issue given the safety impact of morphing wing devices on aircraft operation.

This chapter provides general guidelines for safety-driven design of morphing devices. The study begins with a qualitative analysis of the morphing wing functions at subsystem level to identify potential design faults, maintenance and crew workload impact, as well as external environment risks. The severity of the hazards are determined and ranked in specific classes, indicative of the maximum tolerable probability of occurrence for a specific event, resulting in safety design objectives. A list of morphing system-level functional and safety objectives is

then proposed. These objectives feed the requirements definition process, thus assigning reliable and verifiable constraints to the morphing systems design. Some fault trees for specific failure cases are also detailed. The proposed analyses establish the benefits and needs for a morphing wing incorporating a morphing flap and an adaptive winglet. Nevertheless, such a recommended approach is likely to be applicable to a wider variety of morphing devices installed in aircraft with different adaptive surfaces or functions.

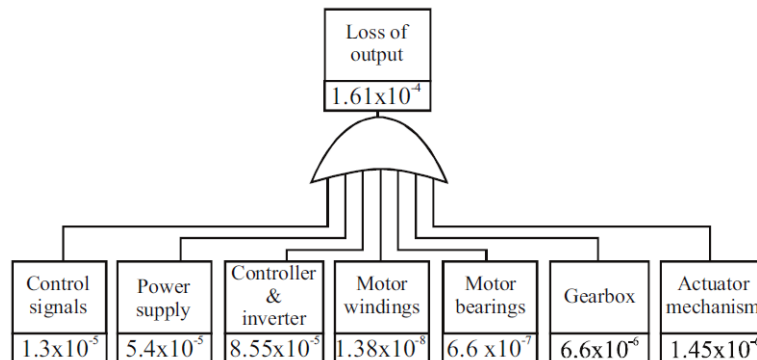


Fig. 71: Example of electromechanical Actuator fault tree with failure rates per hour

As for all the other aircraft control surfaces and systems, the real challenge of this work is to show whether the safety targets are met until the single system is individually assessed and the interaction between conventional and adaptive systems namely performing different functions are collectively evaluated at A/C system level. Such predictions are supported by aeroelastic simulations aiming at demonstrating the aeroelastic impact of potential failures involving critical sub-components of the morphing architectures to preserve the essential features of safety.

6.2 Safety Analysis: general approach

According to the EASA CS-25 regulations applicable to large commercial aircraft, safety assessments of aircraft devices consist of three major phases, i.e. Fault and Hazard Assessment (FHA), Preliminary System Safety Assessment (PSSA), System Safety Assessment (SSA), which in turn consider the interaction among aircraft systems, software and hardware components, and all the interfaces including pilot and crew behavior. In this logic, system functions are firstly qualitatively examined to identify potential faults along with external environ-

mental risks. The severity of these hazards is thus determined and classified, indicative of the maximum tolerable probability of occurrence. After that, the link between faults at sub-systems level and their end-effects are evaluated in the FHA phase, to identify the actual system constraints throughout the system lifetime. Each hazard is quantitatively examined in a top/down fashion, from the events to their causes, until failures of the basic components are categorized. On the basis of the probabilities assigned to the failure events of the elementary components, the probability of occurrence of the top event is calculated. Such a quantitative analysis is usually achieved with the Fault Tree (FT) technique.

Due to the novelty of the morphing wing technology, the literature on the safety effects of morphing devices is very poor. However, some general concepts relating the aircraft functions to the capabilities of a morphing winglet, for instance, allows identifying such a device as a “Safety Critical” structure. This means that any loss of the system control could result in a “catastrophic” event for the aircraft due to the potential risks for the aircraft wing structure. In this context, flutter is probably one of the major risks which shall be managed in the design process by considering either free wheeling of the morphing tabs or jamming of the actuation systems. It follows that, from the fault hazard assessment standpoint, the probability of its occurrence must be proved below the threshold value of $<10^{-9}$ per flight hour.

The main drivers in the safety-driven design of morphing systems are the already-mentioned CS-25 regulations as well as the Aerospace Recommended Practices SAE ARP 4754a ([45]) and SAE ARP4761 ([46]). The CS-25 safety regulation requires the general safety assessment process shown in Fig. 72.

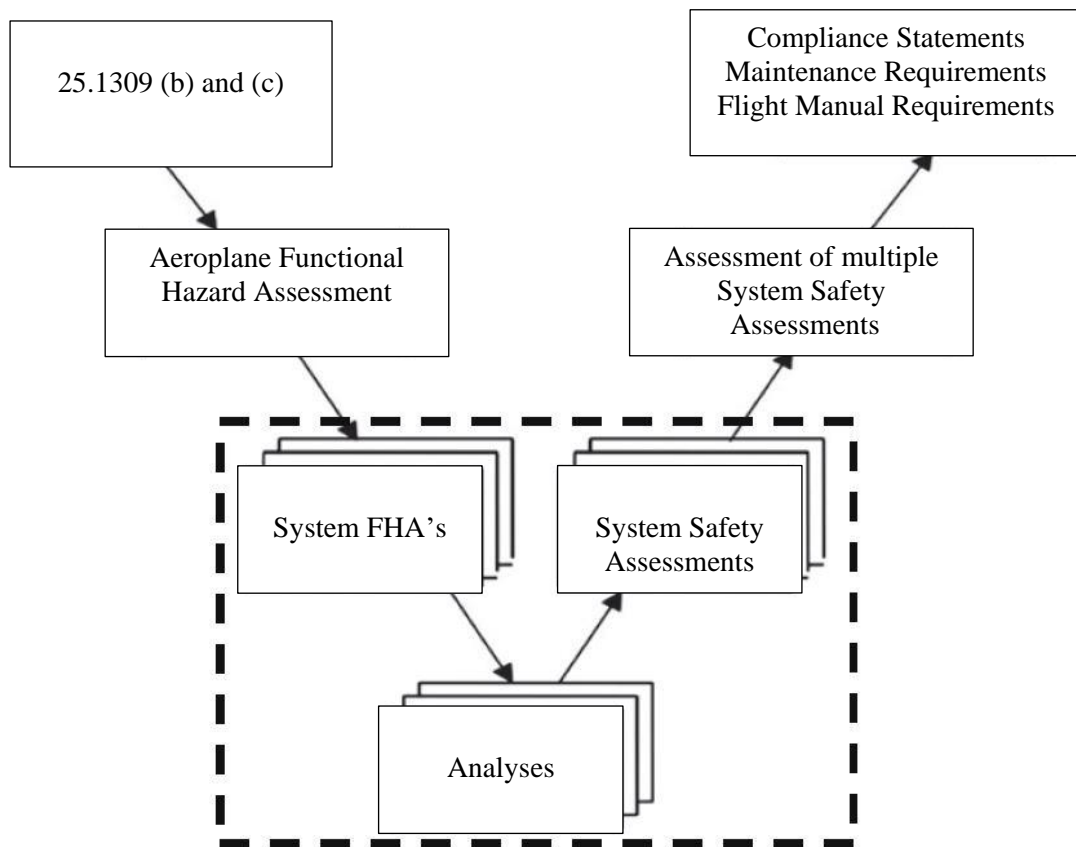


Fig. 72: CS-25 safety assessment process overview

A logical and acceptable inverse relationship must exist between the Average Probability per Flight Hour and the severity of Failure Condition effects, as shown in Fig. 73. Catastrophic failures shall be extremely improbable and shall not result from a single failure, [2]. The upper limit for the average probability per flight hour for Catastrophic Failure Conditions is 10^{-9} , which establishes an approximate probability value for the term “Extremely Improbable”. On the other hand, failure conditions having less severe effects could be relatively more likely to occur, with upper average probability limits equal to 10^{-7} and 10^{-5} per flight hour for Hazardous and Major, respectively.

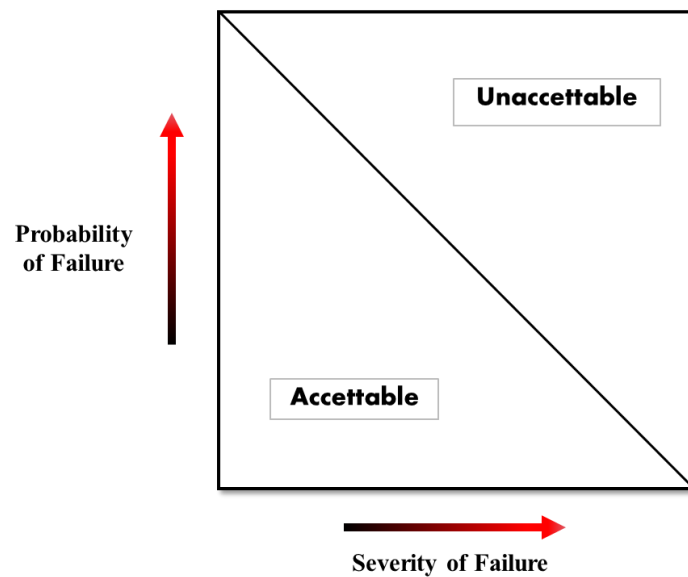


Fig. 73: Relationship between Probability and Severity of Failure Condition Effects, [2]

As part of the safety-driven design flow, after safety requirements have been issues through the Aircraft level Functional Hazard Assessment, they need to flowdown to the next level (the morphing wing system FHA, referred to as “System’s FHA”), and subsequently to lower levels, such us the morphing components FHA. If the aircraft is still generic, a generic set of aircraft level functions can be arbitrarily chosen to define high-level links between the enhanced morphing system functions and the standard aircraft functions by identifying, at the same time, the criticalities associated with the failure conditions.

The “System Safety Assessment (SSA)” regards a quantitative analysis of the Fault Trees generated for those potential failures with hazardous or catastrophic consequences. The reliability data of the system components are then necessary to calculate the basic events probability figures and may be typically requested to the components suppliers (commonly required by contract and by equipment specification) prior to the system integration and assembly phases.

The following paragraphs elaborate the safety process assessment approach described above by focusing on two morphing systems:

- Morphing Flap
- Adaptive Winglet

6.2.1 Functional Hazard Assessment - FHA

Functional hazard assessment is a safety analysis at system/aircraft functional level. As reported on the already-mentioned SAE ARP 4754a [45], the FHA “*examines aircraft and system functions to identify potential functional failures and classifies the hazards associated with specific Failure Conditions. The FHA is developed early in the development process and is updated as new functions or Failure Conditions are identified. Thus, the FHA is a living document throughout the design development cycle*”. The functional failures are thus identified with the associated severity. Then, qualitative requirements are set in this analysis (redundancy, Functional Design Assurance Level (FDAL), specific monitoring, etc.).

When dealing with a morphing device, the following failure scenarios are very likely to occur:

- Total loss of function,
- Partial loss of function,
- Erroneous provision of function, and
- Inadvertent provision of function

Within the total loss of function, we may include very dangerous conditions such as *uncommanded/undamped free floating* of the moveable surface or *detected/undetected runaway of the morphing surface* involving mainly the actuators.

The hazards associated with specific failure conditions are classified according to the safety effect, as follows [45]:

NO SAFETY EFFECT (NSE) “Failure Conditions that would have no effect on safety; for example, Failure Conditions that would not affect the operational capability of the aeroplane or increase crew workload”.

MINOR (MIN) “Failure Conditions which would not significantly reduce aeroplane safety, and which involve crew actions that are well within their capabilities. Minor Failure Conditions may include, for example, a slight reduction in safety margins or functional capabilities, a slight increase in crew workload, such as routine flight plan changes, or some physical discomfort to passengers or cabin crew”.

MAJOR (MAJ) “Failure Conditions which would reduce the capability of the aeroplane or the ability of the crew to cope with adverse operating conditions to the extent that there would be, for example, a significant reduction in safety margins or functional capabilities, a significant increase in crew workload or in conditions impairing crew efficiency, or discomfort to the flight crew, or physical distress to passengers or cabin crew, possibly including injuries”.

HAZARDOUS (HAZ) “Failure Conditions, which would reduce the capability of the aeroplane or the ability of the crew to cope with adverse operating conditions to the extent that there would be: (i) A large reduction in safety margins or functional capabilities; (ii) Physical distress or excessive workload such that the flight crew cannot be relied upon to perform their tasks accurately or completely; or (iii) Serious or fatal injury to a relatively small number of the occupants other than the flight crew”.

CATASTROPHIC (CAT) “Failure Conditions, which would result in multiple fatalities, usually with the loss of the aeroplane. (Note: A “Catastrophic” Failure Condition was defined in previous versions of the rule and the advisory material as a Failure Condition which would prevent continued safe flight and landing.)”.

Fig. 74 shows how the safety effects on flight crew, passengers, and aircraft are classified in terms of severity. It comes up that large reduction in aircraft functional capabilities or safety margins is classified as HAZ whereas CAT events result in hull loss.

Effect on Aeroplane	No effect on operational capabilities or safety	Slight reduction in functional capabilities or safety margins	Significant reduction in functional capabilities or safety margins	Large reduction in functional capabilities or safety margins	Normally with hull loss
Effect on Occupants excluding Flight Crew	Inconvenience	Physical discomfort	Physical distress, possibly including injuries	Serious or fatal injury to a small number of passengers or cabin crew	Multiple fatalities
Effect on Flight Crew	No effect on flight crew	Slight increase in workload	Physical discomfort or a significant increase in workload	Physical distress or excessive workload impairs ability to perform tasks	Fatalities or incapacitation
Allowable Qualitative Probability	No Probability Requirement	<---Probable--->	<---Remote--->	Extremely <-----Remote----->	Extremely Improbable
Allowable Quantitative Probability: Average Probability per Flight Hour on the Order of:	No Probability Requirement	<-----> <10 ⁻³ Note 1	<-----> <10 ⁻⁵	<-----> <10 ⁻⁷	<10 ⁻⁹
Classification of Failure Conditions	No Safety Effect	<-----Minor----->	<-----Major----->	<--Hazardous-->	Catastrophic
Note 1: A numerical probability range is provided here as a reference. The applicant is not required to perform a quantitative analysis, nor substantiate by such an analysis, that this numerical criteria has been met for Minor Failure Conditions. Current transport category aeroplane products are regarded as meeting this standard simply by using current commonly-accepted industry practice.					

Fig. 74: Required probability figures versus safety classification

6.2.2 System Safety Assessment—Fault Tree Analysis

This section deals with the basic principle of the fault tree technique used by in the preliminary system safety assessment activity (PSSA). Fault tree analysis (FTA) allows checking that the qualitative and quantitative requirements associated to each Failure Condition and expressed in the FHAs are met. FCs classified as NSE (NO SAFETY EFFECT), MIN (MINOR) and MAJ (MAJOR) do not need to be modelled by a fault tree (FT), according to the CS25 book 2 (Means Of Compliance—[2]). A detailed description of the FTA technique can be found in the appendix D of the “Guidelines and methods for conducting the safety assessment process on civil airborne system and equipment”—ARP 4761 ([46]).

A fault tree analysis (FTA) is a deductive failure analysis, which focuses on one particular undesired event (Failure Condition). A FTA is a top-down safety analysis technique that is applied as part of the PSSA to determine what single failures or combinations of failures at the lower levels (basic events) may cause or contribute to each Failure Condition. It uses Boolean logic gates to show the relationship of failure effects to failure modes. A basic event is defined as an

event which for one reason or another has not been further developed (the event does not need to be broken down to a finer level of detail in order to show that the system under analysis complies with applicable safety requirements). A basic event may be internal (system failure) or external (e.g. icing condition, fire) to the system under analysis and can be attributed to hardware failures/errors or software errors. Probability of individual failures is only assigned to the hardware (HW). The occurrence of software (SW) errors are probabilistic but not in the same sense as hardware failures. Unlike hardware failures, these probabilities cannot be qualified. No SW failures were thus considered in this work. The FT calculation produces the Minimal Cut Sets (MCS), i.e. the shortest logic and combination of independent basic failures that lead to the Failure Condition. The order of the MCS is the number of elements found in the MCS. Failure Conditions that are classified as CAT shall comply with the fail safe criteria. This means that no single failure shall lead to the occurrence of a CAT Failure Condition. Therefore, MCS of order equal to 1 are not acceptable for CAT Failure Conditions. The hypotheses and common data used by the fault trees are recalled in the following paragraphs. One individual FT is generally built for each Failure Condition coming from the FHAs whose safety classification is equal or more than MAJOR.

The FC is the top event of the fault tree. Its average probability of occurrence per flight hour (FH) is deduced from the quantification of all MCS generated by the calculation of the fault tree.

6.2.3 *Active Versus Hidden Failures*

Both active and hidden failures shall be considered in the fault tree analyses. Active failures are failures that can be detected by the flight crew when they occur during the current flight. For active failures, a mean flight time, T_0 , must be used in the calculation of the FC. Clean Sky 2 partners agreed to use a mean flight time equal to 1 h that has been considered as an appropriate value for regional aircraft. However, for some specific scenarios, a proper “exposure” time can be used in case a Failure Condition is expected to occur only in a specific flight phase. Hidden failures (named also latent/passive/dormant failures) are failures not detected by the flight crew or detected but not reported. Such failures shall be checked at a certain moment of the aircraft life, according to airworthiness requirement during periodic inspections for maintenance purpose. Safety check intervals or maintenance time (MT) must be considered in the calculation of the

FC involving hidden failures. The MT value is set based on the usual checks (periodic inspections) of the aircraft. The standard safety check intervals (A checks, B checks ...) have been considered in the quantification of the FTs. An interval of 8000 flight hours was considered between maintenance checks, i.e. disassembly and inspection of all hinges for detection and elimination of all dormant failures. For equipment that is never inspected, we use the aircraft lifetime. This value comes from “Fatigue Loads design criteria”. MT of “60,000 h” was set as a standard value but a calculation with a more conservative value of 87,600 h was considered, as reported in [47].

6.2.4 On safety factor

The structural damage tolerance and loads are out of the PSSA scope. Structure specialists in separated documents address such specific safety issues. However what is requested is to identify the systems that may exert loads on structural parts when failures occur as explained in the CS25.303 section “Factor of safety” [2]: “...Unless otherwise specified, a factor of safety of 1.5 must be applied to the prescribed limit load which are considered external loads on the structure” (Fig. 75).

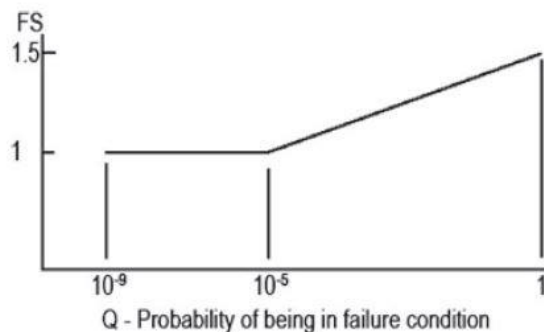


Fig. 75: Safety factor vs probability in failure condition

6.3 Morphing devices: Aircraft level functions

An assessment of the generic A/C level functions is proposed in [45]. The functions which may be namely improved by integrating morphing control surfaces, like morphing flap and adaptive winglet, into an aircraft wing are listed in Table 10. In particular, the use of these devices namely impacts on the following A/C level functions:

- Drag reduction

- Lift adaptation
- Gust/Load alleviation
- Vibration and Fatigue control

AIRCRAFT FUNCTIONS
2. Plan, Generate and Control A/C movement
2.2 Generate and Control aircraft movement
2.2.5 Control A/C Aerodynamics Configuration
2.2.5.1 Control Lift and Drag
2.2.6 Protect Aerodynamic Control
2.2.6.1 To provide protection against turbulence effects
2.2.6.2 To provide protection against stall load
2.2.7 Provide aerodynamic control forces
2.2.8 Support Supplemental flight control
2.2.8.1 To provide overload protection and A/C load protection
2.2.8.2 To provide protection against manoeuvres effects
2.2.13 Generate lift
2.2.14 Provide aerodynamic stability
8. Provide containment and internal support
8.1 Provide containment
8.1.2 Provide structural integrity and loads distribution
8.1.2.1 To provide fatigue protection

Table 10: Aircraft functions impacted by Morphing Wing concept, [45]-[46]

A very high level description of the morphing device is generally required to understand the above reported functional breakdown. Overall, these systems aim at reducing wing drag, at controlling wing lift distribution and at reducing wing loads (including vibrations and fatigue loads). In addition, the wing structural integrity can be also taken into account due to the structural load alleviation / protection / control function, as envisaged in A/C function 8 “Provide containment and internal support”.

6.4 Morphing flap

The morphing flap is a high lift device capable to generate extra lift during take-off and landing. Additionally, it is conceived to drastically enhance aircraft aerodynamic performance in high-lift conditions also through the mode 2 and mode 3. Less drag directly reduces fuel consumption. However, in case of system deployment in high speed conditions for drag minimization or lift adaptation, any possible detachment of the device or erroneous deployment may impact on aircraft safety. More complex functions such as maneuver load alleviation or gust load alleviation shall be excluded for morphing flap due to the current technological limits. The FHA of the morphing flap is shown in Table 11.

Morphing Flap FHA Table									
A/C function	Phase	Failure Scenarios	Failure Effects	Failure condition	Severity	Justification for classification	Crew detection	Recovery Action	Design parameters
High lift generation	Take Off/Landing	Flap loss of function: surface jammed (symmetric condition, both extraction failed)	Reduction of lift for landing	Flap loss of function: surface jammed (symmetric condition, both extraction failed)	MAJ	Slight increase in pilot's work-load	Warning	Land at higher speed, limitation of sustained wind conditions.	Investigate robustness of lift reduction predictions in order to obtain an estimate for precision tolerance
High lift generation	Take Off/Landing	Flap loss of function: surface jammed (asymmetric condition, single extraction failed)	Reduction of lift for landing. Reduced authority on roll and yaw	Asymmetric Flap loss of function: one surface jammed due to single extraction fail	MAJ	Slight increase in pilot's work-load	Warning	Land at higher speed, limitation of sustained wind conditions. Reduced lateral authority. Consider flap retraction in case of unfavourable cross-wind	Investigate robustness of lift reduction predictions in order to obtain an estimate for precision tolerance
Drag reduction	Climb/cruise	Undetected dynamic motion	Wing flutter onset, total loss of morphing flap structure	Free oscillations of the tabs in air-stream not detected by onboard systems	NSE	Omitted (N/A) in force of the implemented design process. Rational analysis must prove that morphing flap device has no impact on wing flutter clearance also	Large vibrations	Immediate Speed reduction, restore baseline shape, deactivate morphing.	Demonstrate system device compliance with paragraph 25.629 (Acceptable MOC). Add redundant displays moni-

						in case of uncontrolled motion.			toring oscillations levels of the system.
Drag reduction	Climb/cruise	Loss of morphing flap control	Wing efficiency degradation and increased fuel consumption	Loss of morphing kinematic control	MAJ			Reduce speed and avoid severe turbulence in order to prevent ultimate loads, automatic recomputation of A/C block fuel	Computation of aircraft fuel consumption and allowed range even in case of loss of control.

Table 11: Aircraft functions impacted by Morphing Flap concept, [47]

On the basis of the probabilities assigned to the failure events of the basic components, the probability of occurrence of such top events shall be then calculated through the Fault Tree (FT) technique.

Based on what described in the previous sections regarding the morphing flap architecture and all considerations about the FHA, two different failure scenarios have been considered in the fault tree analysis concerning the morphing flap:

- 1st failure scenario, involving *high lift generation function* (morphing mode 1);
- 2nd failure scenario, involving *undetected inadvertent morphing flap tab control at high speed function* (morphing mode 2).

High lift generation function was judged compromised in case of the following dissociated failure (right or left side):

1. Deployment system failure
2. Morphing system failure ;

Undetected inadvertent morphing flap tab control at high-speed function was assessed mined in case of the following dissociated failure (right or left side):

1. Loss of morphing kinematic control;
2. Control system failure;
3. Power-off brake failure;
4. Inadvertent tab deflection – undetected.

All listed levels were furthermore exploded according with a rational “top-down” approach (Fig. 76 and Fig. 77). Reliability Workbench – Isograph® ([48]) was used to perform the fault tree analyses, by extracting the lowest level events probability from literature, [49].

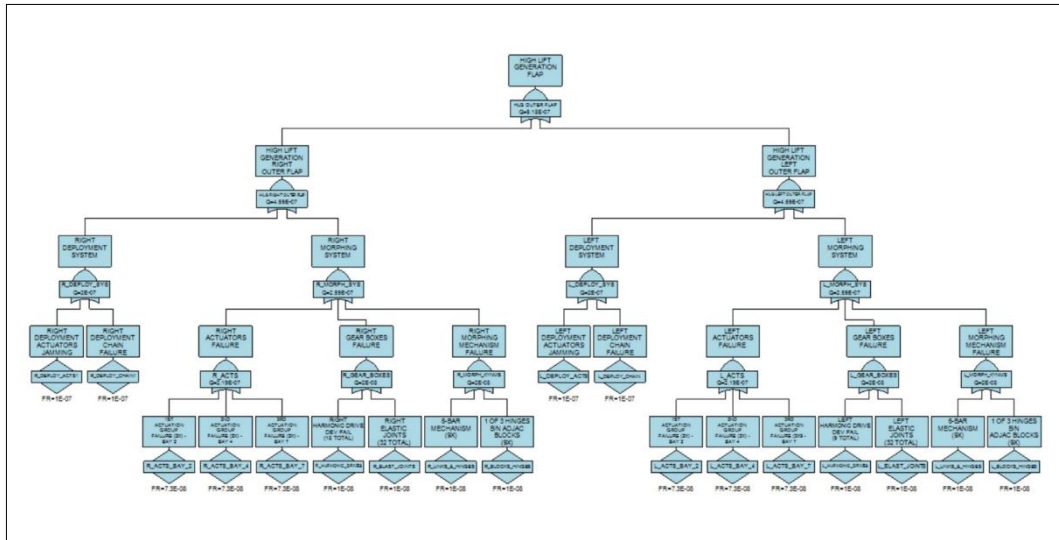


Fig. 76: Morphing Flap High Lift Generation Fault Tree Analysis

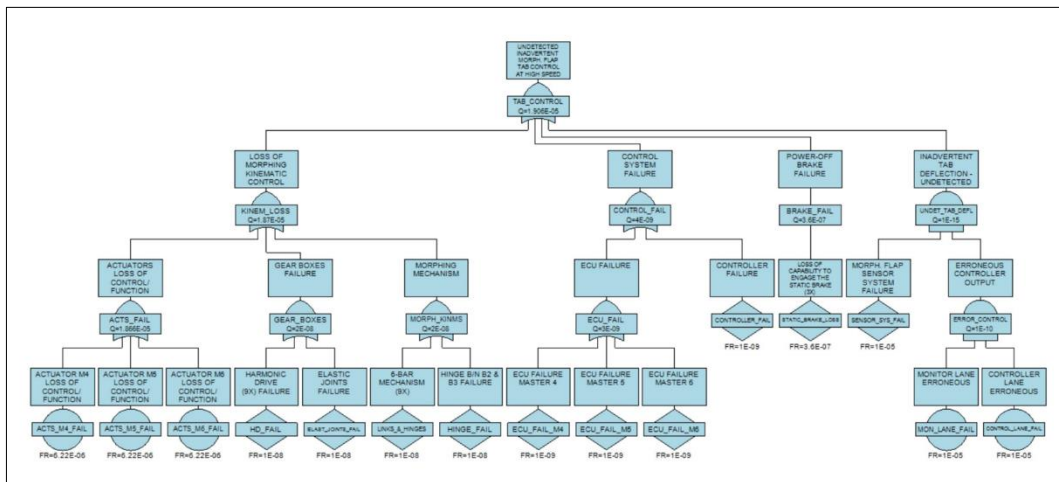


Fig. 77: Morphing flap Undetected Inadvertent tab control at high speed Fault Tree Analysis

In Fig. 76 and Fig. 77 “undeveloped events” are depicted as diamonds by the FT tool. Obtained results show that

- High lift generation function failure meets the required severity of MAJ;
- Undetected inadvertent tab control at high speed meets the required severity of MAJ. In this case, the safety margin is lower since actuators failure events are connected by a logic OR gate, which means that they shall occur with mutual exclusivity to cause the identified hazard.

In order to demonstrate the device compliance with flutter requirements even in case of free floating failure, the following aeroelastic simulations were carried out:

6.5 Morphing winglet

The safety-driven design of an adaptive winglet implies a thorough examination of the potential hazards associated with the system faults, by taking into account the overall operating environment and functions. The use of such a device namely impacts on the following A/C level functions:

- Drag reduction
- Load alleviation
- Fatigue improvement

The potential failures identified in the preliminary FHA are the following (Table 12):

Hazard description	Potential impact	Performed and planned actions to tackle the hazard
Uncontrolled dynamic motion	Morphing tabs moving undamped in airflow (control surfaces flutter) which may cause structural damages of the A/C wing	Flutter simulations and trade-off analyses on control surfaces Immediate A/C speed reduction
Detected jamming of one adaptive winglet (either left or right)	Detected drag increase and increased loads	Reduce speed and avoid severe turbulence in order to prevent ultimate loads, automatic recomputation of A/C block fuel

Undetected loss of control of one adaptive winglet (either left or right)	Increased fuel consumption and reduced controllability	Reduce speed and avoid severe turbulence in order to prevent ultimate loads, automatic recomputation of A/C block fuel
---	--	--

Table 12: Potential failures identified in morphing winglet preliminary FHA

A more detailed description of the MWL FHA is given in Table 13.

MWL FHA Table									
A/C function	Phase	Failure Scenarios	Failure Effects	Failure condition	Severity	Justification for classification	Crew detection	Recovery Action	Design parameters
Load control/ Load alleviation	Climb/Cruise and others	Uncontrolled dynamic motion	MWL tab1 and/or tab2 moving undamped in airflow (control surfaces flutter)	Possible structural damage of the A/C wing.	CAT	Loss of A/C, emergency pilot's actions such as immediate speed reduction to safe aircraft	strong vibrations, A/C uncontrollable	Immediate speed reduction, emergency landing	MWL flutter simulations and trade-off analyses on control surfaces
Load control/ Load alleviation	Climb/Cruise and others	Detected jam of one MWL (either left or right)	Uncontrolled MWL static tab1 and/or tab2 deflection on one side; increased drag and/or increased loads	Detected drag increase and increased loads	MAJ	Physical discomfort for passengers, pilot's workload slightly increased, aircraft structure is seized for jam according to CS-25	Warning	Reduce speed and avoid severe turbulence in order to prevent ultimate loads, automatic recomputation of A/C block fuel	Sizing loads shall include jamming conditions
Load control/ Load alleviation	Climb/Cruise and others	Undetected Run-away of left AND right MWLs	Uncontrolled deflection of both surfaces causing a significant drag increase and aircraft performance reduction. A large reduction	Significant drag increase and aircraft performance reduction	HAZ	Significant to excessive increase in pilot's workload	Increased fuel consumption and reduced controllability	Emergency landing	Not further investigated because fault tree shows very low probability

			in safety margins.						
Load control/ Load alleviation	Climb/Cruise and others	Undetected inaccurate deflection of the tab	Inaccurate deflection of the tab, efficiency degradation	Degraded A/C performance	MAJ	Limited increase in pilot's workload	Increased fuel consumption	Automatic recomputation of A/C block fuel	Investigate robustness of drag and loads reduction in order to obtain an estimate for precision tolerance

Table 13: Aircraft functions impacted by Morphing Winglet concept

The “Actuator runaway” refers to the case where the actuator results in free floating or excessive backlash. This event may occur when either the actuator is mechanically detached from the surface or it has lost its functionality or moves in an incorrect position.

Each row is a failure scenario, and the columns are dedicated to the morphing winglet device to identify the associated failure condition, severity, justification for classification, crew detection, recovery action and design parameters. In this way, it is possible to easily check the coherence of the safety classification and the completeness of the analysis.

The first row of the Table 13 deals with a failure scenario developed in terms of FHA and also verified in the integrated safety aeroelastic analysis (described in the following § 6.6). All other rows, instead, regard failure scenarios not related to the aeroelastic behavior; for this reason, they were only mentioned.

Basically, the morphing winglet can impact load control/load alleviation aircraft function. The failure scenario investigated is the uncontrolled dynamic motion of the left OR right morphing winglet.

For each side, the “main actors” of the latter event identified are:

1. Kinematic rupture of upper tabs;
2. Kinematic rupture of lower tabs.

Fig. 78 shows the fault tree developed only for the kinematic rupture of the upper tabs, identifying the lower tabs one as “undeveloped event” with the same failure rate. The further explosion of the gates involved occurs by OR logic, taking into account the potential loss of the actuator connection, the rupture of three hinges along the first hinge line and the rupture of three hinges/links of the morphing kinematics along the second hinge line.

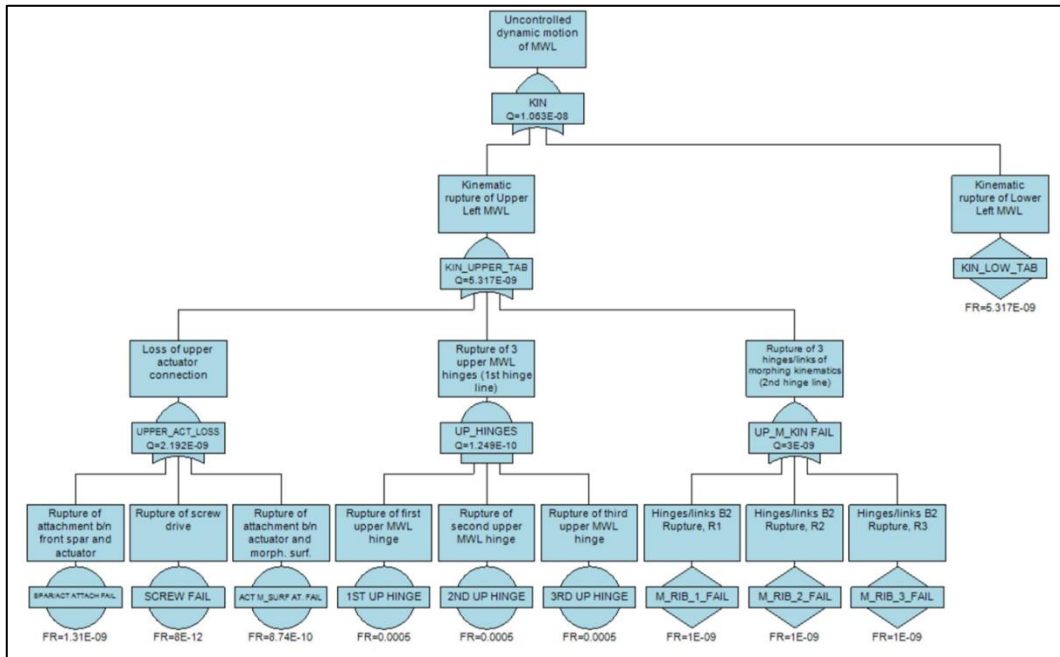


Fig. 78: Morphing winglet - Uncontrolled dynamic motion (left or right)
Fault Tree Analysis

Moreover, for the sake of completeness, the destruction of the wing was considered as top event of a new fault tree analysis (Fig. 79) aiming to verify its compliance with the catastrophic target (Failure probability 10^{-9}).

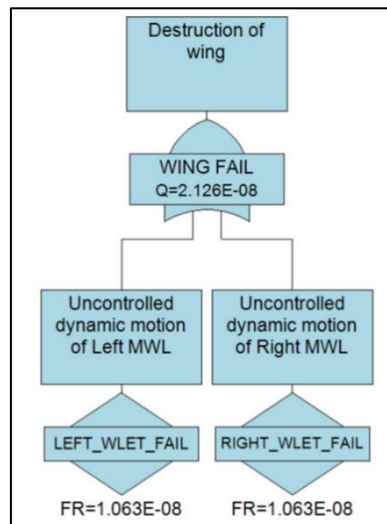


Fig. 79: Destruction of wing FTA

In Fig. 79, the same failure rate was assigned to both uncontrolled dynamic motion of right and left events, linked each other by an OR logic gate. The top event results with a failure rate of the order of 10^{-8} : this outcome reveals a light incompliance with respect to the CAT target (10^{-9}), to overcome which the use of proper damping devices on actuators or between consecutive tabs is highly suggested.

6.6 Integrated Safety Analyses

Referring to the winglet baseline configuration depicted in Fig. 80, identified as “Condition B” in section 5.3.2.5, several flutter cases were analyzed taking into account failure scenarios described in Table 14:

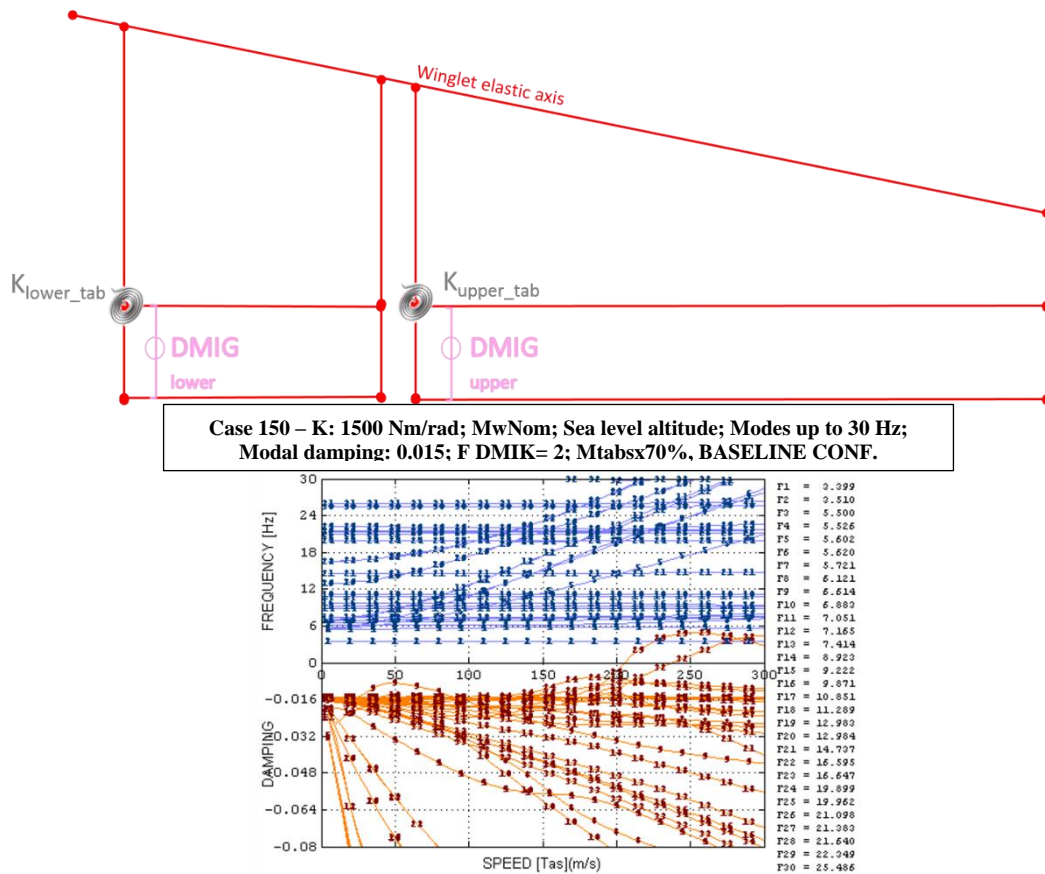


Fig. 80: LH winglet tabs actuators and gear ratio DMIG scheme, Baseline configuration

	K lower_tab	K upper_tab	Link lower_tab	Link upper_tab
1)	Nominal value, 1500 Nm/rad	Nominal value, 1500 Nm/rad	Operative	Failure
2)	Nominal value,	Nominal value,	Failure	Operative

	1500 Nm/rad	1500 Nm/rad		
3)	Nominal value, 1500 Nm/rad	Failure	Operative	Operative
4)	Failure	Nominal value, 1500 Nm/rad	Operative	Operative
5)	Nominal value, 1500 Nm/rad	Failure	Operative	Failure
6)	Failure	Nominal value, 1500 Nm/rad	Failure	Operative
7)	Nominal value, 1500 Nm/rad	Failure	Failure	Operative
8)	Failure	Nominal value, 1500 Nm/rad	Operative	Failure

Table 14: Failure scenarios investigated for morphing winglet

The behavior prediction in failure cases was performed in according to FHA (Fault and Hazard Analysis) specifications.

Following figures collect the trends of modes frequencies and damping versus speed, evaluated for the aforementioned eight cases of failure.

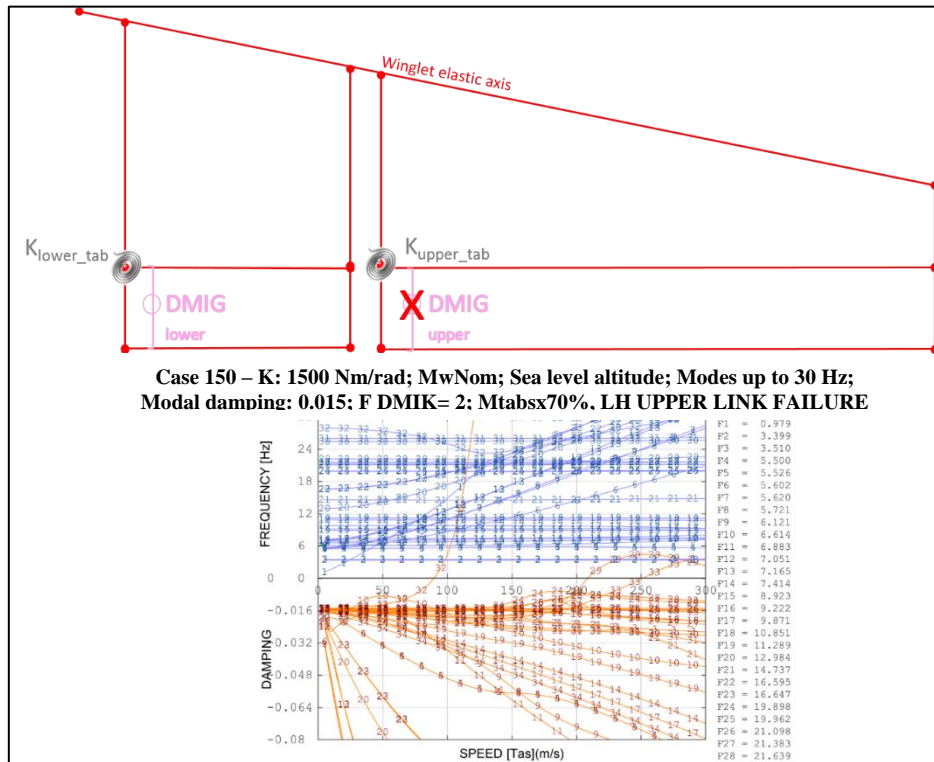


Fig. 81: CASE 1 – LH upper link isolated failure

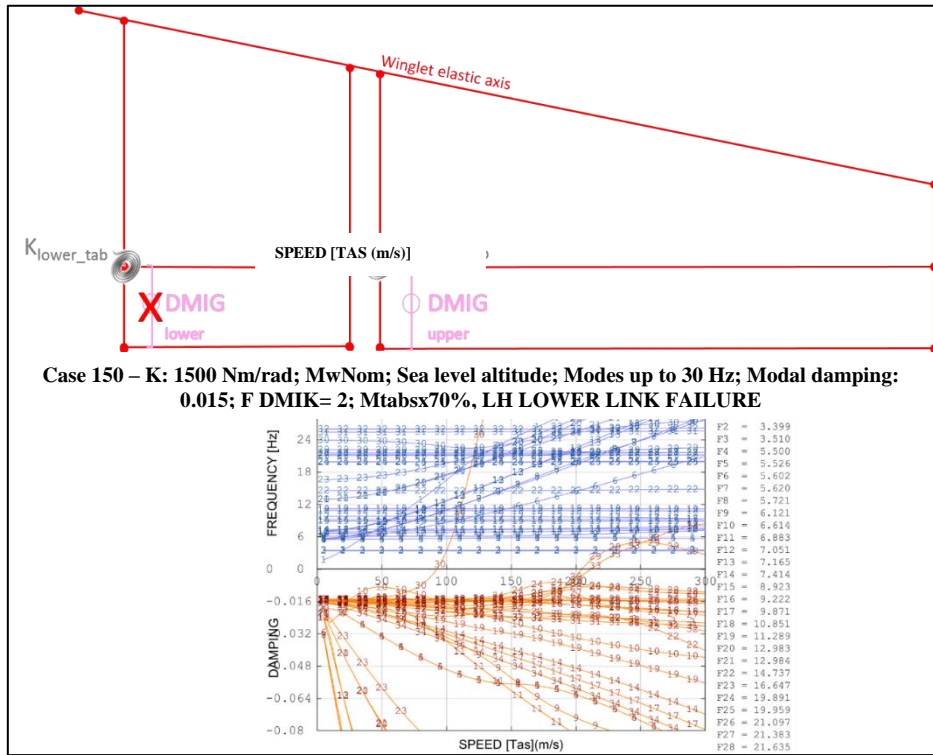


Fig. 82: CASE 2 – LH lower link isolated failure

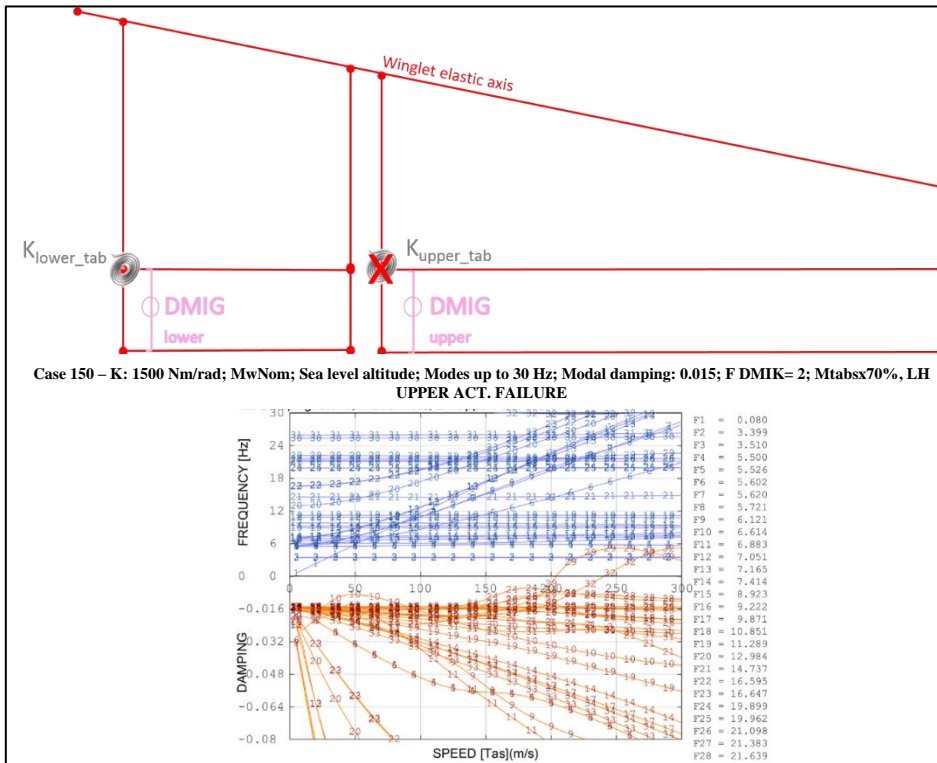


Fig. 83: CASE 3: LH upper tab actuator isolated failure

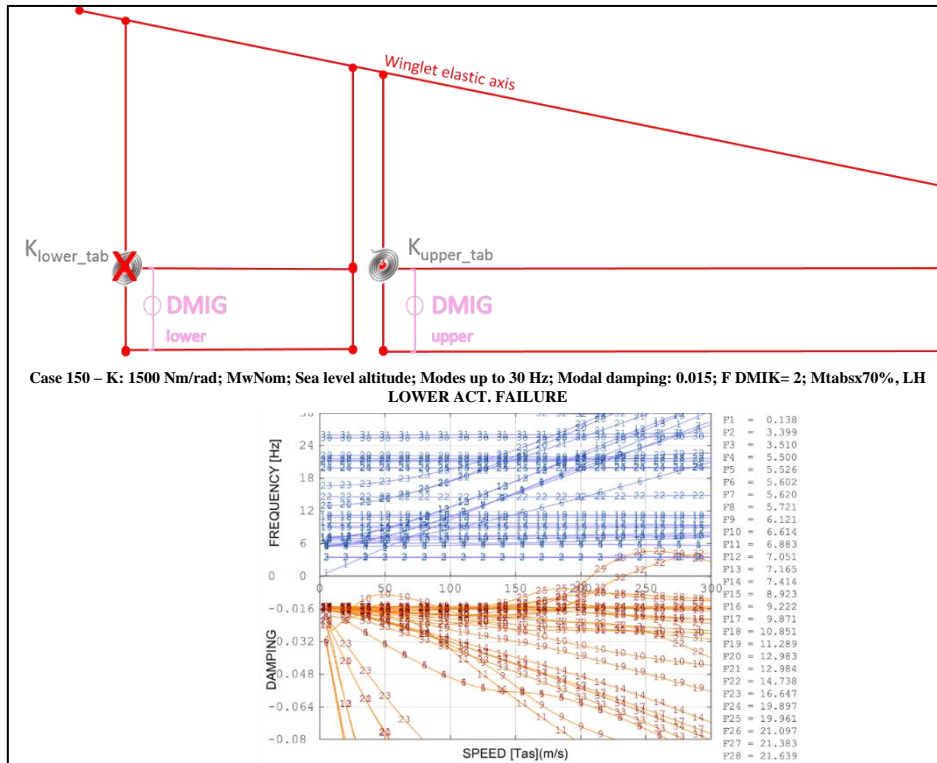


Fig. 84: CASE 4 - LH lower tab actuator isolated failure

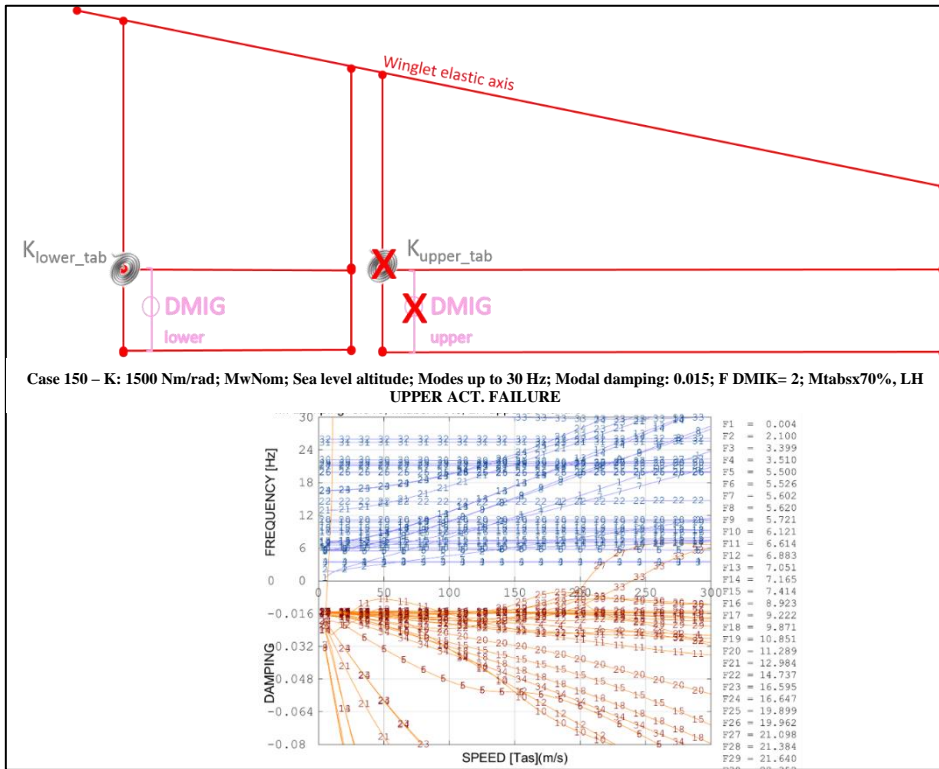


Fig. 85: CASE 5 – LH upper actuator and link combined failure

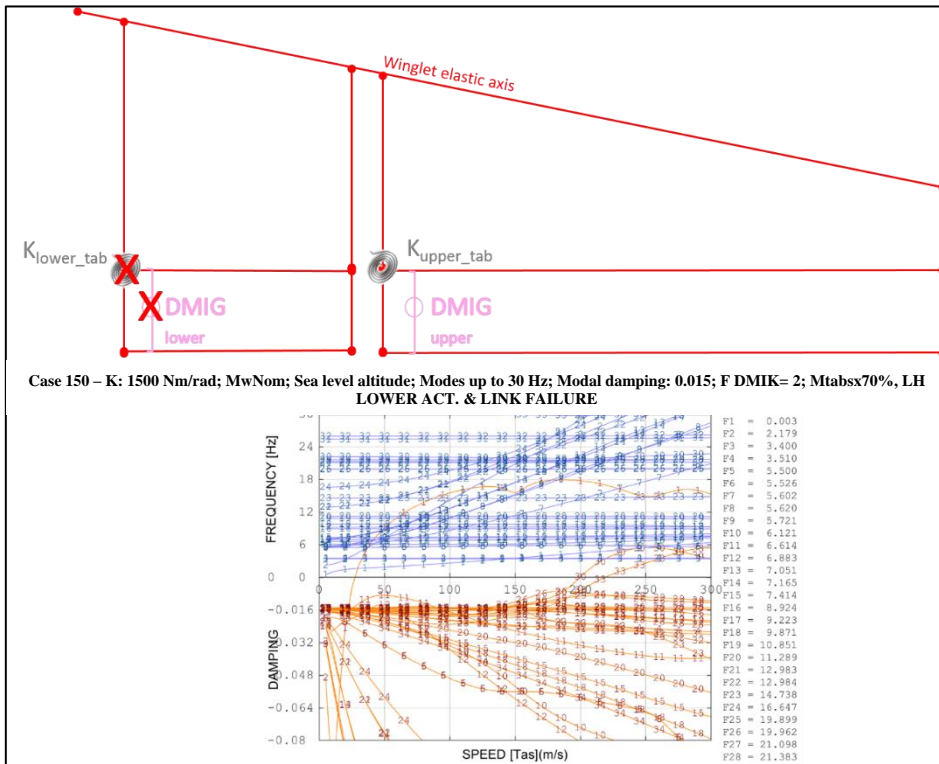


Fig. 86: CASE 6 – LH lower actuator and link combined failure

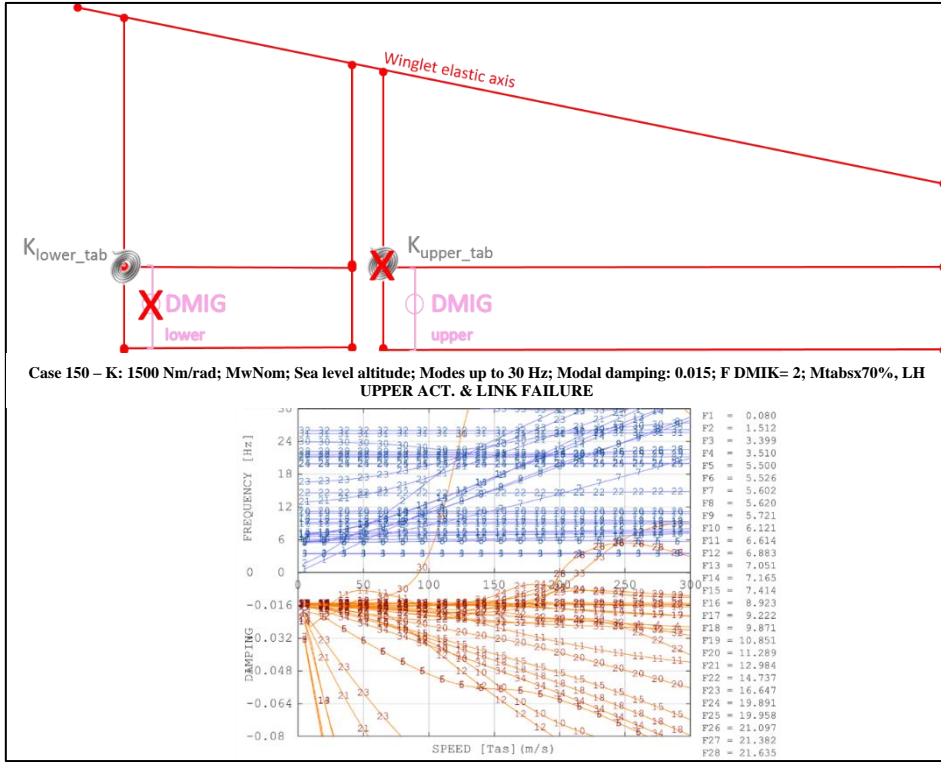


Fig. 87: CASE 7 – LH upper actuator and lower link combined failure

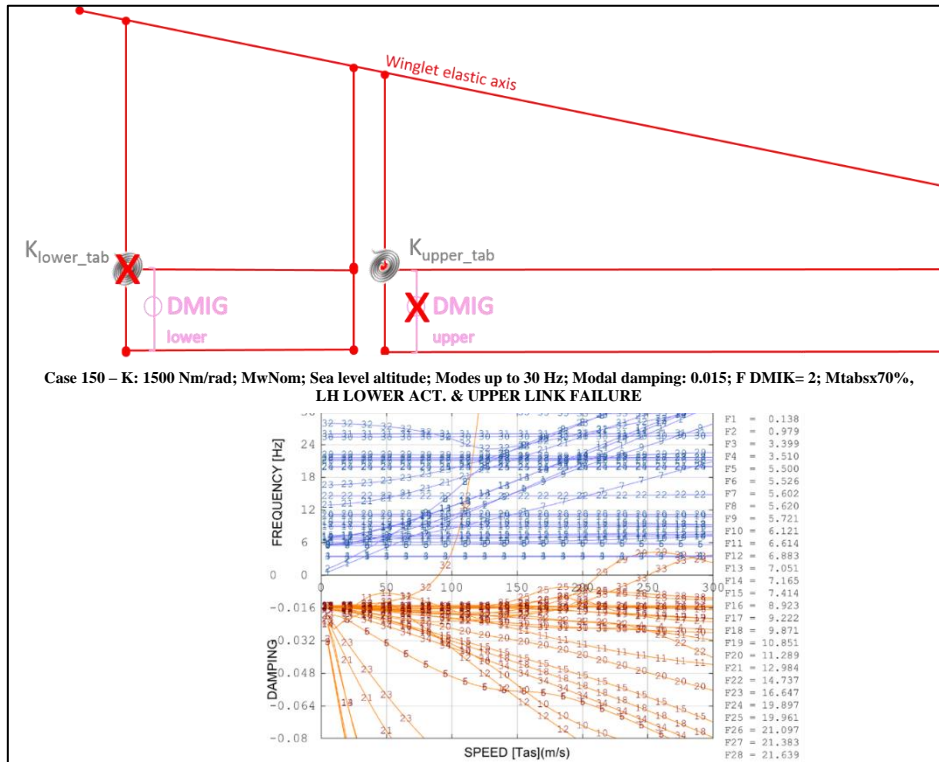


Fig. 88: CASE 8 – LH lower tab and upper link combined failure

All flutter analyses informations are summarized in Table 15.

CASE	K lower tab	K upper tab	Lower tab link	Upper tab link	v _{flutter} [m/s]	f _{flutter} [Hz]
1	Nominal	Nominal	Operative	Failure	89,842	25,717
2	Nominal	Nominal	Failure	Operative	92,517	22,922
3	Nominal	Failure	Operative	Operative	203,819	21,718
4	Failure	Nominal	Operative	Operative	208,03	21,831
5	Nominal	Failure	Operative	Failure	6,886	1,919
6	Failure	Nominal	Failure	Operative	27,541	1,587
7	Nominal	Failure	Failure	Operative	92,58	22,92
8	Failure	Nominal	Operative	Failure	89,944	25,711

Table 15: Flutter analyses results in failure scenarios investigated for morphing winglet

What emerges from these results are the following points:

- The isolated link rupture (cases 1 and 2) is more critical than the isolated actuator loss (cases 3 and 4);

- Upper link rupture (case 1) is more critical than the lower one (case 2);
- Actuator and link combined rupture, both belonging to upper tabs or lower tabs (cases 5 and 6), is the most critical event possible among the ones analyzed.
- Lower (upper) actuator loss, in combination with upper (lower) link rupture is a less critical event, if compared with the ones described in cases five and six.
- The only aeroelastically safe events are cases 3 and 4.

The use of damping on actuators or on tabs is highly recommended for a reassessment in compliance with the FHA severity.

7 Conclusions and Future Works

This thesis provides an extended aeroelastic assessment of two morphing wing devices, flap and winglet, both integrated into a 90-seat turboprop (TP90) regional transportation aircraft.

Experience teaches that due to the augmented Degree Of Freedoms (DOF), morphing wings are more prone to aeroelastic instabilities than more conventional architectures integrating passive counterparts. Non-classical effects may arise in terms of flutter-instabilities due to the unconventional systems arrangement and their mutual interaction, especially in malfunctioning or failure conditions.

This work followed an incremental criterion of problems to face; for this reason, it was divided into five stages:

1. In order to perform flutter analyses, the A/C aeroelastic model was properly generated. Rational approaches were adopted in terms of structural -stiffness and inertial- properties extraction by preliminary Finite Elements Models, referring to a stick-equivalent representation. Doublet Lattice Method (DLM) was used to develop the A/C aerodynamic grid by means of elementary units, called boxes. Superficial spline functions were then adopted to interpolate modal displacements at the center of each aerodynamic box.
2. A first campaign of trade-off analysis was performed on flap tabs, by considering the winglet at the *loop 0* of the preliminary design configuration. Combined variations were considered for flap tabs inertial and actuators stiffness parameters. Obtained results showed the presence of several flutter modes occurring at speeds lower than $1.25V_{\text{dive}}$ (200 m/s). The most critical flutter modes were analyzed in terms of modal shapes; tabs mass-balancing was identified as the best design solution to avoid the flutter.
3. A second campaign of trade-off analyses was carried out on winglet tabs, while flap tabs were maintained at locked commands and for them the inertial and stiffness configurations providing the lowest (and not critical) flutter speeds were considered. Also in this case, inertial and stiffness parameters of the actuators were both made to vary. Most critical flutter modes were identified and two design solutions were consequently suggested for ensuring flutter clearance:
 - Winglet tabs over-balancing;
 - 100% increase of the stiffness of the interface plug between wing/winglet

By comparing such solutions in terms of weight, the second one results the most convenient (less winglet mass) and, for this reason,

it was considered as the nominal configuration for the *loop 1* of the preliminary design.

4. Further flutter analyses were carried out by simulating winglet actuators free-play. For that purpose, harmonic balance method was adopted to model actuators equivalent stiffness from a bi-linear law. Flutter speed resulted out of the speed certification envelope in all the investigated cases.
5. Fault tree analyses were performed on morphing flap and winglet as isolated devices to quantify the probability of particular failure scenarios and to verify their eventual compliance with the airworthiness requirements. Such studies drove the combined aeroelastic assessments by considering several failure cases (isolated or combined link/actuator rupture). Gained results showed that actuator failure is more critical than link rupture, and the aeroelastic instability can be overcome by using proper damping devices.

This activity shows the importance of aeroelastic trade-off analyses since the early stages of the design process to properly size morphing systems, including kinematics, masses and distributed stiffness of the morphing surfaces.

In a multidisciplinary framework involving aerodynamics, structures, actuation architectures and control logics, aeroelastic instabilities analyses shall be integrated in the design loop to maximize the critical speeds of flutter, predict divergence, and control reversal of the morphing surfaces. The idea herein described leads the way to further researches aimed at enhancing the TRL of a morphing wing concept. In this regard, future steps may be:

- Aeroelastic refinements to guarantee flutter clearance using more advanced FE models;
- Aerodynamic model calibration by means of wind tunnel tests;
- Ground Vibration Test on morphing flap and adaptive winglet to obtain experimentally modal characteristics, proving the accuracy of the adopted schemes and the validity of aeroelastic instabilities;
- Mixed numerical-experimental flutter procedure to combine the most relevant experimental modes to the numerical inertial distribution of morphing flap and adaptive winglet.
- Combined fault tree analysis on morphing flaps and winglets by including aircraft failures such as asymmetric inoperative engine or strong lateral wind conditions;
- Assessment of the interaction among all smart tabs and aircraft primary control devices (ailerons, elevator, rudder).

APPENDIX A – General Description of the Sandy code

SANDY is a currently not-commercial code developed by M. Pecora [3] Within last twenty-five years, it was continuously optimized in order to meet industrial requirements for static and dynamic aeroelastic and aero-servo-elastic analyses of aircraft

A multidisciplinary environment - including rational approaches and validated numerical methods - achieves the following main tasks:

- A/C dynamic model (structural model and inertial model) generation;
- A/C aerodynamic model generation;
- Accurate transfer matrices interfacing between dynamic and aerodynamic models generation;
- A/C acceleration and loads response due to flight and ground maneuver and/or gust evaluation;
- A/C static and dynamic acceleration and loads response assessment to movable lifting surfaces deflections imposed by mechanical and/or electro-mechanical control circuits;
- Divergence, control reversal and flutter speeds evaluation.

The computational tool and numerical methods also gives the possibility to carry out fast analyses by investigating the A/C aeroelastic impact of combined design parameters. In this way, trade-off aeroelastic analyses can be achieved changing structural and dynamic properties relative to A/C components.

Sandy operates in Visual Fortran® / Matlab® environment, allowing highly efficient computational intercommunicating routines to evaluate:

- Static design loads for rigid and elastic aircraft;
- Turbulence-induced dynamic loads;
- Aeroelastic instabilities, also including command control laws by means of several methodologies.

Four macro-modules are present in its structure:

- Dynamic module;
- Aerodynamic module;

- Aeroelastic module.
- Plot visualization module.

Dynamic module generates A/C structural and inertial models and internally FE evaluates A/C modal parameters. For the sake of time optimization and model reliability, only two typologies of elements can be used:

- mono-dimensional elements (beam, rod, rigid-link, spring);
- DMIG (Direct Matrix Input at Grids) elements for a correct evaluation of stiffness and inertial properties of all those parts for which a mono-dimensional elements modelling leads to high approximations and/or is not applicable at all.

The dynamic module offers also the possibility to import DMIG elements and A/C modal parameters - modes shapes, frequencies, generalized masses, damping (also extractable by ground vibration tests) - by commercial FE software (e.g.: MSC-NASTRAN®).

The introduction of extra-modes representing movable surfaces deflection is allowed in dynamic module, in addition to the normal modes related to A/C structure.

The aerodynamic module generates the aerodynamic model and evaluates modal pressure distributions by means of Doublet Lattice Method.

In such a way, three-dimensional compressible aerodynamic models as well as the possibility of performing local corrections in pressure distributions can be accomplished in order to achieve a correct simulation of movable surfaces aerodynamics (as recommended by FAA AC 25.629-1A paragraph 6).

The aeroelastic module is finally constituted by all the routines devoted to:

- the interpolation of modal displacements on the aerodynamic lattice (matching routines implementing 3D spline methodologies);
- the evaluation of generalized aerodynamic pressures/forces and steady/unsteady aerodynamic influence coefficients;
- the solution of aeroelastic equations related to A/C aeroelastic response and aeroelastic instabilities identification.

Software overall accomplishments have been successfully proved, in terms of theoretical and experimental aeroelastic stability, during the certification processes of several commercial aircrafts.

APPENDIX B - CS 23.629 Flutter

For the sake of completeness, European airworthiness section regarding flutter analyses is reported.

(See AMC 23.629)

(a) It must be shown by the methods of (b) and either (c) or (d) , that the aeroplane is free from flutter, control reversal and divergence for any condition of operation within the limit V-n envelope and at all speeds up to the speed specified for the selected method. In addition –

(1) Adequate tolerances must be established for quantities which affect flutter; including speed, damping, mass balance and control system stiffness; and

(2) The natural frequencies of main structural components must be determined by vibration tests or other approved methods.

(b) Flight flutter tests must be made to show that the airplane is free from flutter, control reversal and divergence and to show by these tests that –

(1) Proper and adequate attempts to induce flutter have been made within the speed range up to V_D ;

(2) The vibratory response of the structure during the test indicates freedom from flutter;

(3) A proper margin of damping exists at V_D ; and

(4) There is no large and rapid reduction in damping as V_D is approached.

(c) Any rational analysis used to predict freedom from flutter, control reversal and divergence must cover all speeds up to $1.25 V_D$.

(d) Compliance with the rigidity and mass balance criteria (pages 4-12), in Airframe and Equipment Engineering Report No. 45 (as corrected) “Simplified Flutter Prevention Criteria” (published by the Federal Aviation Administration) may be accomplished to show that the aeroplane is free from flutter, control reversal, or divergence if –

(1) V_D/M_D for the aeroplane is less than 482 km/h (260 knots) (EAS) and less than Mach 0.5;

(2) The wing and aileron flutter prevention criteria, as represented by the wing torsional stiffness and aileron balance criteria, are limited to use to aeroplanes without large mass concentrations (such as engines, floats, or fuel tanks in outer wing panels) along the wing span; and

(3) The aeroplane –

(i) Does not have a T-tail or other unconventional tail configurations;

(ii) Does not have unusual mass distributions or other unconventional design features that affect the applicability of the criteria; and

(iii) Has fixed-fin and fixed-stabiliser surfaces.

(e) For turbo-propeller powered aeroplanes, the dynamic evaluation must include –

(1) Whirl mode degree of freedom which takes into account the stability of the plane of rotation of the propeller and significant elastic, inertial and aerodynamic forces; and

(2) Propeller, engine, engine mount and aeroplane structure stiffness and damping variations appropriate to the particular configuration.

(f) Freedom from flutter, control reversal and divergence up to V_D/M_D must be shown as follows:

(1) For aeroplanes that meet the criteria of sub-paragraphs (d) (1) to (d) (3), after the failure, malfunction, or disconnection of any single element in any tab control system.

(2) For aeroplanes other than those described in sub-paragraph (f) (1), after the failure, malfunction, or disconnection of any single element in the primary flight control system, any tab control system, or any flutter damper.

(g) For aeroplanes showing compliance with the fail-safe criteria of CS 23.571 and 23.572, the aeroplane must be shown by analysis to be free from flutter up to V_D/M_D after fatigue failure, or obvious partial failure of a principal structural element.

(h) For aeroplanes showing compliance with the damage-tolerance criteria of CS 23.573, the aeroplane must be shown by analysis to be free from flutter up to V_D/M_D with the extent of damage for which residual strength is demonstrated.

(i) For modifications to the type design which could affect the flutter characteristics compliance with sub-paragraph (a) must be shown, except that analysis alone, which is based on previously approved data, may be used to show freedom from flutter, control reversal and divergence for all speeds up to the speed specified for the selected method.

Advisory Circular AC No: 23.629-1A

Advisory Circular presents definitions and procedures to respond to 23.629 section:

2. SPECIAL DESIGN.

The special design category includes airplanes with certain design features that experience has shown warrant special consideration with regard to flutter. Flutter free operation for these special unconventional configurations may be shown by analyses which include an assessment of the effects of critical parameters. Flight

flutter tests to supplement those analyses are recommended. Some of these special unconventional configurations are:

a. Any aircraft with a design dive speed of 260 knots¹⁵ (EAS) or more at altitudes below 14,000 feet¹⁶ and Mach 0.6 or more at altitudes at and above 14,000 feet.

b. Any aircraft approved for flight in icing conditions. (The effect of ice accretions on unprotected surfaces, including those which might occur during system malfunctions, should be considered).

c. Pusher powerplants.

d. Canard geometry.

e. T, V, X, H, or any other unusual tail configuration.

f. Any external pods or stores mounted to wing or other major aerodynamic surface a

g. Fuel tanks outboard of 50% semispan.

h. Tabs which do not meet the irreversibility criteria of chapter 2, paragraph 3.d., and of reference 1, appendix 4.

i. Spring tabs.

j. All-movable tails, i.e., stabilators.

k. Slender boom or twin-boom fuselages.

l. Multiple-articulated control surfaces.

m. Wing spoilers.

n. Hydraulic control Systems with stability augmentation.

o. Full span flaps.

p. Leading edge devices (i.e., slots, etc.).

q. Geared tabs (servo or anti-servo, etc.).

4. Rational Analysis.

a. Review of Past Analysis. Review of previous flutter analyses conducted upon similar aircraft can provide the engineer with useful information regarding trends, critical modes, etc. Although in general such a review is not used as a substantiation basis for a new aircraft, it can provide a useful tool in evaluating the effect of modifications to existing certified aircraft.

b. Two-Dimensional Analysis. The flutter characteristics of straight wings (or tails) of large aspect ratio can be predicted reasonably well by considering a "representative section that has two or three degrees of freedom. Translation and pitch are always needed and) for control surfaces, the third freedom would be rotation about the hinge line.

c. Three-Dimensional Analysis. Current analysis is based upon consideration of total span, rather than representative section discussed in 4.b. above. The behavior is integrated over the whole structure being analyzed. Some idealization is always necessary; the most common being the division of the span into strips. Other types of modeling are also used. For Part 23 airplanes, quite often the wing and empennage analyses are conducted separately; however, this is not always adequate for unconventional configurations. Both the symmetric and antisymmetric motions require investigation. Calculated mass and stiffness distributions are generally used to calculate uncoupled modes and frequencies. These values are then used to conduct a coupled vibration analysis; the resulting coupled modes and frequencies are then usually compared with measured natural modes. The calculated stiffness-related inputs are generally adjusted until good agreement is obtained with the test data. Once satisfactory agreement is achieved, the coupled vibration analysis is normally used for the flutter calculations. It is suggested that one perform certain variations in the assumed input conditions to see which parameters are critical. Control surface balance conditions and system frequencies (especially tab frequencies) are often investigated parametrically. The effect of control system tension values at the low and high ends of the tolerance range should be assessed. It may be advantageous to arbitrarily vary certain main surface frequencies (stiffness), especially torsional frequencies and engine mode frequencies, while leaving other frequencies constant.

Sometimes it is desirable to evaluate the effect of a slight shift in spanwise node location for a very massive item where the node is located very close to or within the item. (Test data may not be sufficiently accurate for this assessment.)

It is normal practice to run a density-altitude check to include near sea-level, maximum and any other pertinent altitudes such as the knee of the airspeed-altitude envelope where the design dive speed becomes MACH limited. It is desirable to investigate combined wing-empennage modes for high performance (VD of 260 KEAS or above) airplanes, as well as for airplanes with unconventional configurations.

Flutter Analysis Evaluation: For a given set of input parameters, the resulting output generally consists of a number of theoretical damping values (g) with associated airspeeds and frequencies.

Various cross plots of these values among themselves and versus varied input parameters allow a study of trends.

Common plots are: damping vs. equivalent airspeed (g - V plots), control surface balance vs. flutter speed, uncoupled frequency vs. flutter speed, altitude vs. flutter speed, etc.

Normally only the critical items will be extensively compared.

Of particular importance is an evaluation in the neighborhood of the crossing of a damping velocity ($g=0$ -V) curve toward the unstable damping region, through zero.

The typical critical g -V curve will first become increasingly stable and with increasing speed will turn and rise toward or pass through $g=0$, then at some higher speed may again turn toward the stable region. Typical characteristics are discussed in the following examples:

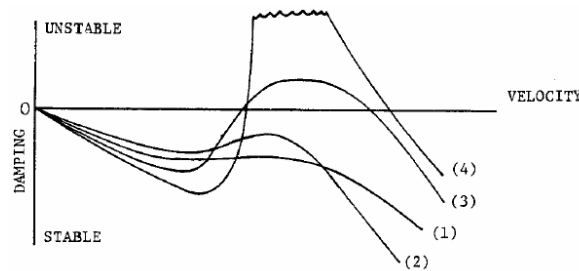


Fig. 89: Example of V-g plot

Curves 1 and 2 show slight trends toward instability, but do not approach actual instability.

Curve 3 crosses the stability axis but, depending on the inherent structural damping, may or may not actually become unstable.

Curve 4 is obviously unstable and probably violent, since its slope is steep as it passes through zero. In actual flight it may only be a mile an hour or so between completely stable and extremely unstable explosive flutter. Flight tests are not advisable when this type plot is observed inside or near the flight envelope.

Much can be learned from g -V curves. (Absolute values should be viewed with some reserve as there is no perfect one-to-one correspondence of the analytical parameters and flight parameters.) where the critical curve crosses the axis (with respect to $V_{g=0}$ for the airplane) is important. Equally important is the rate of approach to instability (slope of curve).

The general practice is to use a damping value of $g=0.03$ at $1.2 V_D$ as the flutter limit of the g -V plots. However, this value should be used with caution if the slope of the curve is large (damping decreases very rapidly with an increase in airspeed) between $g=0$ and 0.03 . In cases where the slope is steep, it is suggested that the $g=0$ airspeed be at least $1.2 V_D$.

If flight flutter testing is conducted to verify damping under the above circumstances, extreme caution should be exercised.

For damping curves such as (3), which peak out below 1.2 VD, the predicted damping should be no more unstable than $g=0.02$ unless justification is provided by other acceptable means.

References

- [1] Pecora, R., “Multi-modal morphing wing flaps for next generation green regional aircraft: the Cleansky challenge”, Proceedings of the ASME 2018 Conference on Smart Materials, Adaptive Structures and Intelligent Systems SMASIS2018 September 10-12, 2018, San Antonio, TX, USA.
- [2] European Aviation Safety Agency, Certification Specifications and Acceptable Means of Compliance for Large Aeroplanes – CS-25, Amendment 11, July 2011.
- [3] Pecora, R., Amoroso, F., Noviello, M. C., Concilio, A., Dimino, I., “Aeroelastic stability analysis of a large civil aircraft equipped with morphing winglets and adaptive flap tabs”, Proceedings of SPIE. 10595, Active and Passive Smart Structures and Integrated Systems XII, March 2018.
- [4] Bisplinghoff, R. L., Ashley, H., Halfman, R. L., “Aeroelasticity”, Dover Publications, Inc., 1955.
- [5] Roger, K. L., “Airplane Math Modeling and Active Aeroelastic Control Design,” Proceedings of AGARD CP-228, pp. 1–11, 1977.
- [6] Browman, J., Sanders, B., and Weisshaar, T., “Evaluating the Impact of Morphing Technologies on Aircraft Performance”, Proceedings of the Forty-Third AIAA Conference on Structures, Structural Dynamics and Materials, AIAA Paper 2002-1631, April 2002.
- [7] Raymer, D. “Aircraft Design: A Conceptual Approach”, AIAA Education Series, Fourth edition, 2006.
- [8] Yang R. J. and Chahande A. I., “Automotive applications of topology optimization”. Journal of Structural and Multidisciplinary Optimization, 9:245–249, 1995.
- [9] Bendsoe, M. P., “Optimal shape design as a material distribution problem”, Journal of Structural Optimization, 1:193–202, 1989.
- [10] Lu K. and Kota S., “Parameterization strategy for optimization of shape morphing compliant mechanisms using load path representation”. Proceedings of ASME Design Engineering Technical Conference, DETC2003/DAC-48775, 2003.
- [11] Bendsoe, M. and Sigmund, O., “Topology Optimization: Theory, Methods and Applications”. Springer-Verlag Berlin, 2004.
- [12] Sigmund, O., “Morphology-based black and white filters for topology optimization”. Journal of Structural and Multidisciplinary Optimization, 33:401–424, 2006.
- [13] Kharal, A. and Saleem, A., “Neural networks based airfoil generation for a given CP using Bezier-PARSEC parameterization”, Journal of Aerospace Science and Technology, 2011.
- [14] Huyse, L. and Lewis, R. “Aerodynamic Shape Optimization of Two-dimensional Airfoils Under Uncertain Conditions”, NASA ICASE Report No. 2001-1, pages 1–8, 2001.
- [15] Zingg, D. W. and Elias, S., “Aerodynamic Optimization Under a Range of Operating Conditions”, AIAA Journal, 44:2787–2792, 2006.
- [16] Trenker, M. “Design Concepts for Adaptive Airfoils with Dynamic Transonic Flow Control”, Journal of Aircraft, 40:734–740, 2003.
- [17] Wadehn, W., Sommerer, A., Lutz, T., Fokin, G., Pritschow, S. and Wagner, S. “Structural concepts and aerodynamic design of shock control bumps”, Proceedings of ICAS Congress, 2002.

- [18]Hodges, D. H. and Pierce, G. A., “Introduction to Structural Dynamics and Aeroelasticity”, Cambridge University Press (Aerospace Series), 2002.
- [19]Pederson, C. B. W., Buhl, T. and Sigmund, O., “Topology synthesis of large-displacement compliant mechanisms”, *Journal of Numerical Methods in Engineering*, 50:2683–2705, 2001.
- [20]Della Vecchia, P., Corcione, S., Pecora, R., Nicolosi, F., Dimino, I., Concilio, A., “Design and integration sensitivity of a morphing trailing edge on a reference airfoil: The effect on high-altitude long-endurance aircraft performance”, *Journal of Intelligent Material Systems and Structures*, Vol. 28, Issue 20, 2017.
- [21]Sofla, A., Meguid, S., Tan, K., and Yeo, W., “Shape morphing of aircraft wing: Status and challenges. *Journal of Materials and Design*”, 31:1284–1292, 2010.
- [22]Bye, D. R. and McClure, P. D., “Design of a Morphing Vehicle”, *Proceedings of 48th AIAA Structures, Structural Dynamics, and Materials Conference*, AIAA 2007-1728, 2007.
- [23]Prock, T., Weisshaar, A. and Crossley, W. A., “Morphing airfoil shape change optimization with minimum actuator energy as an objective”, *Proceedings of 9th AIAA Symposium on Multidisciplinary Analysis and Optimization*, AIAA 2002-5401, 2002.
- [24]Jacob, J., Simpson, A. and Smith, S. “Design and Flight Testing of Inflatable Wings with Wing Warping”, *Society of Automotive Engineers*, 05WAC-61, 2005.
- [25]Blondeau, J., Richeson, J. and Pines, D. “Design, development and testing of a morphing aspect ratio wing using an inflatable telescopic spar”, *Proceedings of 44th AIAA Structures, Structural Dynamics, and Materials Conference*, AIAA 2003-1718, 2003.
- [26]Bye, D. R. and McClure, P. D., “Design of a Morphing Vehicle”, *Proceedings of 48th AIAA Structures, Structural Dynamics, and Materials Conference*, AIAA 2007-1728, 2007.
- [27]Skillen, M. D. and Crossley, W. A., “Modelling and Optimization for Morphing Wing Concept Generation”, *The Langley Research Centre NASA*, NASA/CR-2007-214860, 2007.
- [28]Garcia, H., Abdulrahim, M. and Lind, R., “Roll control for a micro air vehicle using active wing morphing”, *Proceedings of AIAA Guidance, Navigation, and Control Conference Exhibit*, AIAA- 2003-5347, 2003.
- [29]Clean Sky2 program official website: www.cleansky.eu
- [30]De Gaspari, A., Gilardelli, A., Ricci, S., Airoidi, A., “Design of a leading edge morphing based on compliant structures in the framework of the CS2-AIRGREEN2 project”, *Proceedings of the ASME 2018 Conference on Smart Materials, Adaptive Structures and Intelligent Systems SMASIS2018 September 10-12, 2018, San Antonio, TX, USA*.
- [31]Noviello, M. C., Dimino, I., Amoroso, F., Concilio, A., Pecora, R., “Preliminary assessment of morphing winglet and flap tabs influence on the aeroelastic stability of next generation regional aircraft”, *Proceedings of the ASME 2018 Conference on Smart Materials, Adaptive Structures and Intelligent Systems SMASIS2018 September 10-12, 2018, San Antonio, TX, USA*.
- [32]Rea, F., Amoroso, F., Pecora, R., Noviello, M. C., Arena, M., “Structural design of a multifunctional morphing fowler flap for a twin-prop regional aircraft”, *Proceedings of the ASME 2018 Conference on Smart Materials, Adaptive Structures and Intelligent Systems SMASIS2018 September 10-12, 2018, San Antonio, TX, USA*.

- [33] Pecora, R., Amoroso, F., Amendola, F. and Concilio, A., “Validation of a smart structural concept for wing-flap camber morphing,” *Smart Structures and Systems*, vol. 14, no. 4, pp. 659–678, 2014.
- [34] Rea, F., Amoroso, F., Pecora, R., Kintscher, M., “Design of an adaptive twist trailing edge for large commercial aircraft applications”, *Proceedings of the ASME 2018 Conference on Smart Materials, Adaptive Structures and Intelligent Systems SMASIS2018* September 10-12, 2018, San Antonio, TX, USA.
- [35] Rudolph, P.K.C., “High-lift systems on commercial subsonic airliners”, *Technical Report*, NASA-CR-4746, 1996.
- [36] Amendola, G., Dimino, I., Concilio, A., Pecora, R., Cascio, M.L., “Preliminary design process for an adaptive winglet”, *International Journal of Mechanical Engineering and Robotics Research*, 2018.
- [37] Dimino, I., Amendola, G., Di Giampaolo, B., Iannaccone, G., Lerro, A., “Preliminary design of an actuation system for a morphing winglet”, *Proceedings of 8th International Conference on Mechanical and Aerospace Engineering (ICMAE)*, pp. 416-422, 2017.
- [38] Dimino, I., Ameduri, S., Concilio, A., “Preliminary failure analysis and structural design of a morphing winglet for green regional aircraft”, *Proceedings of the ASME 2018 Conference on Smart Materials, Adaptive Structures and Intelligent Systems SMASIS2018* September 10-12, 2018, San Antonio, TX, USA.
- [39] Amendola, G; Dimino, Ignazio, Concilio, Antonio, Andreutti, G, Pecora, Rosario, Lo Cascio, M., “Preliminary design process for an adaptive winglet”, *International Journal of Mechanical Engineering and Robotics Research*, 7. 83-92. 10.18178/ijmerr.7.1.83-92, 2018.
- [40] Lo Cascio, M., MSc Thesis, “Ottimizzazione Topologica del Trailing Edge Adattivo di una Winglet Morphing”, University of Palermo, 2017.
- [41] Pecora, M., “Modellistica aeroelastica per analisi di flutter”, *Documento Tecnico Interno CIRA*, CIRA-TR-05-0101, 2005.
- [42] Roger, K., “Airplane Math Modelling Methods for Active Control Design,” *Structural Aspects of Control*, AGARD Conference Proceeding, Vol. 9, pp. 4.1, 1977.
- [43] Pecora, M., “Dispense del corso di Aeroelasticità applicata tenuto presso la Seconda Università degli Studi di Napoli a.a. 2000/2001”, 2001.
- [44] MSC/MD NASTRAN®, *Software Package*, Ver. R3-2006, “Reference Manual”.
- [45] SAE ARP 4754a (2010) US SAE international, *guidelines for development of civil aircraft and systems*, Revised Dec 2010.
- [46] SAE ARP 4761 (1996) US SAE international, *guidelines and methods for conducting the safety assessment process on civil airborne systems and equipment*, Dec 1996.
- [47] Verrastro, M., Metge, S., “Morphing Wing Integrated Safety Approach and Results”, *Smart Intelligent Aircraft Structures (SARISTU)*, pp. 43-69, 2015.
- [48] *Reliability Workbench Reference Manual*.
- [49] Palmieri M., Pispola, G., Dimino, I., “Contribution to final specifications of the morphing winglet actuation system”, *Airgreen 2 Project Deliverable O 2.1.2-18*, 2018.